Modellering van transitie door zogimpact
met dynamische beschrijving van intermittentie

Modelling of Wake-Induced Transition
with Dynamic Description of Intermittency

Koen Lodefier

Promotor: prof. E. Dick
Proefschrift ingediend tot het behalen van de graad van
Doctor in de Ingenieurswetenschappen: Werktuigkunde-Elektrotechniek

Vakgroep Mechanica van Stroming, Warmte en Verbranding
Voorzitter: prof. E. Dick
Faculteit Ingenieurswetenschappen
Academiejaar 2005 - 2006

UNIVERSITEIT
GENT

ISBN 90-8578-042-X
NUR 978
Wettelijk depot: D/2005/10.500/42

Dankwoord

Ik wens mijn dank uit te drukken aan mijn begeleider Prof. Erik Dick voor de continue hulp gedurende mijn doctoraat, en tevens voor de geboden kansen om mijn werk te gaan toetsen aan de intenationale turbomachine wereld. Ik had het geluk te kunnen vertrekken van een jarenlange expertise op het gebied van transitie modelering, reeds aanwezig in de vakgroep.

Ik richt ook mijn dank naar de collega's van de vakgroep die steeds bereid waren tot een technische discussie of een informele babbel.

Word of thanks

I would like to express all my gratitude to my supervisor Prof. Erik Dick for the continuous support during the research phase of my Ph.D. I also acknowledge the given opportunities to compare my work with the international status. I was lucky to be able to rely on years of experience already achieved in the field of transition modeling, at the department.

I also want to mention the support from all partners of the UTAT project.

English Summary

The research presented in this Ph.D. thesis aims at the numerical calculation of reference test cases for wake-induced transition. By extension, the method can be applied to calculate flow in the low pressure part of a gasturbine engine.

Gasturbine engines are mainly used for propulsion of airplanes, and for generation of electricity. They consist of three major parts. The flow enters the gasturbine through the compressor. Compressed air is heated and converted into combustion gas in the combustion chambers. In the final part, combustion gas at high temperature is expanded in the turbine. The turbine consists of several parts. The high pressure turbine has small dimensions, but the velocities are high, and so is the Reynolds number. The combustion gas is further expanded in the low pressure turbine. Because of the low rotational speed, the dimensions of this turbine are rather big. The rotational speed is low because the low pressure turbine drives the fan. An example of a gasturbine for aviation purposes is shown in Figure 1.

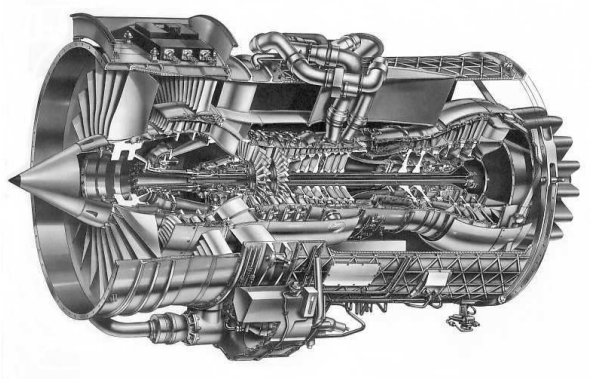

Figure 1: Gasturbine for aviation purposes.

For aero applications working at high altitude, the air density is low. So in the low pressure turbine the Reynolds number is low. This means that, although the free-stream flow is turbulent, the boundary layer remains laminar over a substantial part of the profile. Due to weight considerations, the number of blades is limited, with a high loading on each blade. In steady flow, the laminar boundary layer would separate in the decelerating part on the suction side. This would lead to very high losses. In real engine conditions, the wakes from upstream blade rows enter the blade passage, and periodically suppress the separation. This makes the time averaged losses decrease.

For applications on ground level, the air density is higher, and reduction of the turbine weight is not essential. This means that the Reynolds number is higher and the loading is lower. So the flow has considerably less tendency to separate.

Computational fluid dynamics that are industrially applicable average out all turbulent fluctuations (RANS), and model their influence on the flow in a turbulent viscosity assumption. RANS simulations provide accurate laminar flow solutions. Further, large amount effort has been put into the accurate description of turbulent flow, for a broad range of flow configurations. Generally, the accuracy of turbulent simulations increases with Reynolds number. In the open literature, few models can be found that are able to describe transition from a laminar to a turbulent flow. An overview is given in Chapter 2.

To design a new turbine, computational simulation is a rapid and cheap tool. The other option is to perform experimental measurements. But due to the complex geometry of a gasturbine, these measurements are expensive, not extensive or simply impossible. Most measurements are performed on reference configurations in a laboratory setup. These measurements neglect three dimensional effects (often important in LP turbines) and influence of rotation. Nevertheless, these measurements are very interesting, and are used here for validation of the model, in Chapter 6. Up to now, the only method to actually 'know' what is going on in the engine is via numerical simulation.

The development of the model is a continuation of the work from Steelant and Dick [76] performed at the department of the author. They developed a steady transition model using conditional averaging of the flow. This technique takes into account the interactions between the laminar and the turbulent flow parts. This was considered too expensive for industrial applications, and is therefore not used in the present model. The model, used in RANS context, is extended to unsteady flow in Chapter 3. The intermittency is divided into two

components, a near-wall intermittency factor, and a free-stream factor. This was necessary because their time scales are much different. The velocity scale in the equation for near-wall intermittency is altered for the case of kinematic wake impact on a separation bubble.

The model is based on steady criteria which often rely on the leading edge turbulence intensity. These steady criteria were derived from experiments on flat plates. Flat plate test cases have also been used during development of the present model. The results are discussed in Chapter 4. Afterward, the model has been applied to steady cascade test cases in Chapter 5. Their geometry is much more complex. Due to the strong acceleration on the leading edge, the oncoming turbulence level is no longer characteristic for the turbulence intensity level at transition. So the local value is used. Finally, these criteria, made dependent on the local turbulence intensity, are used in unsteady cascade test cases. This is proved to be successful.

In the unsteady cases, periodic wake passage is a trigger to transition. The wake passage has two components, a kinematic impact followed by an increased level of free-stream turbulence intensity. In between the wakes a background turbulence intensity is seen. Three different types of unsteady behaviour are seen. A first type is that the flow is attached, and transition moves forward under the increased free-stream turbulence of the wake. A second type is that the flow is separated in between the wakes, but reattaches under wake passage. The kinematic wake impact on the separation bubble induces a large scale roll-up of the separation bubble. The roll-up is followed by wake turbulence induced transition. A third type is that the flow is always separated on the suction side, but that the size of the separation bubble reduces under the wake passage.

Some shortcomings are revealed. The calculations are two-dimensional, and consequentely, the break-up of roll-up vortices is not well captured. The turbulence model is seen to overpredict turbulence production in the complex geometry between the blades. Therefore, we conclude that further improvement of the simulation result can be obtained by improving the *turbulence* model. It seems very appealing to use the model in a hybrid RANS/LES context. This would require some adaptation of the model.

Nederlandse samenvatting

In dit werk wordt een numerieke berekening van zog-geïnduceerde transitie beoogd. Bij uitbreiding kan de methode gebruikt worden om de stroming te simuleren in het lage-druk-gedeelte van een gasturbine-motor.

Gasturbine-motoren worden hoofdzakelijk gebruikt voor de voortstuwing van vliegtuigen, of voor het opwekken van elektriciteit. Ze bestaan hoofdzakelijk uit drie onderdelen. De stroming komt de gasturbine binnen langs de compressor. Gecomprimeerde lucht wordt verwarmd en omgezet tot verbrandingsgas in de verbrandingskamers. In het laatste gedeelte wordt het verbrandingsgas geëxpandeerd in de turbine. De turbine bestaat uit verscheidene onderdelen. De hoge-druk-turbine heeft kleine afmetingen, maar de snelheden zijn groot alsook het Reynolds getal. Het verbrandingsgas wordt verder geëpandeerd in de lage-druk-turbine. De afmetingen van deze turbine zijn eerder groot tengevolge van de lage rotatiesnelheid van deze turbine. De turbine dient immers voor aandrijving van de fan. Een voorbeeld van een gasturbine voor luchtvaart doeleinden is gegeven in Figuur 2.

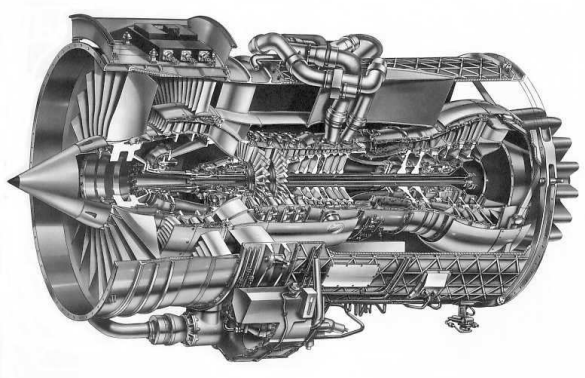

Figuur 2: Gasturbine voor luchtvaart doeleinden.

Voor luchtvaarttoepassingen werkend op grote hoogte is de densiteit van de lucht klein. Dientengevolge is het getal van Reynolds laag. Dit betekent dat, alhoewel de vrije stroming turbulent is, de grenslaag laminair blijft over een groot deel van het profiel. Tengevolge van gewicht overwegingen is het aantal schoepen beperkt, dus de belasting per blad is hoog. In stationaire stroming zou de laminaire grenslaag afscheiden in het vertragende gedeelte van de zuigzijde. Dit zou leiden tot zeer hoge verliezen. In realistische motorcondities komen de zogzones van stroomopwaartse schoepen de schoepenrij binnen, en onderdrukken periodiek de afscheiding. Hierdoor gaan de tijdsgemiddelde verliezen dalen.

Bij toepassingen op grondniveau is de densiteit van de lucht groter, en is een reductie van het turbinegewicht niet noodzakelijk. Dit betekent dat het Reynolds getal groter is, en de schoepbelasting lager. Bijgevolg is de neiging tot afscheiding veel geringer.

Industrieel relevante numerieke stromingsberekeningen middelen alle turbulente fluctuaties uit (RANS). Hun invloed op de stroming is gemodelleerd via een turbulente viscositeit. RANS-simulaties leveren nauwkeurige oplossingen van laminaire stroming. Daarenboven is een grote hoeveelheid arbeid gestopt in het accuraat beschrijven van turbulent stromingen is een groot aantal stromingsconfiguraties. Globaal gezien neemt de nauwkeurigheid toe met toenemend Reynolds getal. In de open literatuur bestaan echter weinig modellen die in staat zijn om de transitie van een laminaire naar een turbulente stroming te beschrijven. Een overzicht is gegeven in hoofdstuk 2.

Numerieke simulaties zijn een goedkoop en snel hulpmiddel bij het ontwikkelen van een nieuwe turbine. De andere optie bestaat erin de stroming experimenteel te gaan bemeten. Echter, wegens de complexe geometrie van een gasturbine zijn deze metingen duur, veelal niet volledig of soms zelfs onmogelijk. Het merendeel van de metingen worden uitgevoerd op referentieopstellingen in een laboratorium. Deze metingen houden geen rekening met driedimensionele effecten (vaak belangrijk in lage-druk-turbines) en de invloed van de rotatie. Toch zijn deze metingen zeer interessant, en ze worden hier gebruikt ter validatie van het model in hoofdstuk 6. Tot op heden is de enige manier om echt 'te weten' te komen wat er gebeurt in een gasturbine de berekening via een numerieke methode.

De ontwikkeling van het model is een voortzetting van het werk van Steelant en Dick [76], uitgevoerd aan deze vakgroep. Zij ontwikkelden een stationair transitiemodel op basis van conditioneel gemiddelde snelheidsprofielen.

Deze techniek beschrijft de interactie tussen laminaire en turbulente stomingsgedeeltes. In een industriële context wordt dit gezien als te duur, en conditionering wordt dan ook niet langer gebruikt in het huidige model. Het model in een RANS context werd uitgebreid naar instationaire stroming in hoofdstuk 3. De intermittentieparameter is opgedeeld in twee parameters, een parameter voor vrije-stroming-intermittentie, en een parameter voor de intermittentie in de grenslaag. Deze opdeling is nodig omdat de tijdsschaal van beide fenomenen sterk verschillend is. De snelheidsschaal in de vergelijking voor grenslaagintermittentie werd aangepast in het geval van kinematisch impact van een zog op de grenslaag.

Het model is gebaseerd op de stationaire criteria die vaak gebruik maken van de turbulentie-intensiteit op de aanvalsboord. Deze criteria werden bepaald op basis van vlakke plaat experimenten. Vlakke plaat experimenten zijn hier ook gebruikt bij de ontwikkeling van het hiudige model. De resultaten worden besproken in hoofdstuk 4. Daarna werd het model toegepast op stationaire cascade testgevallen in hoofdstuk 5. Hun geometrie is complexer. Ten gevolge van de sterke acceleratie bij de aanvalsboord is de aankomende turbulentieniveau niet langer kenmerkend voor de turbulentie-intensiteit nabij transitie. Daarom is de locale waarde gebruikt. Uiteindelijk werden deze criteria toegepast gebruikmakende van de locale turbulentie-intensiteit op instationaire cascade testgevallen. Deze methode is succesvol gebleken.

De periodisch inkomende zogzones in de instationaire testgevallen vormen een aanzet tot transitie. Het zog heeft twee componenten, een kinematisch impact gevolg door een hoge waarden van turbulentie-intensiteit in de vrije stroming. Tussen de zogzones wordt de achtergrond turbulentie-intensiteit waargenomen. Drie verschillende vormen van instationair gedrag komen voor. In een eerste type is de stroming steeds aangehecht, en schuift de transitie stroomopwaarts onder de hoge waarden van turbulentie-intensiteit afkomstig van het zog. Een tweede type is dat de stoming loslaat tussen de zogimpacten, maar terug aanhecht onder zogimpact. Een derde type is dat de stroming afgescheiden is, maar met een reductie van de afscheidingszone onder zogimpact.

Enkele tekortkomingen kwamen aan het licht. De berekeningen zijn tweedimensionaal, en bijgevolg is de afbraak van de oprolwervels niet gezien in de simulatie. We bemerken dat het turbulentiemodel de productie van turbulente kinetische energie in complexe geometieën overschat. Daarom komen we tot de conclusie dat een betere overeenkomst kan bereikt worden door aanpassing van het *turbulentie*model. Het lijkt zeer aantrekkelijk om het transitiemodel

toe te passen in combinatie met een hybride RANS/LES turbulentiemodel. Dit zou enige aanpassingen aan het transitiemodel vergen.

Contents

1 General introduction **1**

2 Literature review **7**

2.1 Transition 7

2.1.1 Natural transition 7

2.1.2 Bypass transition 8

2.1.3 Separated flow transition 19

2.1.4 Relaminarisation 19

2.1.5 Turbulent spot and the Emmons theory 20

2.2 Modelling transition 24

2.2.1 (Nonlinear) eddy-viscosity models 28

2.2.2 Menter's approach 30

2.2.3 Walters - Leylek model 34

2.2.4 PUIM 36

2.2.5 Dynamic Intermittency 40

3 The model **43**

3.1 Choice between a $k-\varepsilon$ and a $k-\omega$ turbulence model 43

3.2 The unsteady transition model 46

3.2.1 Modifications of the turbulence model 46

3.2.2 The turbulence weighting factor τ 49

3.2.3 Equation for free-stream factor ζ 50

3.2.4 Equation for near-wall intermittency factor γ 51

3.2.5 Starting and stopping of transition 57

4 Flat plate test cases **59**

4.1 Introduction 59

4.2 Test-cases 59

4.3 Numerical results on KW and T3 test cases. 61

4.4 Conclusion 65

5 Steady cascade **67**

5.1 Introduction 67

5.2 VKI Cascade Test case 67

5.2.1 Geometry 67

5.2.2 Numerical results 69

5.3 MUR cascade test case 72

5.3.1 Geometry 72

5.3.2 Heat transfer: modelling assumptions 72

5.3.3 Numerical results 74

5.4 Conclusion 77

6 Unsteady cascade test cases **79**

6.1 Introduction 79

6.2 T106A 80

6.2.1 Geometry 80

6.2.2 Concept of a moving wake profile at the inlet 82

6.2.3 Precursor calculation for the incoming wake 83

6.2.4 Inlet conditions 86

6.2.5 T106A (Low $Re_{2c} = 160000$, Low $Tu = 0.5\%$) 90

6.2.6 T106A (Medium $Re_{2c} = 260000$, Low $Tu = 0.5\%$) . . . 98

6.2.7 T106A (Low $Re_{2c} = 160000$, High $Tu = 4\%$) 101

6.2.8 Conclusion 106

6.3 T106D 107

6.3.1 Geometry 107

6.3.2 Inlet conditions 107

6.3.3 T106D (Low $Re_{2c} = 200000$) 109

6.3.4 Conclusion 113

6.4 N3-60 114

6.4.1 Geometry 114

6.4.2 Inlet conditions 115

6.4.3 N3-60 (High $Re_{2c} = 600000$, Low $Tu = 0.4\%$) 117

6.4.4 N3-60 (High $Re_{2c} = 600000$, High $Tu = 4\%$) 121

6.4.5 Conclusion 126

7 Conclusion and future work **127**

Nomenclature

$\alpha_{1,2}$	inlet $(_1)$ and exit $(_2)$ flow angle
β	spot growth parameter
δ	boundary layer thickness
δ^*	displacement thickness
γ	near wall intermittency
$\hat{n}$	dimensionless spot production parameter
λ	Pohlhausen pressure gradient parameter
μ	dynamic viscosity, $\mu = \nu\rho$
μ_t	turbulent viscosity
ν	kinematic viscosity
ν_t	turbulent viscosity
Ω	rotationrate magnitude
ω	specific turbulence dissipation rate
ρ	density
σ	dimensionless Emmons spot propagation parameter
τ	shear stress
τ	turbulence weighting factor, $\tau = \gamma + \zeta$
τ_{avg}	boundary layer averaged turbulence weighting factor
θ	momentum thickness

ε	turbulent kinetic energy dissipation rate
ζ	free-stream intermittency factor
c	blade chord
C_f	skin friction
C_p	pressure coefficient, $C_p = (p_{01} - p)/(p_{01} - p_{2is})$
c_{ax}	axial blade chord
D	diffusion term
E	destruction term
F	reduced frequency
f_b	bar frequency
F_s	starting function for intermittency
g	blade pitch
g	spot production rate per unit surface area
H_{12}	shape factor
K	local acceleration parameter
k	turbulent kinetic energy
k_l	laminar-kinetic-energy
L	turbulence lengthscale
L_{11}	turbulence longitudinal integral lengthscale
l_{tr}	delay between separation and transition location
M	Mach number
n	spot production rate per unit distance in the spanwise direction
P	production term
p	pressure
Pr	Prandtl number
Re_v	vorticity Reynolds number, $Re_v = y^2 S/\nu$ or $y^2\Omega/\nu$

Re_x streamwise Reynolds number, $Re_x = U_\infty x/\nu$

Re_{2c} Reynolds number based on chord and exit velocity, $Re_{2c} = U_{\text{exit}} c/\nu$

$Re_{\theta t}$ critical momentum Reynolds number

Re_θ momentum thickness Reynolds number, $Re_\theta = U_\infty \theta/\nu$

S strainrate magnitude

s streamwise coordinate

s_b bar pitch

t time

TKE turbulence kinetic energy, scaled with exit kinetic energy

Tu local free stream turbulence intensity

U velocity magnitude

u' velocity fluctuation (streamwise component)

U_b bar speed

U_i velocity components

U_∞ local free-stream velocity

v' velocity fluctuation (wall normal component)

x_t start of transition location

(V)LES (Very) Large Eddy Simulation

AVDR Axial Velocity Density Ratio

CFD Computational Fluid Dynamics

DNS Direct Numerical Simulation

KH Kelvin-Helmholtz

LP(T) Low Pressure (Turbine)

PUIM Prescribed Unsteady Intermittency Modelling

RANS Reynolds Averaged Navier-Stokes Equations

RMS Root Mean Square of a variable

S	space, relative surface length
SST	Shear Stress Transport
T	time, scaled with wake period
TS	Tollmien-Schlichting
ZPG	Zero Pressure Gradient

Preface

I want to start off with an example well known to all, which clearly demonstrates the influence of the boundary layer state to the overall dynamics. For this purpose, I use the example of a tennis ball hit with and without topspin. A ball hit with topspin curves more downward than a ball hit without. The physics are comprehensible for people without experience in the turbomachinery field. This example broadens the topic of this thesis to more general applications of Computational Fluid Dynamics (CFD).

Magnus effect

The flow over an irrotational ball experiences a drag force in the downstream direction, and no lift force in the crosstream direction. If this ball rotates about an axis perpendicular to the flow, the resulting lift force becomes non zero. This is because, due to the rotation, the velocity is increased on one side of the ball, and decreased on the other side, compared to the non-rotating ball. Considering potential effects from the Bernoulli equation, the pressure will decrease on the increased velocity side, and increase on the opposite side (for low Reynolds numbers). This pressure difference induces a lift force different from zero.

In the case of a tennis ball hit with topspin, this results in a downward force on the ball. However it is observed that at low speeds, the topspin has the inverse effect. This can be explained by investigating the boundary layer state more thoroughly. A different boundary layer status on both sides of the ball can induce forces that are much bigger than the Magnus force.

Top spin at different Reynolds numbers

If we determine the Reynolds number of a sphere as $Re = \frac{U_\infty d}{\nu}$, the critical Reynolds number for transition on a smooth sphere is 5×10^5. For a rough sphere it is somewhat lower. A tennis ball has a diameter of 6.5 cm and can be hit at 120 Km/h. Consider a sphere subjected to laminar flow (or turbulent flow with *low* turbulence intensity) with a velocity resulting in a Reynolds number lower than critical. The boundary layer will be of laminar state. At the point of deceleration this boundary layer will separate, and produce a turbulent wake. This is point A on the curve of drag coefficient, in Figure 2. With increasing velocity, the boundary layer status turns turbulent (at the critical Reynolds number) and can resist the deceleration much longer. This results in a more narrow wake, so losses are smaller. This is point B. For even higher Reynolds numbers (C), the point of separation moves upstream again due to the higher deceleration rate.

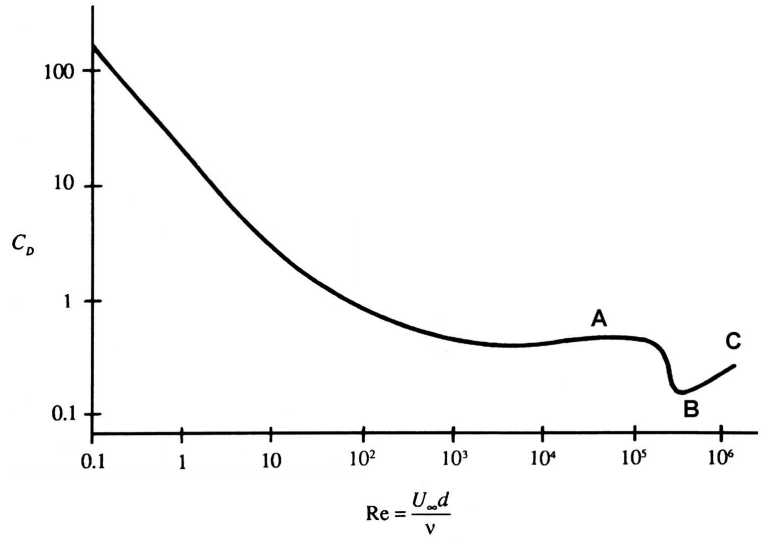

Figure 2: Drag coefficient of a smooth sphere.

At very high Reynolds numbers, the boundary layer is turbulent, and separates immediately after the acceleration phase, independent of the rotation. At lower Reynolds numbers, the rotation will influence the boundary layer state. The rotation alters the velocity *relative to the surface*. A reduced velocity relative to the surface allows the boundary layer to remain laminar. For low Reynolds numbers, the fluctuations are dampened near the wall due to viscous effects. The laminar boundary layer is less resistant to decelera-

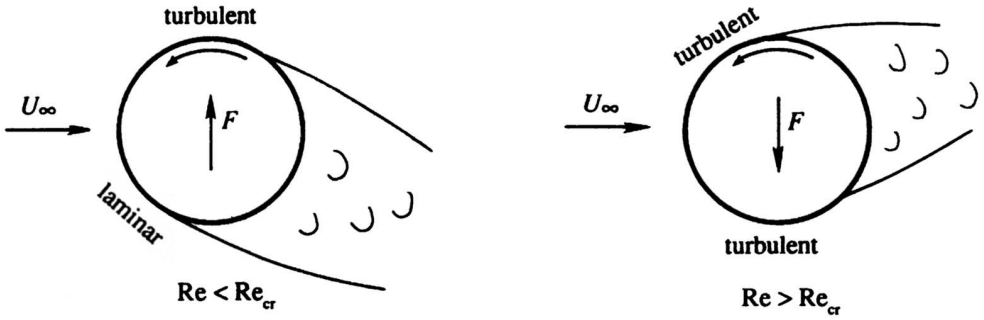

Figure 3: Resulting force F on a tennis ball hit with topspin.

tion and easily goes into separation. To conclude the observations at different Reynolds numbers, we gradually increase the Reynolds number, and observe the separation point:

- At sub-critical Reynolds number, the boundary layer is laminar and separation takes place at start of deceleration.
- At critical Reynolds number, the boundary layer turns turbulent and separation moves much downstream.
- At super-critical Reynolds number, the boundary layer is turbulent and separation moves gradually upstream.

Two situations are now possible, shown in Figure 3. The first one is a ball hit with topspin at a Reynolds number lower than critical. Due to the rotation, this ball will have a turbulent upper boundary layer, and a laminar lower boundary layer. The lower boundary layer will separate upstream of the upper one. As a result, the pressure on the upper side will be lower, and the wake bent downward. The resulting force on the ball is upward. This is the inverse direction of the Magnus effect.

The second situation is a ball hit, with topspin, at a higher than critical Reynolds number. Both upper and lower boundary layer will be turbulent, but the separation point will be different due to the difference in local Reynolds number. The upper side will have a locally higher Reynolds number, resulting from the spin, so the flow will separate more upstream. This is the same direction as the Magnus effect.

Conclusion

More or less independent of the free-stream flow state, the boundary layer can be laminar at low Reynolds numbers. This is a problem for conventional CFD methods which have all been developed for high Reynolds number flow with a turbulent boundary layer. For these conditions the high value of the Reynolds number allows to neglect the molecular viscous terms. Viscous stresses are modelled using a turbulent viscosity much greater than the molecular one. For low Reynolds number flows, this assumption is no longer valid, and more improved turbulence models have to be developed, taking into account the damping of turbulent fluctuations near the wall.

In the Low Pressure (LP) part of a gasturbine, the Reynolds numbers are low. So the suction side boundary layer can be laminar. The impact of wakes from upstream bladerows triggers the boundary layer to turbulence, which prevents it from separating. In this thesis, a method is developed to account for these features in a turbulence model.

Chapter 1

General introduction

Although the topic of transition is general, this work is focused on the simulation of wake-induced transition in the Low Pressure (LP) part of a gasturbine engine. Gasturbine engines consist of a compressor, a combustion part and a turbine. The low pressure part of the turbine produces the main part of the thrust of a gasturbine engine. An increase in efficiency in the LP turbine results immediately in an increase in the engine efficiency. Todays efficiency levels reach up to 90%. So increases in efficiency are increasingly hard to obtain. One way to do this is by reducing the LP turbine weight. The LP turbine is the largest and most heavy part, and can reach up to one third of the total engine weight. A way of decreasing its weight is to reduce the number of blades per stage. On the other hand, an increased blade loading may allow a reduction of the number of LP stages. For a given stage loading, each blade must support a higher aerodynamic load. But care has to be taken that the losses don't increase. Stage losses are mainly due to profile losses in the boundary layer.

In order to further increase the loading of LP blades in a gas turbine, periodic impact of wakes coming from previous blade rows is used to force transition. Without wake-induced transition, the boundary layer at the suction side would massively separate in high load conditions, resulting in high losses. Under the impact of wakes, the boundary layer turns turbulent. In between wakes, the boundary layer relaxes to laminar and even separated state. Due to the transition to turbulence, the separation disappears completely or periodically, and this makes the time averaged losses decrease.

Losses are often evaluated based on the trailing edge momentum thickness. The momentum thickness θ is defined such that $\rho U^2 \theta$ is the momentum loss due to the presence of the boundary layer. This loss is due to viscous dissipation in the boundary layer. The loss over the passage can be approximated by

$$\text{Loss} \sim \frac{\theta_{SS} + \theta_{PS}}{g \cos \alpha_2} \tag{1.1}$$

This is simply the comparison of the lost momentum section with the crosstream exit (subscript 2) section.

Using the Von Karman momentum integral, we see that the momentum thickness is basically the integral of the skin friction over the surface (streamwise coordinate s).

$$\frac{d\theta}{ds} + \frac{\theta}{U_\infty} \frac{dU_\infty}{ds} (2 + H_{12} - M_\infty^2) = \frac{C_f}{2} \tag{1.2}$$

The second term in the left hand side includes the influence of pressure gradient and boundary layer status. Acceleration is seen to reduce the growth of the momentum thickness. This is the case for the pressure side. The suction side has an acceleration followed by a deceleration. In the deceleration phase, θ grows rapidly, and transition is enhanced. As consequence, the suction side loss will be predominant. In case of a separation bubble on the suction side, the skin friction over the separation is low, as is the adverse pressure gradient, so using Eqn. 1.2, θ doesn't increase much. However, after reattachment, the mixing losses are big, and contribute to a substantial increase in momentum thickness. If the reattachment is located at the trailing edge, the mixing losses will occur downstream of the profile, and have to be added to θ_{SS} to evaluate the loss over the cascade.

Since an attached turbulent boundary layer results in higher losses than an attached laminar one, the periodic wake passage which enhances transition is not always beneficial. Schulte [70] proposes the term *Wetted Area* for the area on a Space-Time diagram that is covered by turbulent flow. The space coordinate is the normalized streamwise suction surface distance. The time coordinate is normalized by the wake passing period. For a high reduced wake frequency, the suction side is almost constantly covered by wake-induced transitional flow. This leads to high losses. Benefit from the wake can be expected from periodical suppression of a separation bubble. After wake impact, the boundary layer is **becalmed**, transition is inhibited and separation is prevented for some time. As a result, the time averaged separation bubble is much reduced. Based on the principle of minimizing the wetted area, Schulte proposed an optimum wake frequency when the end of the calmed region has

reached the trailing edge by the time the turbulent path of the next wake and spot has arrived at the same point C, as shown in Figure 1.1.

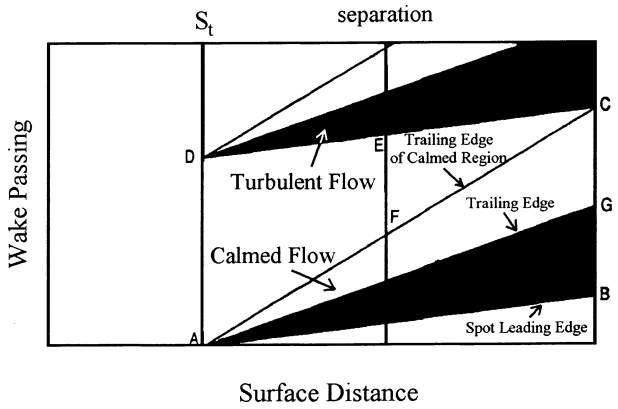

Figure 1.1: Space-Time diagram illustrating the minimum loss hypothesis of Schulte.

Other options, aside periodic wake impact, to reduce the losses are clocking and the use of ribbles or roughness on the surface. Recent LP blades often have a complex 3D design. These blades lead to an improved efficiency, but do not always lead to an economic optimum since their manufacturing cost is considerably higer.

The downstream bladerow also has an influence on the upstream one. This is called potential effect. When two consecutive stator rows have an equal or a multiple number of blades, the relative position of the blades can be optimized for minimal losses in the intermediate rotor passage, this is called clocking.

Further increases in lift (ultra-high-lift) result in a higher adverse pressure gradient on the suction side. The incoming wakes may not be strong enough to suppress the large separation bubble, especially at low Reynolds numbers. The profile becomes more dependent on the Reynolds number. Adding roughness on the suction side can enhance (wake-induced) transition in the deceleration phase, and thus reduce the separation. Zhang et al. [98] demonstrated this for an ultra-high-lift profile on low speed conditions. For such a profile, the separation bubble doesn't reattach under the wake impact. By adding a roughness strip on the surface, the transition is enhanced, and reattachment is seen under the wakes, followed by calming. The key point is to prevent roll-up of the separation bubble under wake impact. On the other hand, if the roughness step is too big, transition starts immediately after the strip, and the wetted

area is very big. So, the strip has to enhance rather than start up transition. Nevertheless, the wetted area increases with the application of a strip, so the most benefit is seen when the profile is aft-loaded. Essentially the same profile loss can be achieved as for a high-lift profile. The stage loss is reduced since it can consist of less blades. These conclusions are extended to high speed conditions on the same ultra-high-lift pressure distribution by Vera et al. [85]. They show that small spanwise strips resulting from the manufacturing process act as negative steps that can control the size of the separation bubble. It is demonstrated that this results in lower loss than for the polished profile.

In a LP turbine, separation is first observed near the hub. A 3D design of the blade can redistribute the load over the blade such that an optimal load is achieved over the entire span of the blade.

On the numerical side, an increasing amount of academic simulations are performed on highly loaded profiles sometimes with wake impact using LES. Contrary, in industry, simulations are performed using algebraic prescription of steady correlations. To fill the gap between these extremes was the goal of the EC-project UTAT, in which the present authors participated. Within the RANS context, three modelling techniques were outlined: the use of linear stability theory e^N, the use of non-linear eddy viscosity models and the use of conventional turbulence models with an additional equation for intermittency. The latter approach is the topic of this thesis.

An integrated e^N model has been proposed by Hu and Fransson [27]. The modelling procedure is intended to simulate transition induced by Tollmien-Schlichting waves, but is extended to be used for higher levels of free-stream turbulence. Still, by construction, the model is not capable of capturing the influence of an increase in free-stream turbulence intensity above three percent. The model is seen to work well for low and medium Reynolds numbers, but shows deficiencies for high Reynolds numbers. The general trend is that deficient transition predictions are downstream of the experiment.

Non-linear eddy viscosity models are proposed by Lardeau and Leschziner [34, 36]. These are turbulence models that are extended to bring in the influence of rotation. Often, also low-Reynolds number physics are taken into account. They obtain reasonably good results for the unsteady test case T106A with low background turbulence intensity. To incorporate the effect of a higher background turbulence intensity, they introduce a supplementary algebraic equation for intermittency. This limits the general applicability of this technique.

The model proposed in this thesis describes the modeling of transition with standard turbulence models, in combination with two equations for intermittency. The turbulence model predicts transition too much upstream. But its influence on the flow solver is weighted with an intermittency factor shifting transition to the physical location.

We have to mention some similarity with the prescribed unsteady intermittency approach (PUIM) proposed by Addison, Schulte and Hodson. Unsteady transition correlations are solved and prescribed algebraically on the computational domain. The result toward the flow solver is similar, but we are confident that our approach can be easier implemented in complex geometries.

The coordinate system used in the major part of this thesis is illustrated in Figure 1.2. The x-axis is in the streamwise direction. The y-axis is the wall-normal direction. The third dimension z-axis, not resolved in the simulations, is the spanwise direction.

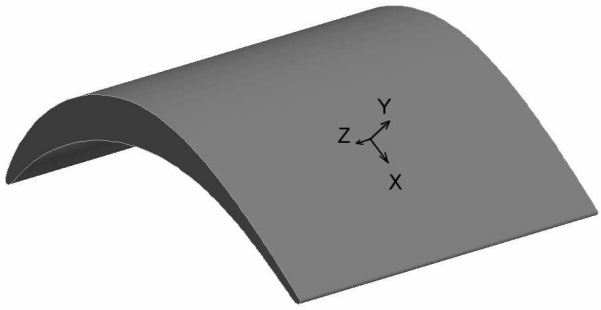

Figure 1.2: Coordinate system.

Chapter 2

Literature review

2.1 Transition

A large part of the boundary layer of an LP turbine blade has a laminar state, this is a result of the low Reynolds number. The change from a laminar to turbulent state is called transition. The inverse case of a turbulent boundary layer changing toward a laminar one is called relaminarisation. Transition results from an excitation and amplification of disturbances in the laminar boundary layer. We can distinguish different modes of transition.

2.1.1 Natural transition

Natural transition occurs at very low turbulence levels. When the Reynolds number (based on streamwise coordinate) exceeds a critical value, the laminar boundary layer develops exponentially growing eigenmodes. These are 2D Tollmien-Schlichting (TS) waves, which are traveling at $0.3 - 0.35\,U_\infty$. As they convect downstream, their amplitude increases and spanwise distortions of the flow vortical structure develop in an increasingly three-dimensional and non-linear manner. Finally, they burst into turbulent spots that grow as they travel downstream. When the spots have merged together, the boundary layer is fully turbulent, and transition is complete.

The first 2D, linear stages of this instability amplification are described by

the *Orr-Sommerfeld equation*. This describes the stability of a boundary layer subjected to small perturbations. It comes out that below a critical Reynolds number all perturbations are stable. At higher Reynolds numbers a band of frequencies are amplified in an unstable way. An other conclusion is that for high Reynolds number a frictionless stability equation is obtained. From this expression, Rayleigh deduced an important theorem known as the *point of inflexion criterion*. It stipulates that the velocity profiles presenting an inflexion point are unstable; which explains why an adverse pressure gradient has a destabilizing effect on the boundary layer.

The point of natural transition is usually determined using the e^N method developed by Smith and Gamberoni [71]. In this method, which is widely used in aircraft industry, e^N is equal to the amplification ratio of the most unstable wave at each streamwise position. Onset is then presumed to occur at the position where the amplification ratio reaches an experimentally determined critical value. The critical value of N is usually assumed to be equal to 9 at very weak turbulence intensities found in external aerodynamics. In a raised free-stream turbulence intensity environment, the critical value of N should be a function of the disturbance level because higher disturbances will require less amplification to start transition. A classical relation was proposed by Mack [43] for turbulence intensity ranging between 0.1% and 1%:

$$\text{amplification ratio} = \frac{A}{A_0} = \exp[N] \tag{2.1}$$

$$N = -8.43 - 2.4 \ln Tu \tag{2.2}$$

2.1.2 Bypass transition

Under free-stream turbulence intensities of order 1% or more, it is observed experimentally that transition occurs rapidly, bypassing the Tollmien-Schlichting route. This results in the direct generation of turbulent spots. This is often the case in turbomachinery where high levels of turbulence act on the boundary layer. The fluctuations in the boundary layer are forced and do not come from a natural instability of the flow. Diffusion of turbulence into the boundary layer is not the main mechanism. Volino [87] argues that transition results from a response of the near-wall viscous layer to the pressure fluctuations imposed in the freestream by means of a **splat mechanism**. According to this splat mechanism, originally discussed by Bradshaw [9], large free-stream eddies hit the boundary layer. So, a negative v' fluctuation in the free stream

compresses the boundary layer momentarily forcing high speed fluid closer to the wall (positive u'). Once the free-stream eddy passes, the boundary layer rebounds to its original state, with little net effect. According to Johnson et al. [31], if the instantaneous velocity in the near-wall drops below 50 percent of the mean, an instability arises, which results in local separation of the flow. It is the normal velocity v' associated with this separation that is believed to initiate the turbulent spot. The addition of v' to the already present u' generates Reynolds shear stress. Goldstein and Wundrow [21] prove this theory using inviscid rapid-distortion theory. It shows that vortex stretching selectively amplifies the low-frequency component of the motion. The high frequencies are moved out of the boundary layer, first into a kind of edge layer and then into the free-stream. Irrespective of the free-stream turbulence intensity level, the dominant streamwise fluctuations are of the Klebanoff type, are very elongated in the streamwise direction, and are very narrow in the spanwise direction. These are often named 'streaks'. It is shown that when the RMS velocity fluctuation is a little over 10%, the maximum velocity fluctuation is nearly equal to 50% at this point, and thus large enough to produce localized breakdown of the boundary layer. This causes a local separation.

Johnson [30] among others [47, 45] have shown that the pretransitional fluctuations, induced primarily by the pressure fluctuations associated with the free-stream turbulence, grow more or less *linearly* in the streamwise direction. Some variation in the induced fluctuations has a linear effect on the streamwise location where the critical fluctuation level is achieved. In other words, the location where fluctuations break down into turbulent spots has a streamwise extension. For natural transition induced through Tollmien-Schlichting waves, transition begins also when a critical level of the fluctuations is achieved, but T-S waves grow *exponentially* once a critical boundary layer Reynolds number is exceeded. So, spots are generated over a relatively short streamwise distance.

There are a number of direct numerical simulations that calculate a laminar boundary layer under the effect of free-stream turbulence. Before going into the discussion of these simulations, a short description of free-stream turbulence is given.

Without production due to mean velocity gradients, homogeneous turbulence decays. This is achieved in wind-tunnel experiments by passing a uniform stream through a grid (velocity U_0 in the x direction). In the frame moving with the mean velocity, the turbulence is with good approximation homogeneous, and evolves with time ($t = x/U_0$). Experiments of Comte-Bellot

and Corrsin [15] show that turbulent kinetic energy k decays as a power law written as

$$\frac{k}{U_0^2} = A\left(\frac{x - x_0}{M}\right)^{-n} \tag{2.3}$$

where x_0 is the virtual origin. Nearly all data in literature are consistent with $n = 1.3$ and $x_0 = 0$. M is the mesh spacing of the grid, and A varies widely depending on the geometry of the grid and Reynolds number. Assuming A, M and $U_0 = 1$, Eqn. (2.3) becomes $k = \frac{1}{x^{1.3}}$. Shortly downstream of the grid, the decay rate of k is high, but decreases downstream. The smaller, faster motions decay rapidly, leaving behind the larger, slower motions. So, inversely to k, the length scale L increases downstream of the grid. In the moving frame, Eqn. (2.3) can be written

$$k(t) = k_0\left(\frac{t}{t_0}\right)^{-n} \tag{2.4}$$

Because of lack of production and diffusion, the equation for k becomes

$$\frac{dk}{dt} = -\varepsilon \tag{2.5}$$

This shows that ε also decays as a power law

$$\varepsilon(t) = \varepsilon_0\left(\frac{t}{t_0}\right)^{-(n+1)} \tag{2.6}$$

It can now be verified that the length scale L increases with time, and the Reynolds number $k^{1/2}L/\nu$ decreases with time.

$$L \equiv \frac{k^{3/2}}{\varepsilon} \sim \left(\frac{t}{t_0}\right)^{0.35} \tag{2.7}$$

$$\frac{k^{1/2}L}{\nu} \sim \left(\frac{t}{t_0}\right)^{-0.3} \tag{2.8}$$

In the approximation of homogeneous turbulence over a flat plate boundary layer, the decay rate is affected by the distance between the grid and the leading edge, and by the grid geometry. This implies that in a numerical simulation not only the inlet level of k has to be determined, but also the value of ε (or ω). The value of the turbulence intensity on the boundary layer edge is used in combination with a transition correlation, eg. Mayle, Abu-Ghanam, ... to determine the transition location. Some researchers have found that anisotropy can affect the transition location. This cannot be taken into account with linear eddy viscosity models.

The turbulent integral length scale can be calculated based on auto correlation functions. When introducing the *ensemble average* operator (over N repetitions) defined by

$$\langle U \rangle \equiv \frac{1}{N} \sum_{i=1}^{N} U^{(n)} \tag{2.9}$$

we can construct the *autocovariance* in one point

$$R(s) \equiv \langle u(t)u(t+s) \rangle \tag{2.10}$$

or the *two-point correlation* at one time instant

$$R_{ij}(\mathbf{r}, \mathbf{x}, t) \equiv \langle u_i(\mathbf{x}, t)u_j(\mathbf{x}+\mathbf{r}, t) \rangle \tag{2.11}$$

where $u(t) = U(t) - \langle U \rangle$ is the fluctuation. The *longitudinal integral lengthscale* is defined as

$$L_{11}(t) \equiv \int_0^\infty \frac{\langle u_1(\mathbf{x}+\mathbf{e_1}r, t)u_1(\mathbf{x}, t) \rangle}{\langle u_1^2 \rangle} dr \tag{2.12}$$

and is characteristic of the larger eddies. For grid turbulence, L_{11} increases downstream due to the fast dissipation of the small scales.

In the boundary layer, turbulent fluctuations coming from the free stream are damped by wall presence, until at some location they break down into turbulence. A variety of experiments show the appearance of fluctuations upstream of the transition location. These fluctuations are mostly in the streamwise component u'. This is shown in a direct numerical simulation of a laminar boundary layer under the influence of a turbulent free stream by Jacobs and Durbin [28]. These computations are typically done in a rectangular region with a lower non-slip wall and with a Blasius boundary layer introduced at the inlet. So, the leading edge is not included, and the calculation starts with a boundary layer of finite thickness. In Figure 2.1 they show streamwise (u') velocity fluctuation contours in three planes parallel to the wall: (a) is in the free stream, (b) is at the upper edge of the boundary layer, and (c) is near the surface. A qualitative change from isotropic turbulence in the free stream to highly elongated streaks (also named 'puffs') near the wall is observed as the plane moves toward the wall. In the near-wall plane (c), a turbulent spot which moves into the turbulent zone is visible on the downstream half of the plane. In Figure 2.2, they show streamwise u' velocity fluctuations (a) and wall normal v' velocity fluctuations (b), on a plane located in the boundary layer, parallel to the wall. It can be seen that v' fluctuations only have a non zero value in the turbulent spots.

Mayle and Schulz [47] have proposed a model for these streamwise fluctuations. Their main idea is that the laminar fluctuations preceding transition

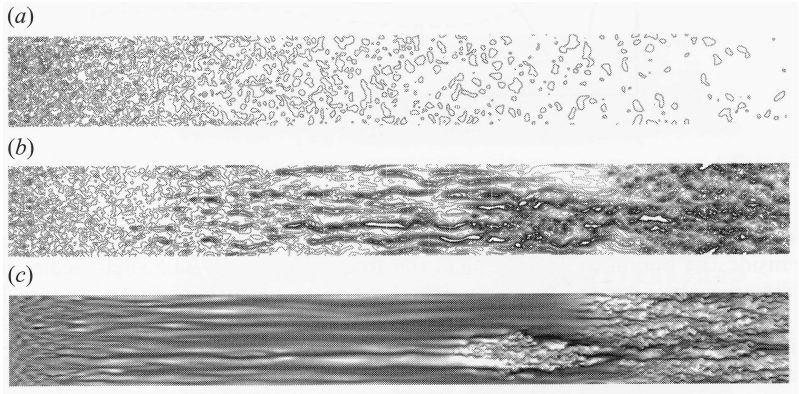

Figure 2.1: Streamwise (u') velocity fluctuation contours in three planes parallel to the wall: (a) is in the free stream, (b) is at the upper edge of the boundary layer, and (c) is near the surface. From the calculation by Jacobs and Durbin [28].

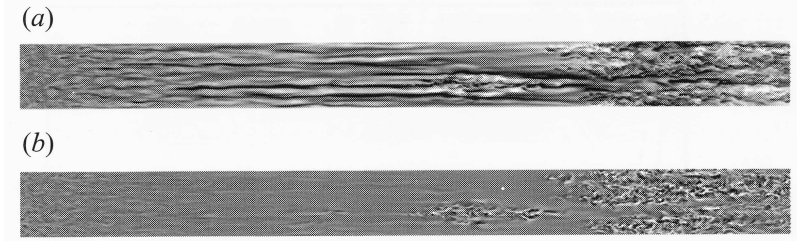

Figure 2.2: (a) Streamwise u' velocity fluctuations and (b) wall normal v' velocity fluctuations. From the calculation by Jacobs and Durbin [28].

are primarily caused by the work of the imposed fluctuating free-stream pressure forces on the flow in the boundary layer. The turbulence-production is zero since it is assumed that the shear stress is zero. The remaining term responsible for production of fluctuations in the boundary layer is the pressure diffusion, which is usually neglected in eddy viscosity models or assumed assimilated in the gradient-diffusion approximation. Based hereon, the production term in their *laminar-kinetic-energy equation* has the form of a forcing function (first term on right hand side)

$$u\frac{\delta k_l}{\delta x} + v\frac{\delta k_l}{\delta y} = C_\omega \frac{U_\infty^2}{\nu}\sqrt{k_l \cdot k_\infty}\exp(-y^+/C^+) + \nu\frac{\delta^2 k_l}{\delta y^2} - 2\nu k_l/y^2 \qquad (2.13)$$

Two possible mechanisms for the generation of these streaks in boundary

layers subjected to free-stream turbulence are described in Brandt et al. [10]. First, streak generation caused by the diffusion and/or propagation of a free-stream **streamwise vortex** into the boundary layer. This occurs near the leading edge. A streamwise vortex entrains low momentum fluid into the upper part of the boundary layer, and high momentum fluid into the near wall part. This forms a low-speed and a high-speed streak. Downstream of their generation, the streaks get continuous forcing from the free-stream low-frequency vortices. Their growth is in a linear way. Zaki and Durbin [95] show that only low-frequency fluctuations, relative to the boundary layer size, can enter. This is the case near the leading edge. Downstream, the boundary layer has increased, and the same frequency becomes high relative to the boundary layer, and cannot enter anymore.

Second, if the boundary layer doesn't contain fluctuations, a non-linear interaction of oblique modes in the free stream is necessary to generate fluctuations in the boundary layer. A *shear sheltering* process prevents the free-stream fluctuations to enter the boundary layer. The shear sheltering is obvious in Figure 2.1. For the streamwise component, it is shown that the small scale free-stream fluctuations in (a) are only visible inside the boundary layer in the leading edge part (c). Downstream, they develop streaks, but the random isotropic fluctuations from the upper free stream (a) is not longer reflected in random fluctuations in the boundary layer. Figure 2.2b adds the normal component in the boundary layer to the picture. Since this component doesn't contain the steaks, in between the leading edge region and the appearance of spots, the the normal fluctuations disappear as a result of the shear sheltering.

In gasturbine applications, the fluctuations enter the boundary layer near the leading edge of the blade, so the first mechanism is observed. This is also the case in the flat plate boundary layer calculation by Wu et al. [93]. Moreover, in these simulations, the influence of incoming wakes on the laminar boundary layer is investigated. Because of their generation mechanism, the low speed streaks are located in the upper part of the boundary layer. They observe breakdown in wake-induced bypass transition usually in the outer part of the boundary layer, so on the low speed streak. Further, they mention that not all streaks lead to breakdown. They discovered that when breakdown occurs in the outer layer, where the convection speed is large, which is here the case, the arrowhead of the spot points upstream. This is different from the Emmonds spot, which are usually stimulated by forcing at the wall. In this case, breakdown occurs near the wall, and the arrowhead points downstream.

In their numerical simulation of a boundary layer flow, but without in-

coming wakes, Brandt et al. [10] investigated the influence of the free-stream turbulence integral lengthscale on the transition location. For their flat plate calculation they found that the transition location moves upstream by increasing the integral lengthscale for a constant free-stream turbulence intensity level. This can be seen in Figure 2.3, which shows free-stream Tu and skin friction values of the numerical flat plate simulation. This conclusion confirms the trend observed in the experimental study of Jonáš, Mazur and Uruba [32]. The turbulence decay decreases for increasing lengthscales. The developed streaks are streamwise elongated regions of high and low streamwise velocity with in between a strong shear layer (due to the velocity difference). The breakdown into turbulent spots is shown to be related to local instabilities of these shear layers.

In a very recent study, Lardeau et al. [38] have numerically investigated the effect of anisotropy in the free-stream turbulence on a flat plate boundary layer. They also investigated what happens if the boundary layer contains no perturbations. The hypothesis proposed by Mayle and Schultz [47] that the pre-transitional fluctuation energy is effected by way of pressure diffusion and that shear production is zero could not be proved. In their well resolved LES simulation of a flat plate, Lardeau et al. applied three different boundary conditions:

- S_{iso} isotropic turbulence is prescribed at the free-stream and at the inlet plane, including within the boundary layer which is prescribed at the inlet
- S_{fs} isotropic turbulence is prescribed, but only above the Blasius boundary layer
- S_{uu} only the streamwise fluctuations from S_{iso} are prescribed

The free-stream turbulence intensity for these cases, and their result in skin friction are shown in Figure 2.4. Without boundary layer fluctuations, the transition location is shifted far downstream, although a higher free-stream turbulence intensity is used in this case. This is also observed by Brandt et al. [10] who argue that without perturbations in the boundary layer, a shear sheltering process prevents the free-stream fluctuations from entering the boundary layer. In the other two cases, the perturbations introduced inside the boundary layer create long streamwise structures, which are receptivity sites for the fluctuations entering the boundary layer. These streamwise structures are also visible upstream of the transition location, and the location where

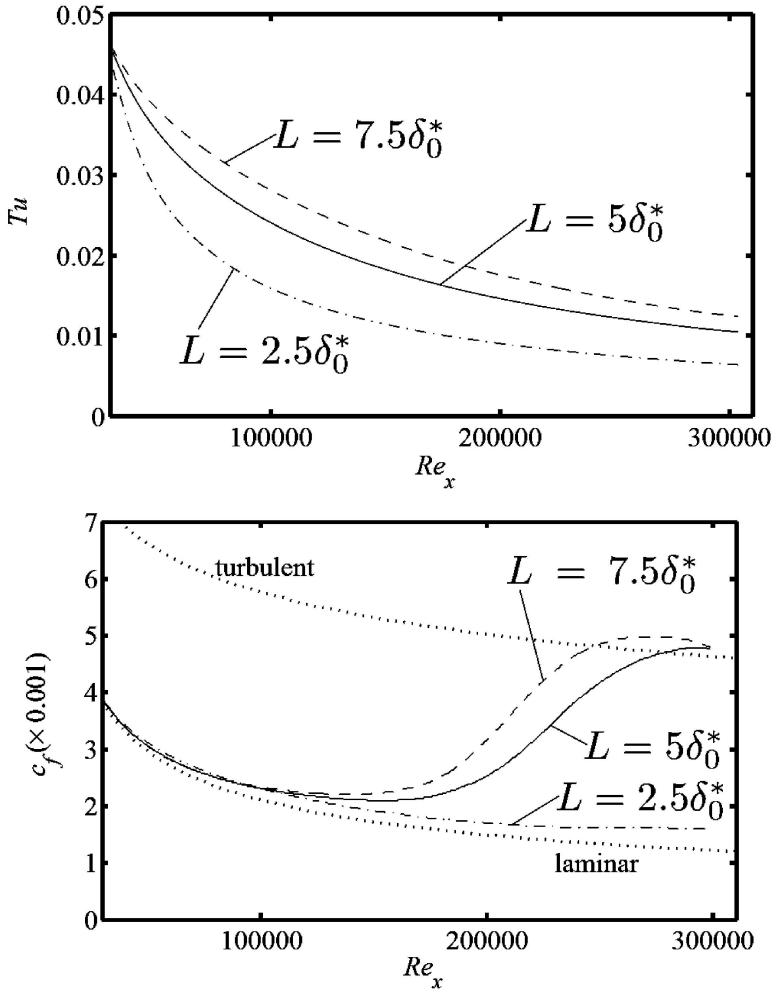

Figure 2.3: Streamwise evolution of the free-stream turbulence intensity (upper) and the skin-friction coefficient (lower) in the numerical simulation of Brandt et al. [10] for different values of the integral lengthscale.

they break down into turbulent spots corresponds roughly to the location at which the skin friction rises. It can also be seen that the suppression of lateral free-stream fluctuations (S_{uu}) does inhibit the transition process. Contrary to the zero shear-induced-production assumption from Mayle and Schultz, Lardeau et al. find fairly high levels of $-\langle uv \rangle / k$ (in the order of 30%-50% of the level of a fully turbulent boundary layer), but declining sharply as the wall is approached. These levels are drastically reduced in the S_{fs}-case. It is these relatively low levels of shear stress that create the elevation of fluctuation

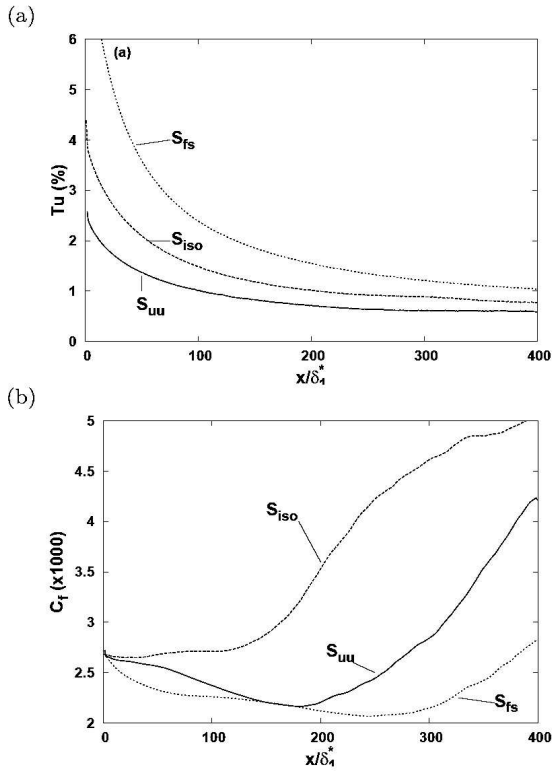

Figure 2.4: Streamwise evolution of (a) the free-stream turbulence intensity and (b) the skin-friction coefficient in the LES simulation of Lardeau et al. [38]

energy through the mechanism of shear production.

In turbomachinery cases, the perturbations enter the boundary layer at the leading edge region of the blade. So the S_{fs} case is not relevant here. *Kinematic* pressure fluctuations, associated with the larger eddies, will amplify these perturbations. Once the boundary layer thickness is large enough, these can form turbulent spots. The velocity fluctuations associated with *acoustic* pressure fluctuations are too small to trigger the perturbations.

There is some debate about the mechanism by which the streaks breakdown into turbulence. Brandt et al. [10] show that when a low speed streak is caught up by a high speed streak, they develop a streamwise waviness. Fluctuations in spanwise and wall normal direction appear mainly on the low speed streak in a quasi-steady periodic pattern. This is illustrated in Figure 2.5. Breakdown is attributed due to Kelvin-Helmholtz like instability

of inflectional wall-normal profiles. Jacobs and Durbin [28] argued that the low speed streak (negative jet) is lifted further upward by the high speed streak as a result of large scale free-stream effects, and is the disrupted by the smaller scales from the free stream. Negative jets overlying positive jets seems to be the most unstable. They contain an inflectional profile.

In recent work, Zaki and Durbin [95] were able to confirm this assumption. They performed numerical simulations with only a *pair* of inflow modes. Only the combination of a low-frequency and a high frequency mode completes the full transition process. The low-frequency mode is able to penetrate the boundary layer near the leading edge, and produces the streaks (named Klebanoff mode or breathing mode in this work). These streaks break down to turbulence if there is also a high-frequency mode in the free-stream. This high-frequency mode is not able to penetrate deeply into the boundary layer, but can reach the negative jets which are lifted away form the wall, toward the boundary layer edge. An inflectional velocity profile exists along the streamwise overlap length of the end of a negative jet with the end of a positive jet. Short wavelength instabilities of Kelvin-Helmholtz type are triggered by the high-frequency free-stream disturbance in the streamwise extent of the inflectional profile.

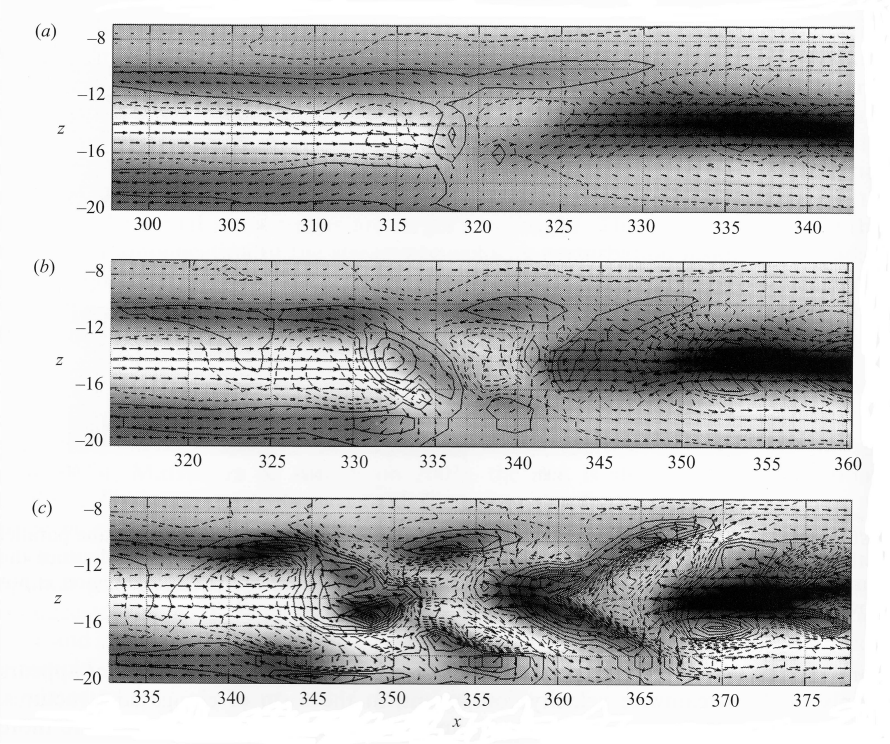

Figure 2.5: Time sequence ($a \rightarrow b \rightarrow c$) showing the streak breakdown in a plane parallel to the wall. Background: contours of streamwise perturbation velocity u' from negative values (dark) to positive (light). Velocity vectors are the perturbation vectors. From the calculation by Jacobs and Durbin [28].

2.1.3 Separated flow transition

A laminar boundary layer subjected to an adverse pressure gradient may separate. In highly loaded LP turbine blades this can occur upstream of transition. The transition then takes place in the separated shear layer. Turbulent reattachment occurs by a turbulent entrainment effect. If the transition is too slow the boundary layer won't reattach.

In the separated free shear layer, Kelvin-Helmholtz instability waves develop along the line of maximum vorticity. Due to rolling over and pairing of the Kelvin-Helmholtz vortices, subharmonic fluctuations with half the frequency are formed. The production of turbulence is related to the appearance of the subharmonic fluctuations. The transition point corresponds to the point of maximum displacement of the bubble, since downstream, the turbulent mixing process enhances momentum exchange across the shear layer.

It is observed that separated transition takes place rapidly over an extremely short transition length. This is because the separated shear layer has considerably less damping capability compared to the attached boundary layer. This is typical for a *short* bubble. A sketch is shown in Figure 2.6. If the Reynolds number is lowered, the turbulent entrainment process can no longer force the boundary layer to reattach. The bubble *bursts* into a *long* bubble. The separation bubble extends more over the airfoil, which strongly reduces the velocity peak in the pressure distribution. Since this also reduces the adverse pressure gradient, the reattachment may eventually take place. This bursting process is associated with a strong increase in losses, and a reduction of the turning angle of the flow. This is experienced by Zhang et al. [97] on an new ultra-high-lift U2 blade with an aft-loaded profile. In Figure 2.7, for the steady case at the lowest Reynolds number, the transition is not strong enough to reattach the boundary layer, this results in *a long bubble with complete separation.*

2.1.4 Relaminarisation

Due to strong acceleration, vorticity is damped through viscous effects. Mayle [46] suggests that transition cannot take place if the acceleration parameter $K = \nu/U_\infty^2(dU_\infty/ds) > 3 \times 10^{-6}$.

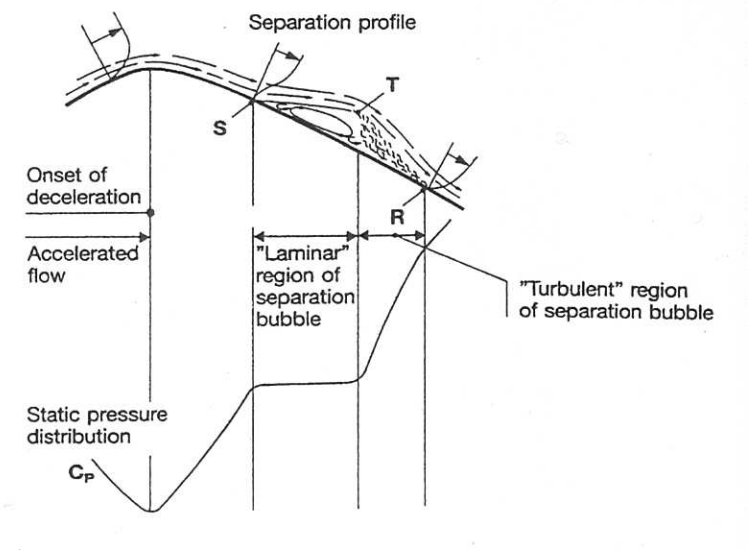

Figure 2.6: Idealized view of the separation bubble (Horton-Roberts).

2.1.5 Turbulent spot and the Emmons theory

Turbulent spots are islands of turbulence surrounded by laminar flow. In normal direction they cover the entire boundary layer from the wall to even some part into the free stream. Schubauer and Klebanoff [69] provided a detailed description of the turbulent spot under zero pressure gradient flow conditions. As illustrated in Figure 2.8, the spot has a triangular shape with a half-angle α of about 11°, and different convection velocities of its leading and trailing boundaries, respectively $0.88\,U_\infty$ and $0.5\,U_\infty$. Due to this velocity difference, the spot grows while maintaining a self-similar shape. Because the spots spread longitudinally and laterally, spots originating from different locations eventually merge to form a continuously turbulent boundary layer. The growth of the spot arises from two processes. On one hand, the spot entrains fresh irrotational fluid from the freestream and from the ambient boundary. On the other hand, eddies inside the spot induce perturbations in the surrounding laminar boundary layer. This is the case along the leading edge of the spot, and explains the strong lateral growth of the turbulent region.

A spot is followed by a calmed region in which the wall shear stress gradually (exponentially) decreases toward the laminar level again. The trailing edge of the calmed region has a velocity of $0.3\,U_\infty$. The calmed region is a laminar-like zone, but has a fuller velocity profile. The calmed region prevents

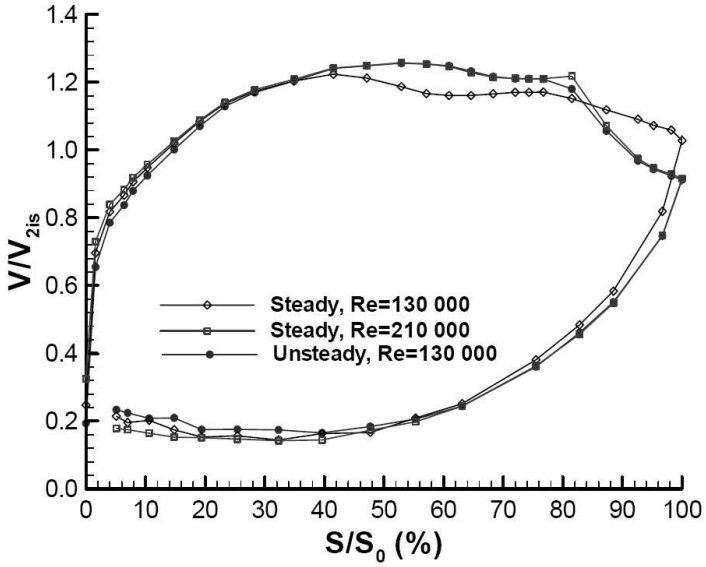

Figure 2.7: Illustration of short and long bubbles by the pressure distribution measured by Zhang [97].

the formation of new instabilities, and is not accessible to Tollmien-Schlichting waves originating upstream of the spot inception because the velocity of the calmed region trailing edge exceeds the propagation velocity of the TS wave. As the wall shear stress relaxes to the laminar level, the calmed region loses its stabilizing property. The calmed region can be terminated by growth of a neighbouring turbulent spot covering it or by strong bypass transition events. Recent work from Gostelow [84] indicates that in a turbomachinery environment, the calming effect remains at work even when its domain coincides with that of the following turbulent patch. This has the effect of reducing the violence of the turbulence and therefore of continuing the stabilization of the flow.

At any point in the transition zone, the boundary layer constantly changes between a laminar and a turbulent (followed by a calmed) state. The probability or fraction of time that it will be turbulent increases toward the rear of the transition zone. This gives an intermittent character to transition as depicted by Emmons [20]. The *intermittency* γ is equal to zero for laminar flow and is unity for turbulent flow. The classic smooth transition from laminar to turbulent results from a time average of the intermittent change between laminar and turbulent properties at any point along the transition zone.

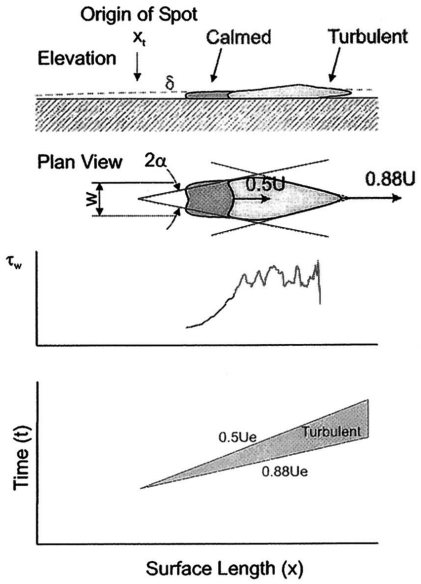

Figure 2.8: Schematic of spot.

Relying on statistical theory and using some assumptions of spots, Emmons models transition and so determines the intermittency distribution. He assumed that spots have a simple wedge-like geometric plan which does not vary across the height of the boundary layer. He further assumed that within the spot, the flow is fully turbulent and that outside, it can be considered as laminar. When two spots merge, they simply form a larger area of turbulent flow. Consider a transitional boundary layer on a (x, z) surface as shown in Figure 2.9 where the free-stream flow is in the x direction, and time t. Emmons model depends on the volume of dependency V of the point of interest $P(x, z, t)$. This volume in space and time contains all the points which could have been the origin of a turbulent spot, which subsequently passed over point $P(x, z, t)$. If turbulent spots are produced at a position $P_0(x_0, z_0)$ at the rate $g(P_0)$ per unit surface area, then the fraction of time the flow at P is turbulent corresponds to the fraction of time turbulent spots produced at P_0 pass over P. Of course when P is covered by a turbulent spot, spots produced at all other locations and time that can also cover P cannot be counted. Only point P_0 lying in the volume of dependency V can produce a turbulent spot over P. It was shown by Emmons that the intermittency can be calculated as:

$$\gamma(P) = 1 - \exp\left[-\int_V g(P_0)\, dx_0 dz_0 dt_0\right] = 1 - \exp\left[-\int_V g(P_0)\, dV_0\right] \quad (2.14)$$

Eqn. (2.14) means that the intermittency can be determined if the spot formation parameter $g(P_0)$, which governs the rate and location of formation of turbulent spots, and the geometry of the volume of dependency V, which is defined by the spreading behaviour of the individual turbulent spots, can be specified.

The general form of Eqn. (2.14) remains unchanged whether the flow is unsteady or steady.

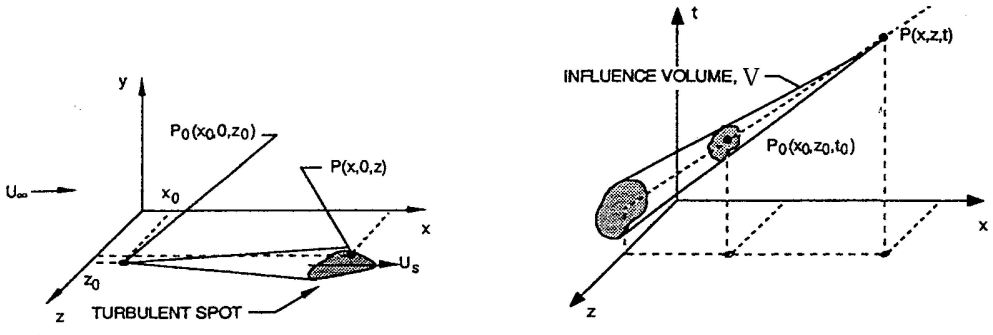

Figure 2.9: Coordinate sysytem for a turbulent spot on a surface and influence volume V for a point P.

Concentrated breakdown

Narasimha [55] showed that in steady flow, the *spots form at a preferred streamwise location randomly in time and in cross-stream position.* This means that no breakdowns occur on a flat plate before a certain streamwise location or much further downstream. This may be identified with the onset of transition x_t. Upstream of x_t, no spots are able to form, while downstream of x_t, the formation of spots is inhibited by calmed regions following spots which were created at x_t. The form of the source-rate function is thus a Dirac delta function around the location x_t:

$$g(P_0) = n\,\delta(x_0 - x_t) \tag{2.15}$$

with n being the turbulent spot production rate per unit distance in the spanwise (z) direction. The volume of dependency is now based on the distance (downstream) to the start of transition ($x_0 - x_t$). Eqn. (2.14) can thus be simplified:

$$\gamma(P) \quad = \quad 1 - \exp\left[-\int_V g(P_0)\,dx_0 dz_0 dt_0\right]$$

$$
\begin{aligned}
&= 1 - \exp\left[-\int g(x_0)\left(\int\int dz_0 dt_0\right) dx_0\right] \\
&= 1 - \exp\left[-\int g(x_0)\left(\frac{\sigma}{U_\infty}(x_0 - x)^2\right) dx_0\right] \qquad (2.16)
\end{aligned}
$$

where σ is the dimensionless Emmons spot propagation parameter which depends on the shape and the velocity of the spot. With the spot leading edge propagation rate U_{le}, the trailing edge propagation rate U_{te} and the half spreading angle α; under the assumption of a triangular shape, σ can be expressed as:

$$\sigma = \left(\frac{1}{U_{te}} - \frac{1}{U_{le}}\right) U_\infty \tan(\alpha) \qquad (2.17)$$

Taking into account the concentrated-breakdown spot production rate function of Eqn. (2.15), one obtains:

$$\gamma(x) = \begin{cases} 0 & (x \leq x_t) \\ 1 - \exp\left[-\frac{n\sigma}{U_\infty}(x - x_t)^2\right] & (x > x_t) \end{cases} \qquad (2.18)$$

The previous expression highlights the need for onset of transition. Narasimha showed that, if the intermittency distribution $\gamma(x)$ was measured, x_t is best obtained by plotting the function

$$F_\gamma = \sqrt{-\ln(1 - \gamma)} \qquad (2.19)$$

against x and extrapolating to $F_\gamma = 0$ from the best fit of a straight line to the plot. This is desirable because small values of γ are hard to measure accurately.

With the introduction of the local Reynolds number $Re_x = U_\infty x/\nu$, Eqn. (2.18) can be rewritten as

$$\gamma(x) = 1 - \exp\left[-\hat{n}\sigma(Re_x - Re_{x_t})^2\right] \qquad (2.20)$$

where $\hat{n} = n\nu^2/U_\infty^3$ is a dimensionless spot production parameter.

2.2 Modelling transition

Separated state transition due to wake impact may be caused by Kelvin-Helmholtz instability in the free shear layer. The transition is then due to

the kinematic effect of the wake impact. Large scale roll-up vortices form which break-up into turbulence [77]. In separated state, transition may also be caused by diffusion of turbulence and pressure coupling, as in attached state. The transition is then due to the wake turbulence effect. This transition form is mainly of bypass type, however with some remnants of natural transition [46].

Turbulence models that are adapted to flows with low turbulence level, i.e. low Reynolds number turbulence models, are, to some extent, able to describe bypass forms of transition. An explanation of this ability has been given by Wilcox [91]. This is discussed in paragraph 2.2.1. The observation is that many eddy viscosity models and Reynolds stress models have such a transitional behaviour. However, this ability to mimic transition is, in essence, a consequence of mathematical properties of the system of turbulence equations. In the development and calibration of a turbulence model, the production of turbulence generated by a laminar velocity profile is not taken into account. So, the ability to mimic transition is not based on built-in physical properties.

An overview of the early developments on simulation of bypass transition with low Reynolds number turbulence models is given by Savill [64, 66]. Models, like the Launder-Sharma model, where the near-wall behaviour is described by the turbulence Reynolds number (Re_T) perform the best. However, no model gives a reliable result for various combinations of Reynolds number, free-stream turbulence level and pressure gradient. Moreover, results are sensitive to initial conditions, boundary conditions and numerical aspects like grid resolution and computational domain extension. The conclusions of Savill for the older turbulence models have been confirmed for newer turbulence models in the studies of Westin and Henkes [89], Craft et al. [17], Chen et al. [12], Lardeau et al. [37] and Hadzic and Hanjalic [24], for attached state bypass transition and for separated state bypass transition. Non-linear eddy viscosity models [12, 17, 37] and Reynolds stress models [89] generally produce better results than linear eddy viscosity models. In the cited references, only steady flows are considered. A first attempt to use a non-linear eddy viscosity model on wake-induced transition is due to Lardeau and Leschziner [34, 35]. They verify the quality of the model on the T106A test case. The predictions are qualitatively in good agreement with the experiments, but important quantitative discrepancies are observed. We will discuss their results during the analysis of the performance of our model on the same T106A test case in Section 6.2.

Reynolds stress models [89] often are extremely sensitive to boundary con-

ditions and numerical aspects. A recent study by Lardeau et al. [34] confirms these conclusions for non-linear eddy viscosity models. In order to improve the predictive capabilities of the models, Lardeau et al. introduce a laminar fluctuation energy equation as a pre-transition model and introduce intermittency dependence in the eddy viscosity. We discuss pre-transition models hereafter. In the model modification of Lardeau et al., the intermittency is described algebraically. This prevents the applicability of the model to general flows, as we discuss hereafter.

A very new class of transition models is based on the description of the laminar fluctuation energy in the pre-transition region of the boundary layer. The concept was introduced by Mayle and Schulz [47]. Recent examples of such models were formulated by Walters and Leylek [88] and Lardeau et al. [37]. A one-equation or two-equation system is used to describe the fluctuations prior to transition. Information from this system is used to start and let grow the turbulence. The principle is physically sound. The technique is however still much too new to allow a judgment on its qualities.

The most classic way to describe natural and bypass transition is based on the concept of intermittency, as introduced by Dhawan and Narasimha [55, 18]. The intermittency is the fraction of time the flow is turbulent during the transition phase. By letting grow the intermittency from zero to unity, start and evolution of transition can be imposed. Mostly, this is done by simply multiplying the eddy viscosity from a two-equation turbulence model with the intermittency factor. This simple approach neglects the interaction between turbulent and non-turbulent parts of the flow during transition. In order to capture this interaction, a conditional averaging technique leading to a set of turbulent and a set of non-turbulent equations for mass, momentum and energy is necessary, as used by Steelant and Dick [75, 76]. The conditional averaging is usually seen as too complex for engineering applications as the number of equations doubles. Therefore, the intermittency concept is typically used in combination with globally averaged Navier-Stokes equations and the loss of some physical information is accepted. Note that this loss of information is also present in the transition modelling based on the pure use of a low-Reynolds number turbulence model, as described earlier. The evolution of the intermittency is quite general for steady flows on flat plates [18, 55]. Furthermore, for these flows, the onset of transition and the growth rate of transition can be correlated quite easily. Well known correlations for onset of transition have been constructed by Abu-Ghannam and Shaw [3] and by Mayle [46]. Well known correlations for the growth rate are due to Mayle [46] and Solomon, Walker and Gostelow [73]. In the early applications of the

intermittency concept, the evolution of the intermittency was described algebraically with the "universal" distribution of Dhawan and Narasimha or a similar distribution and with start and end of transition determined by correlations. Examples of such algebraic techniques are due to Cho et al. [13] and Michelassi et al. [53], already applied to unsteady flows. A second technique is the Prescribed Unsteady Intermittency Method, introduced by Addison and Hodson [6] and Schulte and Hodson [70]. In this technique, intermittency patterns are described by a more complex set of algebraic equations. Physical phenomena like the spreading of turbulent spots and the calming of the boundary layer after wake passage, i.e. the relaxation to a laminar state, with enhanced resistance to separation, can be taken into account. A more general formulation of the intermittency is obtained by a dynamic intermittency convection-diffusion-source equation, as introduced in the frame of conditionally averaged Navier-Stokes equations by Dopazo [19]. This dynamic equation was further developed by Byggstøyl and Kollmann [11] and Cho and Chung [14]. The dynamic equation in the form of Cho and Chung was used by Savill et al. [64, 66, 86], but applied to globally averaged Navier-Stokes equations. It was combined with a Reynolds stress model and an eddy viscosity model and applied with success to steady transition in attached and separated state. The model requires empirical input for start of transition, but not for growth rate. The concept of dynamic intermittency combined with conditionally averaged Navier-Stokes equations was further developed by Steelant and Dick [75, 76]. They constructed an equation with empirical input for start of transition and growth rate of transition. Their dynamic equation for intermittency was adapted to globally averaged Navier-Stokes equations by Suzen, Huang at al. [80, 83, 82] and Pecnik et al. [58]. Although a general time dependent equation for intermittency is used in the previous cited works, all the applications are steady flows. The extension of the technique to unsteady flows is, however, more or less straightforward. First attempts to apply the technique to wake-induced transition were done by Suzen and Huang [81] for a low Reynolds number test case by Kaszeta and Simon and the T106A test case from Stieger and Hodson and by Pecnik et al. on the T106D test case[1] from Hilgenfeld, Stadmüller and Fottner [59]. The obtained results were encouraging but not particularly successful. In the test-cases used by Suzen and Huang, the separation bubble comes out much too large. There is qualitative agreement for velocity profiles, but there are large quantitative differences. Moreover, this study is far from complete. Comparison with experiments is only made for velocity profiles. There is no comparison for wall shear stress, boundary layer shape factor and momentum thickness, which are crucial parameters for final evaluation of the qualities of a transition model. For the

[1]The results of our model on the T106D test case are discussed in Section 6.3

test case used by Pecnik et al., the separation comes out too small. There is qualitative agreement with the experiment for shape factor, but quantitative differences are large. In this thesis, we present a model based on unsteady convection-diffusion-source equations for intermittency starting from the original equation of Steelant and Dick [76], but where we make also adaptations for globally averaged Navier-Stokes equations. The work has some similarity with the work of Suzen et al. and Pecnik et al.

2.2.1 (Nonlinear) eddy-viscosity models

Turbulence models that are adapted to flows with low turbulence level, i.e. low Reynolds number turbulence models, are, to some extent, able to describe transition. An explanation of this ability has been given by Wilcox [91]. A summary is given here. For the $k-\omega$ model, the incompressible 2D boundary layer form of the equations for k and ω is as follows.

$$U\frac{\delta k}{\delta x}+V\frac{\delta k}{\delta y} = \nu_t\left(\frac{\delta U}{\delta y}\right)^2-\beta^*\omega k+D_k \tag{2.21}$$

$$U\frac{\delta \omega}{\delta x}+V\frac{\delta \omega}{\delta y} = \alpha\frac{\omega}{k}\nu_t\left(\frac{\delta U}{\delta y}\right)^2-\beta\omega^2+D_\omega \tag{2.22}$$

$$\nu_t = \alpha^* k/\omega \tag{2.23}$$

For the standard high-Reynolds-number version of the $k-\omega$ model, α^* is equal to one. With the introduction of the *net production per unit dissipation* $\mathcal{P}_{k/\omega}$, the equations are as follows.

$$U\frac{\delta k}{\delta x}+V\frac{\delta k}{\delta y} = \mathcal{P}_k\beta^*\omega k+D_k \tag{2.24}$$

$$U\frac{\delta \omega}{\delta x}+V\frac{\delta \omega}{\delta y} = \mathcal{P}_\omega\beta\omega^2+D_\omega \tag{2.25}$$

$$\mathcal{P}_k = \frac{\alpha^*}{\beta^*}\left(\frac{\frac{\delta U}{\delta y}}{\omega}\right)^2-1 \tag{2.26}$$

$$\mathcal{P}_\omega = \frac{\alpha\alpha^*}{\beta}\left(\frac{\frac{\delta U}{\delta y}}{\omega}\right)^2-1 \tag{2.27}$$

Due to its definition, the sign of $\mathcal{P}_{k/\omega}$ determines whether k and ω are amplified or reduced in magnitude. After introduction of Blasius similarity variables the terms become

$$\mathcal{P}_k = \frac{\alpha^*}{\beta^*}Re_x\left(\frac{\frac{\delta \mathcal{U}}{\delta y}}{W}\right)^2-1 \tag{2.28}$$

$$\mathcal{P}_\omega = \frac{\alpha\alpha^*}{\beta} Re_x \left(\frac{\frac{\delta \mathcal{U}}{\delta y}}{W} \right)^2 - 1 \tag{2.29}$$

From the exact laminar solution of the Blasius boundary layer we obtain

$$\left(\frac{\frac{\delta \mathcal{U}}{\delta y}}{W} \right)_{\max} \approx \frac{1}{300} \tag{2.30}$$

Using this value, we conclude that signs change for the following Reynolds numbers.

$$(Re_x)_k = 9 \times 10^4 \frac{\beta^*}{\alpha^*} \tag{2.31}$$

$$(Re_x)_\omega = 9 \times 10^4 \frac{\beta}{\alpha\alpha^*} \tag{2.32}$$

For the closure coefficient without viscous modification, this results in $(Re_x)_k = 8100$ and $(Re_x)_\omega = 12150$. At $Re_x = 8100$ production of k exceeds its dissipation, and transition starts. At $Re_x = 12150$, values of ω also start to increase. Transition is complete when a balance between k and ω is achieved. For comparison, begin and end locations of transition on the T3A flat plate test case are at $Re_x = 120000$ and $Re_x = 300000$. This illustrates that for high-Reynolds-number turbulence models, transition starts too early, and transition length is too short. The transition location is also independent of the turbulence intensity (only Eqn. (2.30) is slightly dependent on the free-stream conditions).

The introduction of a viscous modification to the closure coefficients, in most cases, leads to an increase of $\frac{\beta^*}{\alpha^*}$ and $\frac{\beta}{\alpha\alpha^*}$. This will tend to delay transition. This delay in transition is not physical since these viscous modifications have been calibrated on fully turbulent flow conditions. Their behaviour on a laminar boundary layer is a priori unknown. The viscous modifications of Wilcox have been aimed for $(Re_x)_k = 90000$. The dependence of the transition location on the free-stream turbulence intensity is based on diffusion of turbulence quantities into the boundary layer. Their influence on the closure coefficients alters the critical Reynolds number of Eqns. (2.31) and (2.32). Experiments show that this is different from the physical transition mechanism, where transition is due to kinematic pressure fluctuations induced by the free-stream eddies penetrating into the boundary layer. These fluctuations amplify streamwise perturbations present already in the boundary layer. This is a much faster mechanism than diffusion.

In general, a two-equation eddy viscosity turbulence model can mimic start of transition if the net production term in the k equation, this is the sum of

the production term and the dissipation term, evolves from a negative value to a positive value in a laminar boundary layer, when starting from low levels of turbulence quantities. Similarly, a model can mimic the transitional region if the net production of the dissipation parameter (ω in Wilcox' analysis) also evolves from a negative value to a positive value and when the sign change is obtained after the sign change of the net production term in the k equation. The reasoning extends naturally to Reynolds stress models.

The predictive capability of turbulence model is inferior to the transition onset criteria. Lardeau et al. [37] combine the accuracy of the Mayle criterion for transition onset with the ability of the Craft, Launder and Suga [16] (CLS) nonlinear model to show low Reynolds effects. They include the laminar-kinetic-energy from Mayle and Schulz. Additionally, an algebraic intermittency equation is used in the evaluation of the kinetic energy k, a weighting of the laminar-kinetic-energy k_l and the turbulent kinetic energy from the CLS model k_t:

$$k = (1 - \gamma)k_l + \gamma k_t \tag{2.33}$$

To account for the different nature and result on turbulence production of the laminar fluctuations, the intermittency is a multiplier of the turbulent viscosity:

$$\nu_t = f_\mu c_\mu \frac{k(\gamma k_t)}{\varepsilon} \tag{2.34}$$

In doing so, the pretransitional fluctuations can be modeled upstream of the point where the skin friction starts to evolve to a turbulent level. The use of an algebraic intermittency equation prevents the applicability of the model to general flows.

2.2.2 Menter's approach

A class of transition models uses only *local* information, it means that no search or line-integration operations may occur. The motivation is that general-purpose CFD codes cannot carry out non-local operations. This is already the case for single processor calculations. Nowadays, most industrial CFD simulations are carried out on parallel computers using a domain decomposition.

More specific, the evaluation of the boundary layer momentum thickness, often used in correlations for prediction of transition location, is regarded as non-local information. Moreover, in multimode calculations, it will occur that the cells over which the momentum thickness integral is performed, are

physically allocated over two, ore more, different calculations nodes. Further, the momentum thickness loses its mathematical definition in case of 3D flows. By replacing all non-local (often 2D) information with local information, the model extends naturally to 3D flow.

Menter's transition detector

The basic idea of this approach [51] is to find a local estimation of Re_θ, thus omitting the non-local integral computation needed to obtain θ. This local detector is the vorticity Reynolds number Re_v. The vorticity Reynolds number can be composed using the strain magnitude or the vorticity rate magnitude.

$$Re_v = \frac{y^2 S}{\nu} \quad \text{or} \quad \frac{y^2 \Omega}{\nu} \tag{2.35}$$

The vorticity Reynolds number is analyzed here based on Pohlhausen laminar boundary layer profiles. In this approach, boundary layer profiles are assumed self-similar.

$$\frac{u}{U_\infty} = \left(2\eta - 2\eta^3 + \eta^4\right) + \lambda\left(2\eta - 6\eta^2 + 6\eta^3 - 2\eta^4\right) \tag{2.36}$$

with
$$\begin{cases} \eta &= \frac{y}{\delta} \\ \delta &= \text{boundary layer thickness} \\ \lambda &= \text{pressure gradient parameter} \end{cases}$$

$$S = \Omega = \frac{\partial u}{\partial y} = \frac{U_\infty}{\delta}\frac{\partial \frac{u}{U_\infty}}{\partial \eta}$$

$$\frac{Sy^2}{\nu} = \frac{U_\infty \delta}{\nu}\left[2 - 6\eta^2 + 4\eta^3 + \lambda\left(2 - 12\eta + 18\eta^2 - 8\eta^3\right)\right]\eta^2 \tag{2.37}$$

$\frac{Sy^2}{\nu}$ becomes zero at the wall ($\eta = 0$) and for $\eta = 1$. In the boundary layer, it has a unique maximal value $\left(\frac{Sy^2}{\nu}\right)_{\max}$ for

$$\eta = \frac{-1 + 8\lambda - \sqrt{21 - 36\lambda + 24\lambda^2}}{20\lambda - 10} \tag{2.38}$$

Inserting (2.38) into (2.37) gives

$$\left(\frac{Sy^2}{\nu}\right)_{\max} = \frac{U_\infty \delta}{\nu} f_1(\lambda) = Re_\theta \frac{\delta}{\theta} f_1(\lambda) \tag{2.39}$$

With θ the momentum thickness. Based on (2.36) we find

$$\frac{\delta}{\theta} = \frac{315}{37 - 4\lambda - 5\lambda^2} \tag{2.40}$$

This makes

$$\frac{\left(\frac{Sy^2}{\nu}\right)_{\max}}{Re_\theta} = f_1^*(\lambda) \tag{2.41}$$

Also

$$K = \frac{\nu}{U_\infty^2}\frac{dU_\infty}{dx} = Re_\theta^{-2}\frac{\theta^2}{\nu}\left(-\frac{1}{\rho U_\infty}\frac{dp}{dx}\right) \tag{2.42}$$

Near the wall

$$\frac{dp}{dx} = \left(\frac{\partial \tau}{\partial y}\right)_0 = \mu\left(\frac{\partial^2 U}{\partial y^2}\right)_0 = \mu\left(-\frac{U_\infty}{\delta^2}12\lambda\right) \tag{2.43}$$

This makes

$$K(Re_\theta)^2 = \left(\frac{\theta}{\delta}\right)^2 12\lambda = f_2(\lambda) \tag{2.44}$$

With numerical fit of (2.41) and (2.44)

$$\frac{\left(\frac{Sy^2}{\nu}\right)_{\max}}{Re_\theta} = 2.2 - \frac{20}{3}K(Re_\theta)^2 \tag{2.45}$$

Simulations have indicated that values of $K(Re_\theta)^2$ are negligible small. This assumption leads to

$$\left(\frac{Sy^2}{2.2\nu}\right)_{\max} = Re_\theta \tag{2.46}$$

The rotation Reynolds number is zero at the wall and at the edge of the boundary layer, with a single maximal value somewhat midway the boundary layer. This value equals $2.2Re_\theta$. Therefore we can use $Re_v/2.2$ as an indicator of Re_θ, and start the transition when $Re_v/2.2$ has reached the critical $Re_{\theta t}$ resulting from a transition criterion.

Drawbacks

This approach is very appealing, but thorough investigation reveals that at the time being, the model is not reliable enough to be used in combination with a transition onset criterion.

First, in the Pohlhausen representation, the shear and rotation are assumed zero outside the boundary layer. In real gasturbine environment this is not the case. This can, combined with the strong increasing values of y^2 far from the wall, activate non-physical intermittency. The detector needs to be limited to the boundary layer region.

Second, in the Pohlhausen representation, the curvature is not taken into account and accuracy decreases for extreme values of pressure gradient parameter. For cascades, the self-similarity condition is no longer fulfilled. Re_θ is not only locally determined but it results also from flow history. A correction has to be added for cascade test cases. Numerical simulations showed good agreement for flat plate cases, but for cascade test cases, $Re_v/2.2$ is 1.8 times smaller than Re_θ.

Third, because the parameter $Re_v/2.2$ has a profile in the boundary layer perpendicular to the wall, the start of transition and the γ profile are not constant perpendicular to the wall. This results in an important underevaluation of the intermittency γ close to the wall. This has to be compensated for.

Because of these drawbacks, in this work, values of Re_θ are calculated by intergration of θ throughout the boundary layer.

Current status

Menter and co workers recently presented a version of their local model [52], which they also implemented in the industrial code CFX. The model has been tuned for reference test cases. The dependence of Re_θ on acceleration parameter and others is included in the new transition onset criterion used. The model is intended to include basic transition influence in a broad range of industrial applications. No attempt has been made to include the physical mechanism of transition into the model.

2.2.3 Walters - Leylek model

This approach consists of a three-equation, linear, eddy-viscosity turbulence model. The model has equations for turbulent kinetic energy k_t, laminar kinetic energy k_l and far-field dissipation rate ϵ. The objective is to model the pre-transitional fluctuations with the k_l equation. Once a parameter including the kinetic energy is greater than some threshold level, the energy from the stream-wise fluctuations k_l is transferred to the turbulent fluctuations k_t.

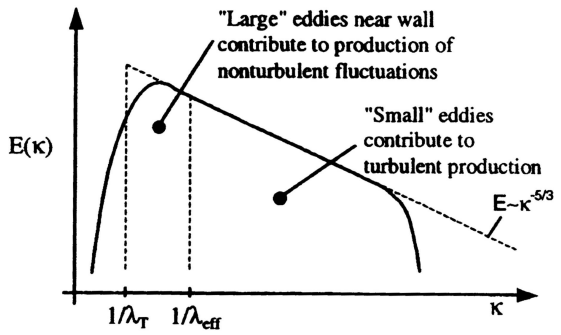

Figure 2.10: Illustration of wall-limiting concept leading to length scale selectivity concept for production of k_l

The dynamics of laminar kinetic energy production are not entirely understood at present. Nevertheless, among researchers a consensus is growing that two aspects are critical:

- selectivity of the boundary layer to certain free-stream eddy scales
- amplification of low-frequency disturbance in the boundary layer

The growth of k_l has been shown to correlate with low-frequency normal (v') fluctuations of the free-stream turbulence. These fluctuations are redirected in wall presence into stream-wise fluctuations. This process is accompanied by the creation of local pressure gradients in the boundary layer which tend to amplify the disturbances. It is in this way that laminar fluctuations differ from turbulence: the energy is almost entirely contained in the stream-wise direction and due to the absence of Reynolds stress, typical turbulence production does not occur. This mechanism is likely to occur only for eddies

with large length scales relative to the wall distance. The authors divide the energy spectrum in the near-wall region into wall-limited (large scales) and non-wall-limited (small scales) sections, see Figure 2.10. The cutoff eddy size used is the effective turbulent length scale λ_{eff}. Scales smaller than λ_{eff} interact with the mean flow as typical turbulence and larger scales contribute to the production mechanism for k_l. The dynamics of k_l have been found to be quite universal. The disturbances remain at relatively low frequency, and are amplified by large eddies whose fluctuations are redirected in the streamwise direction after penetrating in the boundary layer. So fluctuation energy grows linearly with Re_x, and dissipation is expected to be relatively low.

Assuming the Kolmogorov inertial range spectrum over all wave numbers greater than the turbulent length scale λ_t, the turbulent kinetic energy is separated into two components. The large-scale component is $k_{t,L}$, the small scale component is $k_{t,S}$.

$$k_t = k_{t,S} + k_{t,L} \tag{2.47}$$

$$k_{t,S} = k_t \left(\frac{\lambda_{eff}}{\lambda_t} \right)^{2/3} \tag{2.48}$$

$$k_{t,L} = k_t \left[1 - \left(\frac{\lambda_{eff}}{\lambda_t} \right)^{2/3} \right] \tag{2.49}$$

In this way, the turbulent kinetic energy k_t diffusing from the free stream into the boundary layer is split into two components. Only the large-scale part is used as a factor in the production term of the equation for laminar fluctuations k_l, accounting for the scale selectivity in the production mechanism for laminar fluctuation energy. Only the small-scale part is used as a factor in the production term of the equation for k_t, implemented as typical turbulent production with a damping function to impose viscous effects.

In both the equation for k_t and k_l, a term R appears, but with different sign. It is the rate of production of turbulent kinetic energy by laminar kinetic energy during the bypass transition process. Since it appears with opposite sign, it results in no net change of total fluctuation energy. It is also present in the equation for ε where it causes a decrease of turbulent length scale from the initial (approximately freestream) to a fully turbulent boundary layer scale. The term R contains a threshold function β_{BP} which determines start of bypass transition .

$$R = 0.21 \beta_{BP} \frac{k_l}{\tau_t} \tag{2.50}$$

$$\beta_{BP} = 1 - \exp\left(- \max\left[\left(\frac{\sqrt{k_t}\, d}{\nu} - 35 \right), 0 \right] / 8 \right) \tag{2.51}$$

It is assumed that laminar fluctuations break down whenever the turbulent kinetic energy k_t is greater than some threshold value, relative to the wall distance d and fluid kinematic viscosity. Transition is started if

$$k_t > \left(\frac{35\nu}{d}\right)^2. \tag{2.52}$$

The combination of the fulfilled threshold Eqn. (2.51) and the construction of the R term using k_l in Eqn. (2.50) expresses that transition initiates when the laminar stream-wise fluctuations (k_l) are transported a certain distance from the wall, where that distance is determined by the energy content of the free stream, and the kinematic viscosity.

A similar mechanism has been added for natural transition.

2.2.4 PUIM

The PUIM method was introduced by Addison and Hodson [6] and Schulte and Hodson [70] and provides an unsteady intermittency distribution which must be coupled to a flow solver. During the simulation, boundary layer parameters and flow variables at the edge of the boundary layer are read from the mean flow solver and fed into the PUIM procedure, which returns a distance-time intermittency field. For a steady state simulation, the distribution of intermittency is constant in time. The prescribed intermittency factor is then imposed on the turbulence model in the flow solver at streamwise wall stations defined within the mesh. The intermittency acts as a multiplier on the eddy viscosity, and is set to 1 in the freestream flow and 0.1 in the diffusive terms of the transport equations of the laminar regions. The method used for determination of the intermittency is a further extension of the Emmons theory. The breakdown location is determined using correlations.

Intermittency description

Emmons originally put forward the hypothesis of continuous breakdown in which there is uniform spot production downstream of the leading edge. More usually is to give spot production only downstream of x_t. Over the years, there has been much debate about which hypothesis is more appropriate. It is now believed (Schulte and Hodson [70], Ramesh and Hodson [61]) that the continuous breakdown hypothesis is more appropriate if the effects of calming

are taken into consideration. As the calmed regions following spots prevent the formation of new ones downstream of x_t, it ends up being similar to concentrated breakdown, except if the spot production rate is low.

The ability of the calming effect to suppress the formation of further spots means that the most probable location of spot formation lies near the start of transition. Downstream of this location fewer and fewer spots can form because the flow will be calmed or already turbulent for a part of the time. It often occurs that spot production is inhibited after the intermittency rises above 0.25.

In the case of steady flow, the calming effect is already taken into consideration when using the concentrated breakdown hypothesis. This is not the case in the context of wake-induced transition where the spot formation location (transition location) moves with time. In this way, sources may lie in the calmed zone of spots created at different locations with time. On the other hand, in a continuous breakdown hypothesis, the effect of calming must be included even for steady flows. This model of transition which includes the calming effect is proposed by Schulte and Hodson [70] and is used in their PUIM method.

In analogy to Eqn. (2.14), the probability that point $P(x, z, t)$ is turbulent or calmed, is expressed as

$$\gamma_{turb+calm}(P) = 1 - \exp\left[-\int_{V+W} g_{corr}(P_0)\, dV_0\right] \tag{2.53}$$

where V is the volume of dependency of the point. The volume W is the dependency cone of the calmed region, which means that it includes all points, which could have been the origin of a turbulent spot, whose calmed region would subsequently pass over the point $P(x, z, t)$. The corrected spot production rate g_{corr}, is the original spot production rate g, but corrected with the possibility that no spot can form because the flow is calmed or already turbulent $(1 - \gamma_{turb+calm})$.

$$g_{corr}(P_0) = (1 - \gamma_{turb+calm})\, g(P_0) \tag{2.54}$$

The intermittency is now expressed as:

$$\gamma(P) = 1 - \exp\left[-\int_{V} g_{corr}(P_0)\, dV_0\right] \tag{2.55}$$

Determining the onset of transition

The distribution of turbulence in the freestream is used to determine the location of transition onset. Once an inlet profile is available (eq. from measured data), a frozen turbulent kinetic energy model is used to relate local values to those at inlet, assuming the wake to convect with free-stream velocity. Decay and production of turbulence in the passage is thus not taken into account.

A number of steady correlations is used to determine the location of transition **onset in attached state**: Hourmouziadis, Mayle, Abu-Ghannam and Shaw, and e^N correlations.

Hourmouziadis [26] presents a correlation for start of transition only depending on the free-stream turbulence intensity by specifying the momentum thickness at start of transition by:

$$Re_{\theta t} = 460\, Tu^{-0.65} \tag{2.56}$$

A very similar correlation is suggested by Mayle:

$$Re_{\theta t} = 400\, Tu^{-0.625} \tag{2.57}$$

Taking also the pressure gradient into account, Abu-Ghannam and Shaw [3] describe critical momentum Reynolds number for start of transition as:

$$\begin{array}{lcll} Re_{\theta t} & = & 163 + \exp\left(f - \frac{f}{6.91} Tu\right) & \\ \text{with} & & & \\ f & = & 6.91 + 12.75\lambda_\theta + 63.64\lambda_\theta^2 & \text{for adverse pressure gradient} \\ f & = & 6.91 + 2.48\lambda_\theta - 12.28\lambda_\theta^2 & \text{for favourable pressure gradient} \\ \lambda_\theta & = & Re_\theta^2\, K & \end{array} \tag{2.58}$$

For the use of this correlation, Abu-Ghannam and Shaw propose that transition cannot begin when $Re_{\theta t} < 163$, which corresponds to the stability limit for zero pressure gradient flows. However, transition has been seen to begin below this value.

The e^N stability method for predicting transition onset is used with the correlation of Solomon et al. [74] which is adapted for use in turbomachinery. The critical N factor (N_{crit}) is made a function of the free-stream turbulence intensity level:

$$N_{crit} = -8.43 - 2.4 \ln(Tu) \tag{2.59}$$

For **separated** flow transition, correlations for length from separation to transition onset are used (l_{tr}). Separation is assumed if the skin friction coefficient is less than 0.0001 or the Thwaites pressure gradient parameter is less than -0.082.

Based on steady experiments, Garter proposes a correlation based on the momentum thickness at separation:

$$l_{tr} = 130\,\theta_{separation} \tag{2.60}$$

Mayle's correlation for a 'short bubble' may also be used:

$$l_{tr} = 300\,Re^{0.7}_{\theta_{separation}} \left(\frac{\theta_{separation}}{Re_{\theta_{separation}}} \right) \tag{2.61}$$

Determining the turbulent spot parameters

Once the location of the spot onset front is known, the spot production rate at each location along the front in the $S-T$ plane may be calculated. It is assumed that the production rate of the spots, which will occur randomly along the span, will be equal to those determined from the steady flow correlations.

Gostelow et al [22] have modified Narasimha's correlation for **concentrated breakdown** to include the effects of pressure gradient as well as free-stream turbulence intensity level to give a correlation for the dimensionless parameter N

$$N = \frac{n\sigma\theta_t^3}{\nu} = 0.86\times10^{-3}\exp(2.134\lambda_\theta \ln(Tu) - 59.23\lambda_\theta - 0.564\ln(Tu)) \tag{2.62}$$

The correlation from Mayle gives for zero pressure gradient flow:

$$M_{K=0} = \frac{n\sigma\nu^2}{U^3} = 1.5\times10^{-11}\,Tu^{7/4} \tag{2.63}$$

Corrections for pressure gradient are given in graphical form, but can be fitted by:

$$\begin{array}{rcll} \frac{n\sigma\nu^2}{U^3} & = & M_{K=0}\,10^{-0.8\sqrt{K}} & \text{for favourable pressure gradients} \\ & = & M_{K=0}\,10^{\alpha\sqrt{K}} & \text{for adverse pressure gradients} \end{array} \tag{2.64}$$

with α also given in graphical form.

For **separated** flow, the correlation for spot production rate is given by Mayle as:

$$\frac{n\sigma\nu^2}{U^3} = \frac{0.000228}{Re_{\theta_{separation}}^{1.4}} \tag{2.65}$$

In the case of **continuous breakdown**, the uncorrected spot formation rate used in Eqn. (2.54), is now expressed as a rate r_t *per unit area* per unit time. A simple relationship with the concentrated breakdown rate is used:

$$\frac{r_t\sigma\nu^3}{3U^4} = \left(\frac{n\sigma\nu^2}{U^3}\right)^{1.5} \tag{2.66}$$

r_t is evaluated at the start of transition and assumed constant thereafter. Due to the effect of calming, the corrected form of r_t is diminished downstream.

The individual spot-spreading angle α and propagation parameter σ have been measured on flat plates under steady conditions and for different pressure gradient parameters. Having done so, Gostelow [23] found the following relations:

$$\alpha = 4 + \frac{22.14}{0.79 + 2.72\exp(47.63\lambda_\theta)} \tag{2.67}$$

$$\sigma = 0.03 + \frac{0.37}{0.48 + 3\exp(52.9\lambda_\theta)} \tag{2.68}$$

It is seen that for adverse pressure gradient, the transition process is much faster.

2.2.5 Dynamic Intermittency

The first application of a dynamic intermittency equation to transitional boundary layer flow was done by Savill et al. [65]. They developed a one-equation intermittency model based on the work of Byggstøyl and Kollmann [11] and Cho and Chung [14]. The model performance is presented on flat plate test cases with sharp leading edge (T3A and T3A$^-$). For these cases, the start of transition is predicted by the underlying turbulence model. The length of the transition region is controlled by the intermittency equation. Recently, Vicedo et al [86] have applied the model to the steady case of separated flow transition of a flat plate with round leading edge (T3L). Here, the correlation by Mayle [46] is used to determine the distance between separation and transition. Upstream of the transition location, the source terms in the k and ε equation are disabled.

The transport equation for intermittency reads

$$\begin{aligned}\frac{D\gamma}{Dt} &= \frac{\partial}{\partial x_j}\left[\left(\nu + (1-\gamma)\frac{\nu_t}{\sigma_\gamma}\right)\frac{\partial \gamma}{\partial x_j}\right] + C_{\gamma 1}\,\gamma(1-\gamma)\frac{P_k}{k} \\ &\quad + C_{\gamma 2}\,\gamma\frac{k^2}{\varepsilon}\frac{\partial \gamma}{\partial x_i}\frac{\partial \gamma}{\partial x_i} - C_{\gamma 3}\,\gamma(1-\gamma)\frac{\varepsilon}{k} - C_{\gamma 4}\,\gamma(1-\gamma)\frac{\varepsilon}{k}\Gamma\end{aligned} \tag{2.69}$$

where the intermittency invariant, Γ, read

$$\Gamma \equiv \frac{k^{5/2}}{\varepsilon}\frac{u_i}{|\mathbf{u}|}\frac{\partial u_i}{\partial x_j}\frac{\partial \gamma}{\partial x_j} \tag{2.70}$$

The start of transition in the intermittency equation is an implicit result of disabling the source terms in the turbulence model. After transition, the levels of P_k/k start to increase.

Another one-equation model was proposed by Suzen and Huang [80]. The model is a combination of the Cho and Chung equation in the free stream, and the Steelant and Dick [76] equation in the boundary layer. A blending function enables the switch between the models. The onset of attached flow transition is determined by a new correlation including the effect of turbulence intensity and pressure gradient. The correlation resembles the Abu-Ghannam correlation in the adverse gradient region, and in addition, it reflects the fact that the flow becomes less likely to have transition when subject to favourable pressure gradients. In order to determine the onset of separated flow transition, the authors propose a correlation relating the distance between separation and transition onset to the momentum thickness Reynolds number at separation and the turbulence intensity.

Such one-equation models have been widely validated on steady test cases. Results on unsteady test cases are only presented for the Suzen and Huang model, and with little detail.

The approach presented in this thesis is a two-equation model for unsteady transition. The model is based on the dynamic equation for intermittency from Steelant and Dick [76]. Both steady and unsteady dynamics are considered during development of the model. Finally a validation of the model is performed on steady and unsteady test cases. The capability of the model to capture wake-induced transition is assessed.

Chapter 3

The model

3.1 Choice between a $k-\varepsilon$ and a $k-\omega$ turbulence model

The concept of a dynamic intermittency equation can be applied to any type of two-equations turbulence model. In this thesis, the application to two-equation turbulence models is presented, and the choice between a $k-\omega$ and a $k-\varepsilon$ model is made. To illustrate the difference in behaviour between a $k-\varepsilon$ model and a $k-\omega$ model, we use the low-Re Yang-Shih model [94] and the high-Re SST model [49]. Note, that in order to describe near wall behaviour, the low-Re extension of a $k-\varepsilon$ model is needed. This is not necessary for a $k-\omega$ model. Already in high-Re formulation, a $k-\omega$ model allows calculation in the near wall region. The low-Re modifications of a $k-\omega$ model improve the asymptotic behaviour near the wall and the transition behaviour of the model [91]. Since, here, we aim at modelling transition with a supplementary intermittency equation, we do not use the low-Re modifications in the $k-\omega$ model meant for transition. We use the SST version of the $k-\omega$ model due to its superior performance with respect to the standard $k-\omega$ model concerning free stream sensitivity and adverse pressure gradient behaviour. We take as test case the T3A flat plate flow from ERCOFTAC [1] with turbulence intensity $Tu = 3\%$ in the oncoming flow. This test case is extensively described in section 4.2. Figure 3.1 shows the variation of the friction coefficient for the T3A test case obtained with the $k-\varepsilon$ and $k-\omega$ models when they are used without modifications. The models predict start of transition far before the physical transition which occurs at approximately $Re_x = 1.2 \times 10^5$. This

deficiency of turbulence models without modification is well known [64]. In particular, we remark that the low Reynolds number $k-\varepsilon$ model shows pronounced transition behaviour with a very steep rise of the friction coefficient at the mathematical transition position. The high Reynolds SST model has a direct switch from laminar to turbulent state and has strong tendency to produce turbulent flow behaviour from the leading edge on. Further, this model shows a long relaxation phase before full turbulent behaviour is reached. We believe that this behaviour is due to the SST properties. A more classic $k-\omega$ model, like the Wilcox model shows a behaviour similar to that of the $k-\varepsilon$ model [91].

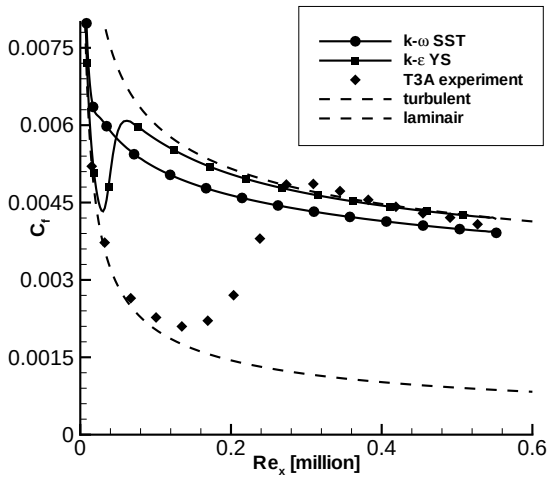

Figure 3.1: T3A; skin friction evolution for original k-ε and k-ω models.

Figure 3.2 shows the variation of the friction coefficient for the same test case when the production terms are suppressed up to $Re_x = 0.2 \times 10^6$ and when they are switched fully on at this location. The chosen switch location is well after the physical transition location. This result illustrates the explosive character of the transitional behaviour of turbulence models used without modification. The basic reason for the explosive character in the previous tests is that the turbulence models are forced to work on laminar velocity profiles. Turbulence models have been calibrated for turbulent flows only, and their behaviour on laminar flows has not been considered during design. Some consequences are illustrated in Figure 3.3 which shows profiles for the turbulent viscosity obtained by using the $k-\varepsilon$ model with the full production term on the T3A test case in laminar flow. In other words, the turbulent viscosity is

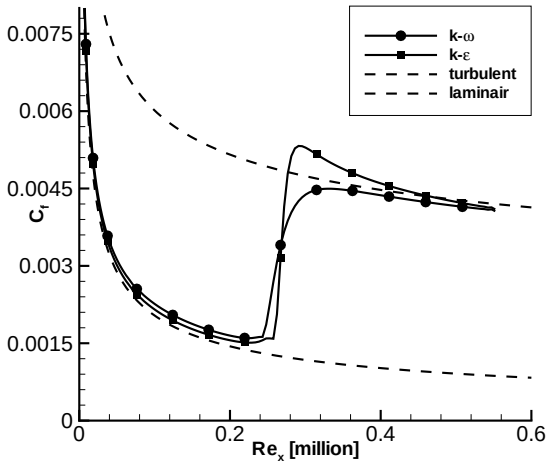

Figure 3.2: T3A skin friction evolution for k-ε and k-ω models with suppression of turbulence until $Re_x = 0.2 \times 10^6$.

set to zero in the Navier-Stokes equations. A comparison is made with the turbulent viscosity, obtained with the same model, in turbulent flows. The turbulent flow is obtained by allowing the turbulent viscosity in the Navier-Stokes equations. The corresponding C_f behaviour for the turbulent flows was already shown in Figure 3.1. From Figure 3.3a it is clear that the $k-\varepsilon$ model results in excessive values of the turbulent viscosity, when it is applied to a laminar flow. The corresponding values of the $k-\omega$ model, shown in Figure 3.3b, are much lower. The behaviour of the $k-\omega$ model is better than the behaviour of the $k-\varepsilon$ model since it does not rely on near-wall functions, which have been tuned on turbulent velocity fields. The consequence of the foregoing observations is that the behaviour of a turbulence model in the pre-transition zone is principally incorrect. In order to bring the behaviour closer to reality, turbulence has to be damped. A $k-\omega$ model and a $k-\varepsilon$ model react differently to damping of the production terms. Figures 3.3c and 3.3d show the turbulent viscosity obtained by multiplying the production terms with 0.2. The reduction obtained in turbulent viscosity is not substantial for the $k-\varepsilon$ model. For the $k-\omega$ model, turbulent viscosity becomes very small close to the wall.

In order to further illustrate the difference in behaviour of both models, Figure 3.4 shows the obtained skin friction coefficient when the production terms in the turbulence model have been multiplied with a factor 0.2 and

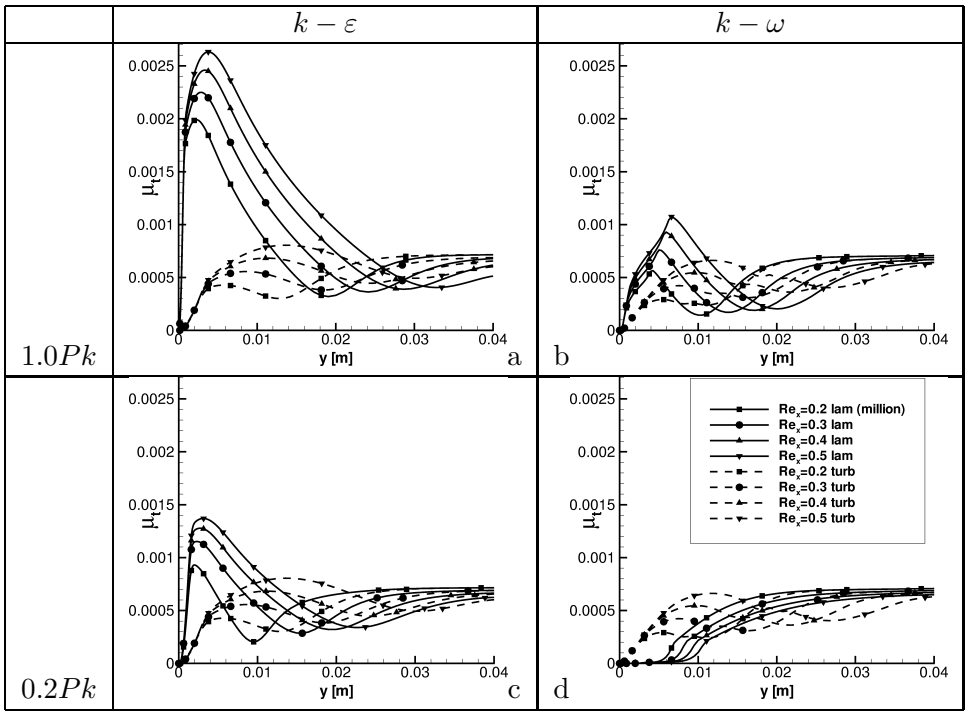

Figure 3.3: μ_t profiles at different Re_x locations on laminar and turbulent velocity profiles.

0.5. Also the turbulent viscosity used in the Navier-Stokes equations has been multiplied by this factor. The more explosive character of the $k-\varepsilon$ model is clear. This comparison shows that by steering the production term, a $k-\omega$ model can be easier controlled than a $k-\varepsilon$ model. For this reason we give here preference to the $k-\omega$ model.

3.2 The unsteady transition model

3.2.1 Modifications of the turbulence model

The turbulence model used is the SST $k-\omega$ turbulence model from Menter [49]. In order to suppress excessive production of turbulent kinetic energy near the stagnation point, a time scale bound T_{bound} has been applied according to Durbin [48]. Even with this time scale bound, false production was observed

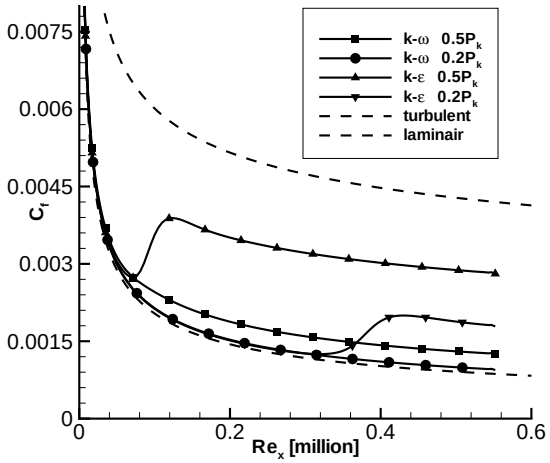

Figure 3.4: T3A skin friction evolution for k-ε and k-ω models with reduced terms.

in a small region at the leading edge of the profile. This non-physical turbulent kinetic energy is convected over the suction side such that a higher turbulence intensity is seen compared to experiments. To avoid this phenomenon, the production term P_k is disabled in a small region at the profile leading edge. The extension of this region is detailed in Table 3.1. The leading edge of the profile is located in the origin. In Figure 3.5, the region of disabled production term is shown for the T106D case.

	$\Delta x\,(mm)$	$\Delta y\,(mm)$	$c_{ax}\,(mm)$
MUR	$-2 \rightarrow 2$	$-4 \rightarrow 4$	37
VKI	$-10 \rightarrow 6$	$-10 \rightarrow 10$	197.5
T106A	$-10 \rightarrow 6$	$-8 \rightarrow 8$	170
T106D	$-4 \rightarrow 4$	$-4 \rightarrow 2$	≈ 86
N3-60	$-4 \rightarrow 20$	$-20 \rightarrow 2$	203.65

Table 3.1: Region of disabled production term P_k

The $k-\omega$ model, in high-Reynolds form, produces typically a very early and very rapid transition, which is completely unphysical [41, 42]. The objective of an intermittency based technique is to modify the transitional behaviour of a turbulence model and to control it by the description of the intermit-

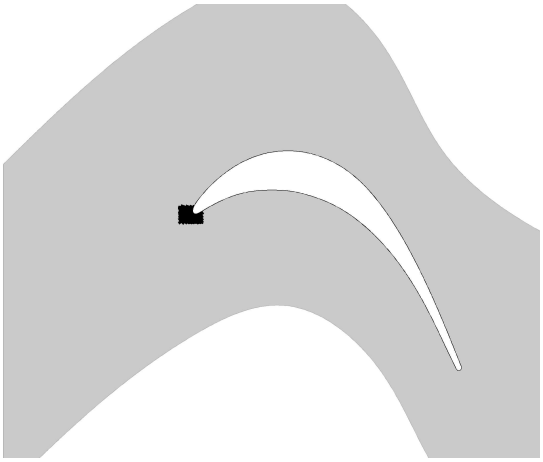

Figure 3.5: Region of disabled production term for T106D

tency. For this purpose, we use a turbulence weighting factor $\tau(\mathbf{x}, t)$. This factor is the fraction of time that the flow is turbulent on some location ($\mathbf{x}$) and at some time instance (t). So, this factor forms a generalization of the notion of intermittency, introduced in section 2.1.5. The factor is 1 in fully turbulent flow and 0 in fully laminar flow. For the Navier-Stokes part of the calculation, the turbulent viscosity from the turbulence model is multiplied by the turbulence weighting factor τ. For the turbulence model, the weighting factor is introduced in the k equation. The equation for ω is unaltered. In the production term of the k equation, a weighting of the turbulent viscosity and the molecular viscosity is applied. The destruction term is multiplied with τ.

$$\frac{\partial(\rho k)}{\partial t} + \frac{\partial(\rho U_i k)}{\partial x_i} = P_k - D_k + \frac{\partial}{\partial x_i}\left[\left(\mu + \frac{\mu_t}{\sigma_k}\right)\frac{\partial k}{\partial x_i}\right] \tag{3.1}$$

$$P_k = \left[\tau\ \mu_t + F_s(1-\tau)\ 0.08\ \mu\right] S^2 \tag{3.2}$$

$$D_k = \tau\ \rho\beta^* k\omega \tag{3.3}$$

Inside the boundary layer, τ and F_s are set to zero before transition so that the production and destruction terms are multiplied by zero. There is no production of turbulence, but diffusion remains from the free stream into the boundary layer. So, in the pre-transitional part of the boundary layer, μ_t is not zero. The description is probably not physically correct, but with τ set to zero, turbulent stresses in the Navier-Stokes equations are set to zero, so that correct description of pre-transitional fluctuations is not relevant. As a result, at start of transition, turbulent properties have a non-zero value. Small, but non-zero, starting values are essential to let grow turbulent properties sufficiently fast in the transition zone.

At the start of the transition zone, the starting function F_s is set to unity. With τ still almost zero, the production is strongly determined by the molecular viscosity. The original turbulence model has an extremely rapid, non-physical, transition mechanism. This is suppressed by the multiplication of μ_t with τ in Eqn. (3.2). Due to this multiplication, without the molecular term in (3.2), the build-up of turbulence properties becomes extremely slow. So, the molecular term is meant to let grow the turbulence properties at the very beginning of the transition zone. After this initial start, the turbulent part in the production term takes over. As already said, to realize this, a small, but non-zero, value of μ_t is necessary. The factor 0.08 was determined by optimization on the flat plate T3 test case series, see section 4.3. The value of the factor is not critical, neither is the starting value of μ_t.

Outside the boundary layer or after transition, i.e. where $\tau = 1$, the full production term is used.

The equation for ω is unaltered, but is given below for completeness.

$$\frac{\partial(\rho\omega)}{\partial t} + \frac{\partial(\rho U_i\omega)}{\partial x_i} = P_\omega - D_\omega + Cross + \frac{\partial}{\partial x_i}\left[\left(\mu + \frac{\mu_t}{\sigma_\omega}\right)\frac{\partial\omega}{\partial x_i}\right] \quad (3.4)$$

$$P_\omega = \rho\Gamma\frac{\omega}{k}\nu_t S^2 \quad (3.5)$$

$$D_\omega = \rho\beta\frac{\omega}{T_{bound}} \quad (3.6)$$

$$Cross = 2\rho(1-F_1)0.856\frac{1}{\omega}\frac{\partial k}{\partial x_j}\frac{\partial\omega}{\partial x_j} \quad (3.7)$$

$$T_{bound} = \min\left(\frac{1}{\omega}; \frac{0.6\sqrt{2}}{\sqrt{6}S}\right) \quad (3.8)$$

$$\mu_t = \rho k \min\left(T_{bound}; \frac{0.31}{S\ F_2}\right) \quad (3.9)$$

The function F_1 is the blending function beween $k-\omega$ and $k-\varepsilon$, the modification recently proposed by Menter et al. [51] is used. For the evaluation of the turbulent viscosity in Eqn. 3.9, the strainrate magnitude is used instead of the rotationrate magnitude, which is according to the recent model modification by Menter et al. [50].

3.2.2 The turbulence weighting factor τ

The turbulence weighting factor τ is the sum of the 'near-wall' intermittency factor γ and the 'free-stream' intermittency factor ζ. The intermittency factor

γ represents the fraction of time during which the near-wall flow is turbulent due to transition. This intermittency factor tends to zero in the free stream. The free-stream factor ζ expresses the intermittent behaviour of the turbulent eddies, coming from the free stream, impacting into the underlying pseudo-laminar boundary layer. Near the wall, the eddies are dampened and the free-stream factor goes to zero. The free-stream factor is unity in the free stream of a gas turbine engine, where the flow is always heavily turbulent. Both components of the turbulence weighting factor have been modelled by a convection-diffusion-source equation.

In earlier work where the turbulence weighting factor was used [76, 41], this factor was described by a single convection-diffusion-source equation. This worked well for steady flows. For unsteady flows, it is however necessary to make a distinction between the intermittency (ζ) at the edge of the turbulent free stream flow impacting on a laminar boundary layer and the intermittency (γ) in the transitional boundary layer resulting from the transition process, because their time scales are extremely different. The propagation of the free-stream turbulence into the laminar boundary layer is mainly a diffusion process and is therefore rather slow. The generation of turbulence in the transition zone of a boundary layer is caused by breakdown of vortical structures. This is a very rapid dynamic process.

3.2.3 Equation for free-stream factor ζ

Cho and Chung [14] investigated the intermittency at the edge between a turbulent jet and the surrounding laminar free stream. They developed a model which describes the intermittent submission of turbulent eddies coming from the jet disturbing the laminar free stream. Based on this work, Steelant and Dick [76] included the dissipation term E_ζ in their conditionally averaged transition model. Pecnik et al. [58] did a recalibration of two constants to fit the term into the globally averaged flow description. Based on this earlier work, we propose the following equation for the free-stream intermittency

$$\frac{\partial(\rho\zeta)}{\partial t} + \frac{\partial(\rho U_i\zeta)}{\partial x_i} = -E_\zeta + \frac{\partial}{\partial x_i}\left[\left(\mu + \frac{\mu_\zeta}{\sigma_\zeta}\right)\frac{\partial\zeta}{\partial x_i}\right] \tag{3.10}$$

$$E_\zeta = C_3\mu_\zeta\frac{U}{U_\infty^2}\frac{\partial U}{\partial n}\frac{\partial\zeta}{\partial n} \tag{3.11}$$

with $\sigma_\zeta = 1$, and n the direction to the nearest solid boundary. The factor C_3 was determined by Steelant and Dick as $C_3 = 2.5$, but Pecnik et al. argued that

for globally averaged NS, instead of conditionally averaged NS, the value has to be adapted to $C_3 = 15$. The term E_ζ guarantees a zero normal variation of the free-stream factor near the wall. In combination with the boundary condition $\zeta = 0$, this leads to a zero free-stream factor throughout the major part of the boundary layer. The diffusion coefficient μ_ζ has been determined by Steelant and Dick to create an inverse Klebanoff profile for the free-stream factor prior to transition. The coefficient is a function of ζ, where the Steelant and Dick term was a function of τ. Since this is a free-stream term, only the free-stream factor ζ should influence this diffusion coefficient. So we slightly modify the original diffusion coefficient into:

$$\mu_\zeta = \mu C_1 T u^{-0.69} \left[-ln(1-\zeta)\right]^{-\frac{1}{4}(1-\zeta)} \tag{3.12}$$

The factor C_1 has been redetermined by Pecnik et al. as $C_1 = 3.5$. We also use the exponent in (3.12), as modified by Pecnik et al. Further, the damping function f_{μ_τ} in the original expression has been left out. It is no longer necessary, since by replacing τ by ζ in (3.12), no singularity occurs at the wall.

The origin of the term f_{μ_τ} was to ensure that, in a one-equation intermittency model, close to a solid wall, the diffusion coefficient becomes zero. The expression for f_{μ_ζ} can be written as a function of y^+, and evaluated assuming the friction factor f of order 0.04; for laminar flow, $f = 64/Re$. Using the identity of the friction velocity u_τ that $\frac{u_\tau}{U_\infty} = \sqrt{f/8} = 0.071$, its value is plotted in Figure 3.6. We see that the term only had a mathematical importance, and no influence on the computation since its value was always equal to unity.

$$f_{\mu_\zeta} = 1 - \exp\left[-256\left(y^+ \frac{U_\infty}{u_\tau}\right)^2\right] \tag{3.13}$$

3.2.4 Equation for near-wall intermittency factor γ

The original steady equation

The original steady intermittency equation is a convection-diffusion equation with a source term, as developed by Steelant and Dick [76]. The Steelant and Dick equation has been constructed to reproduce the Narasimha [18] law in steady state. The basic form of the steady convection-diffusion equation has a convective term (lhs term), a source term (P_γ) and a diffusion term (D_γ):

$$\frac{\partial(\rho U_i \gamma)}{\partial x_i} = P_\gamma + D_\gamma \tag{3.14}$$

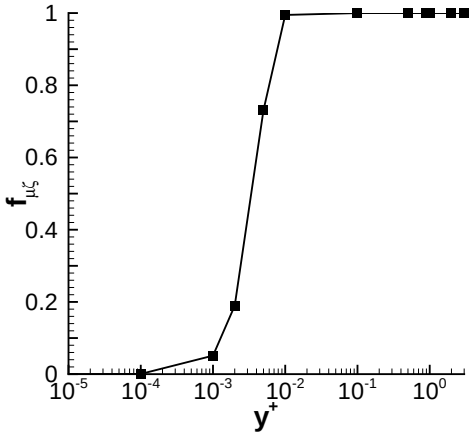

Figure 3.6: f_{μ_ζ} as function of y^+.

The production term P_γ of the intermittency equation is derived from the Narasimha law intending to see the steady intermittency equation reproduce the Narasimha equation throughout the boundary layer given a start of transition location. For zero pressure gradient, the intermittency γ can be described algebraically according to Dhawan and Narasimha [18] by

$$\begin{aligned} \gamma(x) &= 1 - \exp[-\hat{n}\sigma(Re_x - Re_{xtr})^2] \\ &= 1 - \exp[-A(x - x_{tr})^2], \qquad (3.15) \\ \text{with} \quad A &= \hat{n}\sigma \left(\frac{U_\infty}{\nu}\right)^2 \qquad (3.16) \end{aligned}$$

This gives

$$-\ln(1-\gamma) = A(x - x_{tr})^2 \qquad (3.17)$$

Derivation of (3.15), using (3.17), gives

$$\begin{aligned} \frac{d\gamma}{dx} &= 2A(x - x_{tr}) \exp[-A(x - x_{tr})^2] \\ &= \frac{2A}{\sqrt{A}} \sqrt{-\ln(1-\gamma)}(1-\gamma) \\ &= 2\beta(1-\gamma)\sqrt{-\ln(1-\gamma)} \qquad (3.18) \end{aligned}$$

Multiplying the previous equation with ρU produces the shape of the production term for intermittency equation P_γ.

$$P_\gamma = 2\beta(1-\gamma)\sqrt{-\ln(1-\gamma)}\rho U \qquad (3.19)$$

The parameter β is the spot growth parameter. It is described by empirical correlations due to Mayle [46]. The β-parameter depends on free-stream turbulence and on pressure gradient. The correlations are different for attached bypass transition and separated transition. The growth rate is significantly higher for separated transition. For attached bypass transition:

$$\beta = \frac{\sqrt{\hat{n}\sigma(Tu,K)}U_\infty}{\nu} \tag{3.20}$$

$$\hat{n}\sigma = 1.5\text{x}10^{-11}Tu^{7/4}f_K \tag{3.21}$$

$$\hat{n}\sigma_M = \hat{n}\sigma_{inc}\left[1+1.4M^{1.5}\right]^{-2} \tag{3.22}$$

$$f_K = \begin{cases} 10^{-3227K^{0.5985}} & \text{for} \quad K>0 \\ (474Tu^{-2.9})^{(1-exp(2.10^6K))} & \text{for} \quad K<0 \end{cases} \tag{3.23}$$

$$K = \frac{\nu}{U_\infty^2}\frac{dU_\infty}{dx} = \text{local acceleration parameter} \tag{3.24}$$

$$K_M = K_{inc}\left[1-M^2\right] \tag{3.25}$$

The Mach number correlation is obtained after a fit of data from Boyle and Simon [8]. For transition over a separation bubble:

$$\beta = \sqrt{\frac{0.0000228}{Re_{\theta separation}^{1.4}}}\frac{U_\infty \rho}{\mu} \tag{3.26}$$

The damping function f_τ introduced by Steelant and Dick, to account for distributed breakdown of turbulent spots is left out in the present model. The function was calibrated to be used in a steady model in combination with the destruction term E_ζ. Without recalibration, the term resulted in an important delay of transition. Furthermore, in all unsteady cases, transition is seen to take place in the deceleration part of the suction side, and is consequently of concentrated breakdown type[1].

$$\begin{aligned} f_\tau = &\quad 1-\exp[-1.735\tan(5.45\tau-0.95375)-2.2] \quad \text{Steelant and Dick} \\ f_\tau = &\quad 1 \quad \text{Current model} \end{aligned} \tag{3.27}$$

We add a general diffusion term to ensure a gradual variation toward the free-stream condition. Since the spots grow in a laminar surrounding, their diffusion is basically molecular. Therefore we use the molecular viscosity coefficient. The diffusion term is of smaller magnitude than the production term. In this way, the stream-wise variation of intermittency is not influenced by the diffusion of intermittency.

$$D_\gamma = \frac{\partial}{\partial x_i}\left[\mu\frac{\partial\gamma}{\partial x_i}\right] \tag{3.28}$$

[1] Argumentation is given in Section 2.2.4

Considering the above, the steady equation for intermittency factor reads:

$$\frac{\delta(\rho U_i \gamma)}{\delta x_i} = f_\tau P_\gamma + D_\gamma \tag{3.29}$$

Adding the unsteady term, the equation becomes:

$$\frac{d\gamma}{dt} = \frac{\partial(\rho\gamma)}{\partial t} + \frac{\partial(\rho U_i \gamma)}{\partial x_i} = f_\tau P_\gamma + D_\gamma \tag{3.30}$$

If we examine the unsteady equation in a unsteady case, the production term appears to be a very slow term. At start of unsteady transition, the time scale for intermittency growth starting from a small value is very large. We examine the build-up of intermittency starting from a low value of 0.02:

$$\left|\frac{d\gamma}{dt}\right|_{0.02} = |f_\tau|_{0.02}\,|P_\gamma|_{0.02} + |D_\gamma|_{0.02} \tag{3.31}$$

$$\text{and} \quad |f_\tau|_{0.02} = 0.218 \tag{3.32}$$

$$|P_\gamma|_{0.02} = 2\beta\,|\gamma|_{0.02}\,\rho U \tag{3.33}$$

$$|D_\gamma|_{0.02} = 0 \tag{3.34}$$

$$= \text{Cst}\,|f_\tau|_{0.02}\,U\,|\gamma|_{0.02} \tag{3.35}$$

Integration shows that γ grows exponentially with time, with a timescale T.

$$|\gamma|_{0.02} = \exp(t/T) \tag{3.36}$$

$$\text{with} \quad T = \left(\frac{1}{\text{Cst}\,|f_\tau|_{0.02}\,U}\right) \tag{3.37}$$

The function for distributed breakdown is seen to slow down the time response of the intermittency production. This is in no way physical. Also near the wall, the velocity U is small, and leads to a huge timescale.

The new unsteady equation

The unsteady near-wall intermitteny equation is given below. The production term is used in both steady and unsteady cases.

$$\frac{\partial(\rho\gamma)}{\partial t} + \frac{\partial(\rho U_i \gamma)}{\partial x_i} = P_\gamma + \frac{\partial}{\partial x_i}\left[\mu\,\frac{\partial \gamma}{\partial x_i}\right] \tag{3.38}$$

$$P_\gamma = 2\beta(1-\gamma)\sqrt{-\ln(1-\gamma)}\rho\frac{[U_\infty F_s + (U-U_\infty)(2-F_s)]}{\max[F_s, 1.0]} \tag{3.39}$$

Additionally, production of γ is disabled when $\tau = 1$ to ensure that outside the boundary layer the production of intermittency γ is brought to zero.

The velocity scale factor between square brackets has been modified with respect to the original one. The original factor is recovered for the starting function $F_s = 1$. The velocity scale is then the local velocity. With the local velocity scale ($F_s = 1$), steady bypass transition in attached decelerated flow is adequately described [41, 42]. As modelling approach, we assume that this is also the case for *wake turbulence induced* bypass *transition* in attached decelerating flows. Indeed, there is much experimental evidence that wake turbulence induced bypass transition happens in a *quasi-steady* way. We refer to the work of Addison and Hodson [4, 5], Orth [57], Liu, Rodi and co-workers [39, 13], Schobeiri et al. [68]. In this experimental work, it is shown that bypass transition caused by wake impingement begins at the same location, independent of the wake passing frequency. This experimental observation has led to a number of algebraic intermittency models for wake-induced bypass transition where the correlations of Mayle [46] or Abu-Ghannam and Shaw [3] for start and length of steady bypass transition have been used with success. We refer to Addison and Hodson [6], Liu and Rodi [13], Michelassi et al. [53], Jiang and Simon [29].

Similarly, wake turbulence induced transition over a separation bubble is seen to happen in a quasi-steady way, as demonstrated by Schobeiri et al. [67]. Here too, as modeling approach, we use the local velocity scale ($F_s = 1$).

For *kinematic wake impact* on a separation bubble, the velocity scale determining the transition has to be modified in (3.39). Inside a separation bubble, the velocity is very low. This has as consequence that the production term with local velocity is near to zero and that almost all generation of intermittency has to come from the diffusion term in (3.38). This diffusion process does not correspond to reality. Kinematic wake impact on a separation bubble causes an almost immediate breakdown of the free shear layer due to Kelvin-Helmholtz instability, as experimentally evidenced by Stieger and Hodson [77, 79]. Roll-up vortices form. The Kelvin-Helmholtz instability has also been observed in DNS and LES simulations of separation transition on turbine cascades. We refer to Wu and Durbin [92], Michelassi et al. [54], Raverdy et al. [62]. Even without incoming wake, the breakdown of the free shear layer is caused by unsteadiness triggered by the trailing edge vortex shedding. The physical mechanism of instability, i.e. Kelvin-Helmholtz instability, is not essentially different from the mechanism of quasi-steady transition over a separation bubble. There is however a difference in size. For quasi-steady

transition over a separation bubble, the first, laminar part, of the separation bubble is not affected by K-H vortices, and the vortices that finally form are of small scale. Contrary, kinematic wake impact on a separation bubble affects the entire separation bubble at once. There is no delay length between the separation point and the start of shear layer instability. The very rapid breakdown in kinematic wake impact transition is modelled here by putting the velocity scale to a high value in (3.39). This is achieved for $F_s = 2$. The velocity scale then becomes U_∞. As can be verified in the simulation results shown later[2], with $F_s = 2$, the intermittency γ is forced almost immediately to unity. So within the modelling frame of the intermittency equation (3.38), sudden transition of a separation bubble is expressed in this way. No fitting has been done to describe the correct temporal behaviour of the rapid appearance of the intermittency, it simply has to be large enough. Of course with γ forced rapid to unity, turbulence properties still have to build up with the turbulence equations.

After wake passage, when the physical reasons for transition disappear, F_s is set to zero. The production term then becomes a destruction term due to the negative velocity scale $2(U - U_\infty)$, which is mainly active near the wall. Once the trigger to transition is switched off, the near-wall intermittency is damped by wall presence. The intermittency still present in the bulk of the boundary layer is mainly convected with the flow. So, the intermittency equation describes this physical process.

From the previous discussion, it is clear that during unsteady build-up and break-off of intermittency, large differences may occur between the intermittency at the wall and the intermittency in the bulk of the boundary layer. Therefore boundary layer averaged values of the weighting factor are also shown in the results, computed as:

$$\tau_{avg} = \frac{1}{\delta} \int_0^\delta \tau \, dx \tag{3.40}$$

For bypass and quasi-steady separation transition, the timescale for buildup of intermittency is dependent on the local velocity, see Eqn. (3.37). A sudden start of transition due to an upstream shift of the transition location leads to a faster increase of τ_{avg} compared to γ at the wall. At the wall, the velocity is zero, so buildup is zero, an increase in intermittency is the result of diffusion toward the wall[3]. For unsteady separation transition, using the free-stream velocity scale, the time scale for build-up of intermittency is constant through-

[2]See plot of starting function F_s in Figure 6.11 and plot of intermittency in Figure 6.13

[3]This can be observed in the simulation in Figure 6.13 for $S = 0.64$ and $T = 1.1$

out the boundary layer. Since the convecting velocity is lower near the wall, this implicates that the lengthscale for build-up is shorter near the wall.

3.2.5 Starting and stopping of transition

For start of bypass transition in attached state, the criterion of Mayle [46] is used. The starting function F_s is set equal to 1 in the boundary layer, downstream of start of transition. To do this, a stream-wise coordinate is created by solving the following equation with zero gradient boundary condition at walls:

$$\frac{\partial(U_i s)}{\partial x_i} = U \tag{3.41}$$

This coordinate is calculated for steady flow conditions. Stations are defined by lines perpendicular to the streamwise coordinate lines. On the stations, the momentum thickness is calculated. The edge of the boundary layer is defined by the location where the rotation magnitude is 1% of the maximum value. Free-stream turbulence intensity is taken on this position. The level of 1% can be subject to change. The maximum rotation is often obtained in the first cell to the wall, and depends on the global Reynolds number, and the grid refinement. If necessary, the level has to be reduced until convergence of H_{12}, or θ is obtained.

For start of transition in separated state, both quasi-steady and unsteady criteria are used. The start of quasi-steady separation transition is determined from the criterion of Mayle [46]. The starting function F_s is set equal to 1 downstream of this position. For roll-up separation transition, the wake impact is detected through the free-stream turbulence level. We take here 2.12% as detection criterion, the reasoning of this is explained below. The starting function F_s is set equal to 2 downstream of the impact position. F_s stays at 2 as long as the criteria of 2.12% free-stream turbulence level on separation are satisfied. The level of 2.12% is based on work of Zhang et al. [97]. They argue that bypass transition precedes, and thus prevents, roll-up if Re_θ at separation is higher than about 250. Using the Mayle correlation, this corresponds to the turbulence level of 2.12%. Consequently, roll-up is possible if the separation Re_θ is lower than 250 or alternatively the turbulence intensity at separation higher than 2.12%.

The criterion for kinematic wake-induced separation transition is used together with the criterion for wake-turbulence induced separation transition

and with the criterion for attached bypass transition. Whichever value of F_s is the largest, is imposed.

Chapter 4

Flat plate test cases

4.1 Introduction

The test cases of this section consist of steady flows over a flat plate with sharp leading edge. A broad range of Reynolds numbers and free stream turbulence intensities are covered. The influence of pressure gradient is introduced by altering the channel section. Flat plates have a certain popularity among experimenters. The dimensions can be quite large, and the surface is flat. This makes them easy to instrument. Also for numerical simulations there are advantages. The grid generation is easy and the mesh size can be kept low, which allows a quick evaluation of the performance of different models.

4.2 Test-cases

For development of the steady model and testing, bypass transitional flows on adiabatic flat plates with sharp leading edges proposed by Kuan and Wang (KW case) [33] and by ERCOFTAC (T3 cases) [1] have been used. Three zero pressure gradient test cases were considered (KW, T3A and T3B), and three with pressure distribution (T3C1 ,T3C2 and T3C5). In the experiments, the pressure distribution is imposed by a variable surface opposite to the flat plate. The oncoming flow is accelerated in the first part up to the point of minimal channel section. Downstream, the channel height increases and the flow is decelerated. The specifications of the different test cases are given in Table

4.1 where U_i stands for the oncoming velocity and Tu_{le} for the turbulence intensity at the leading edge. The experimental decay of free stream turbulence has been reproduced by variation of the inlet turbulence length scale. Values for k and ω at the leading edge are listed in Table 4.1. When extrapolating the turbulence intensity to the leading edge value, differences with the test case specifications are observed. The values obtained via extrapolation, listed under Tu_{le} Mayle, were used to determine the values of Re_θ at transition onset.

Case	$U_i(m/s)$	$Tu_{le}(\%)$	Tu_{le} Mayle (%)	$k_{le}(m^2/s^2)$	$\omega_{le}(s^{-1})$	$(\mu_t/\mu)_{le}$
KW	13.8	1.1	1.1	0.0345	166	14.23
T3A	5.4	3	2.8	0.042	232	12.4
T3B	9.4	6.14	6.14	0.488	315	106
T3C1	6.12	7.78	6.0	0.324	430	51.58
T3C2	5.3	3	2.3	0.0313	254	8.436
T3C5	9.26	3	2.3	0.103	500	14.1

Table 4.1: Description of U_i and Tu_{le} for flat plate test cases. Further, numerical estimates are given for Tu_{le} Mayle, k_{le}, ω_{le} and $(\mu_t/\mu)_{le}$

The numerical grids for flat plates contain about 200 nodes in streamwise direction and about 100 in crosstream direction. The first grid point is located at $0.025\,mm$ from the wall, which ensures $y^+ < 1$ for all test cases. A stretching factor has been applied perpendicular to the wall. In stream-wise direction, also a stretching factor has been applied near the leading edge. The inlet is $200\,mm$ upstream of the leading edge. For the pressure gradient test cases, a curved wall (with slip allowed) has been placed opposite the flat plate, to get the appropriate velocity distribution. This is an iterative process since the boundary layer growth is dependent on the transition, and influences the pressure distribution in the channel flow. The computational domain for various test cases is shown in Figure 4.1. For the zero pressure gradient cases, the upper boundary is a constant pressure outlet. This pressure outlet has a slight angle to prevent flow entering the domain through this boundary condition. The upper boundary of the variable pressure distribution cases is an inviscid wall.

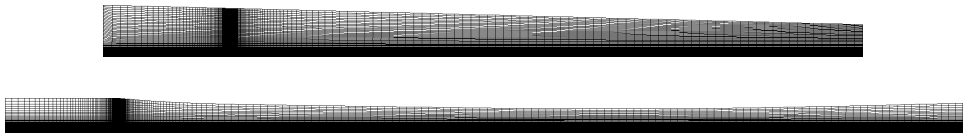

Figure 4.1: Computational domain and grids used for the simulation of T3A (upper) and T3C2 (lower).

4.3 Numerical results on KW and T3 test cases.

The Mayle criterion specifies that the free-stream turbulence intensity has to be evaluated at the leading edge when used in the correlation for onset prediction of Eqn. (4.1).

$$Re_{\theta t} = 420 Tu_{le}^{-0.69} \tag{4.1}$$

Figure 4.2 shows the skin friction evolution for the flat plate test cases. The correspondence with the experiments generally is very good except for the T3C2 case. The cases KW, T3A and T3B differ only in leading edge level of free-stream turbulence intensity. For increasing Tu_{le} (T3B > T3A > KW), transition starts earlier. Made dimensionless, this means at lower Re_x values. This is clearly reproduced by the model. The KW case has a turbulence intensity which is merely higher than the limit necessary for bypass transition to occur[1]. Still, the transition is well reproduced by the model. The T3C cases all have an acceleration phase followed by a deceleration phase. For the T3C1 and T3C5 cases, transition occurs during the acceleration. The T3C1 case has a Tu_{le} comparable to T3B. Transition starts consequently at similar levels of critical Re_θ ($Re_{\theta t}$). Due to the acceleration in the T3C1 case, the boundary layer growth is slower, and $Re_{\theta t}$ is achieved at a larger value of Re_x than in the T3B case. The acceleration also reduces the growth rate of the spots, so the length of transition becomes larger. For the T3C5 case, the Tu_{le} is lower which results in a more downstream start of transition.

To explain the difference between T3C5 and T3C2, we analyze the influence of Reynolds number, Re_l based on oncoming velocity and plate length, on the local acceleration parameter in a fixed point in the converging-diverging channel above the flat plate. The Reynolds number is changed by varying the oncoming velocity.

$$K = \frac{\nu}{U_\infty^2}\frac{dU_\infty}{ds} \sim \frac{1}{Re_l}\frac{l}{U_\infty}\frac{dU_\infty}{ds} \tag{4.2}$$

Since the geometry remains unchanged, $\frac{l}{U_\infty}\frac{dU_\infty}{ds}$ remains constant in a fixed

[1] as described in section 2.1.2

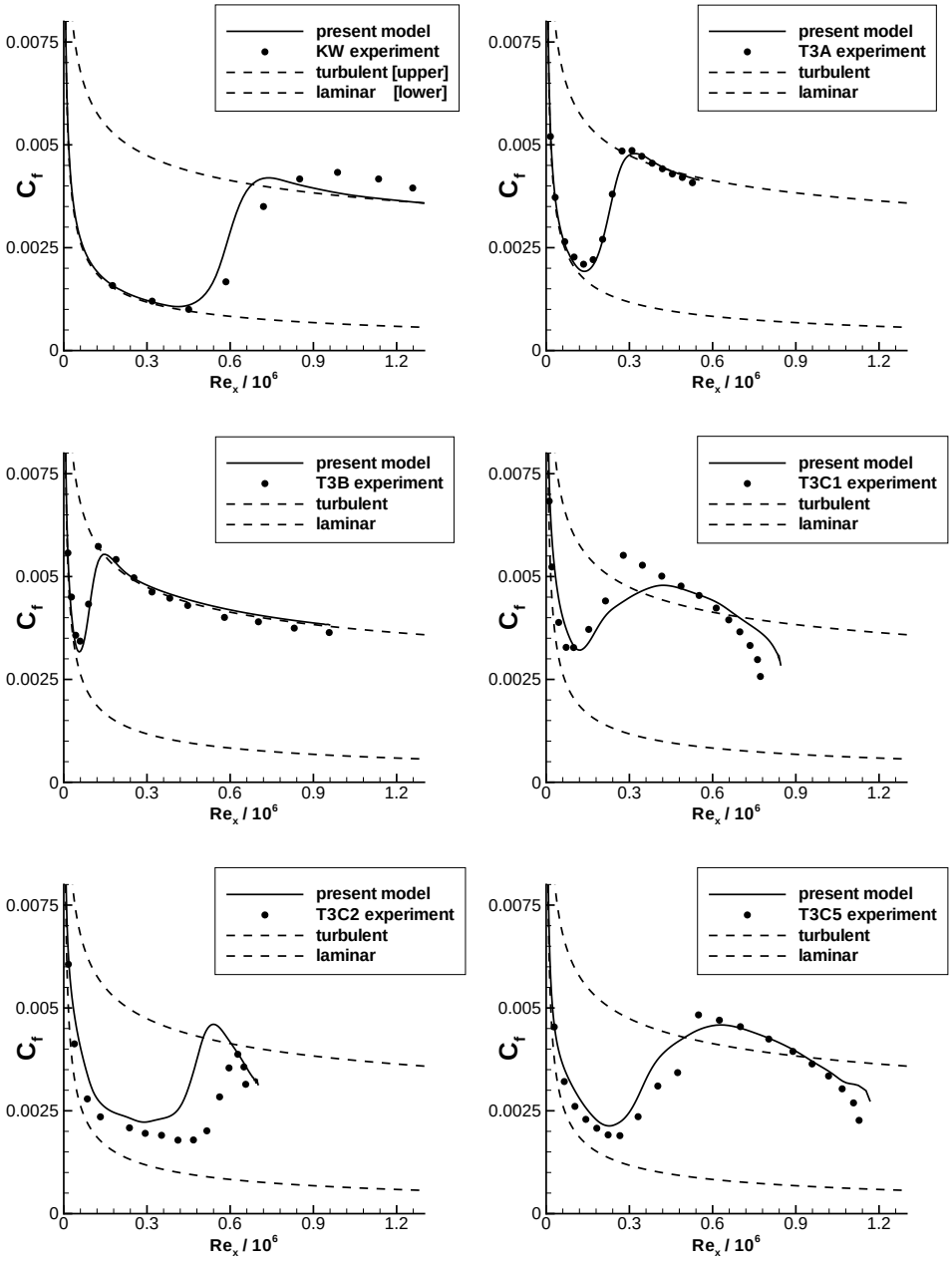

Figure 4.2: Skin friction evolution for the flat plate test cases.

point when varying the Reynolds number. So the acceleration parameter is stronger for reduced Reynolds number, in this case the oncoming velocity. The T3C2 has a similar level of Tu_{le} as T3C5, but the oncoming velocity is lower. The critical Re_θ value is similar. Due to the lower velocity, values of the acceleration parameter K are more extreme in the case of T3C2, compared to T3C5. So in the accelerating part, the critical Re_θ value for T3C2 is achieved at a level of Re_x somewhat higher than for T3C5. But still, in terms of Re_x, transition is detected earlier than in the experiment. The higher acceleration also reduces the spot growth. This explains the slower growth of the intermittency after transition in the case of T3C2. Due to the lower Reynolds number, the deceleration in T3C2 is also more extreme, compared to T3C5, so a rapid completion of transition is seen during deceleration. For T3C2 case, the levels of momentum thickness θ have a plateau value for values of Re_x from 0.28 $\times 10^6$ to 0.4 $\times 10^6$. In this region, small changes in $Re_{\theta t}$ correspond to a large variation in Re_{xt}. So, even for T3C2 case, the Mayle criterion prediction of $Re_{\theta t}$ is reasonably good.

The T3C2 is very challenging because the free-stream turbulence intensity and the Reynolds number are low, so transition is expected to occur far downstream. In the accelerated first part of the boundary layer Re_θ numbers remain low, and transition does not occur. After start of deceleration the boundary layer momentum thickness rapidly starts to increase, and the Mayle critical Reynolds number (based on leading edge turbulence intensity) is achieved. Although at that location, the free-stream turbulence intensity has decayed substantially, see Figure 4.3, and would result in a more downstream transition location if used as a local value in Eqn. (4.1). For this case it is not clear which turbulence intensity induces transition: the higher values affecting the accelerated boundary layer or the lower values affecting the decelerating part. It is obvious that the Mayle criterion based on the leading edge Tu level is here at the edge of its applicability.

In Figure 4.4, the evolution of the turbulence weighting factor τ is shown on different perpendicular profiles to the wall through the transition. From $Re_x = 0.01 \times 10^6$ to $Re_x = 0.1 \times 10^6$ we see the boundary layer growing. At $Re_x = 0.15 \times 10^6$ transition has started with values of $\tau = 0.1$ ($\gamma = 0.1$, $\zeta = 0$) in the boundary layer, and a transition to $\tau = 1$ ($\gamma = 0$, $\zeta = 1$) in the free stream. Similar to experimental observation in steady cases, the intermittency has a plateau value in the boundary layer throughout the transition.

Figure 4.5 shows the evolution of experimental skin friction of the T3A test case; also shown is the (rescaled) computed intermittency factor at the

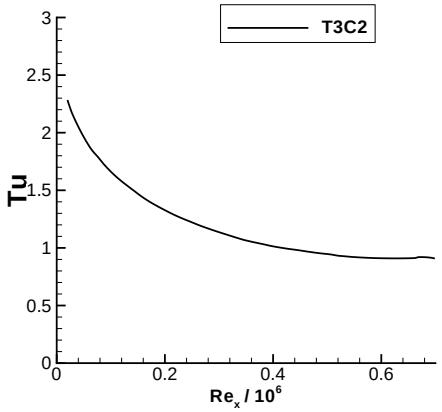

Figure 4.3: Evolution of free-stream turbulence intensity for the T3C2 test case.

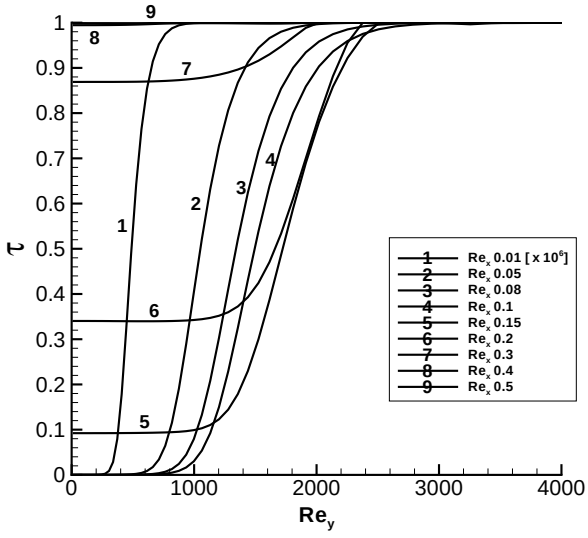

Figure 4.4: Turbulence weighting factor at different stations perpendicular to the wall for the T3A test case.

wall $\gamma/100$. The dash-dot line shows the (rescaled) intermittency obtained from weighting of the simulated skin friction between the correlations of laminar and turbulent skin friction evolution ('γ from C_f' from hereon). There is no acceleration in the T3A case, so before transition, the skin friction should be equal to the laminar correlation, and 'γ from C_f' = 0. After transition, the turbulent skin friction should be reproduced, 'γ from C_f' = 1. Skin friction halfway between the two curves gives 'γ from C_f' = 0.5. We see a good agreement between the curves of γ and 'γ from C_f'. This illustrates that the intermittency has the desired result on the Navier-Stokes part of the computation. This is not trivial, and is the result of the production term for turbulence P_k in Eqn. 3.2. In the N-S part, the effective viscosity is applied:

$$\mu_{eff} = \mu + \tau\,\mu_t \tag{4.3}$$

The good agreement between C_f and γ or τ, can only be obtained with physically correct values of μ_t in Eqn. (4.3), this is the value of the turbulent viscosity in the turbulent spot. In Figure 4.5 we see an initial good response of the skin friction to the increase in intermittency. This is the result of the term $\tau\,0.08\mu$ in Eqn. (3.2), since at start of transition, the turbulence model still has to undergo transition, with values of μ_t still low. Halfway transition, we see that the simulated skin friction goes up faster than the intermittency. This in an inherent result of the explosive character of the SST turbulence model on a laminar velocity profile, explained in section 3.1. There is even some overshoot. The levels of μ_t go up fast, and their influence is seen. After transition, the original version of the turbulence model is applied, and the overshoot is quickly recovered.

4.4 Conclusion

In all cases, except for T3C2, transition is located in the zero pressure gradient (ZPG) or favourable pressure gradient part. For the T3C2, transition is detected in the simulation in the ZPG part, but experimentally it is located at start of the deceleration. In accelerated and ZPG flow, values of Re_θ grow slowly with increasing Re_x. In decelerated flow (adverse pressure gradient), the values of Re_θ increase quickly with Re_x. The quantification of the transition location in terms of Re_{xt} by using a criterion for $Re_{\theta t}$ will result in substantial less error in the adverse pressure gradient part. In the unsteady cases that are relevant for LP turbines[2], transition is seen to take place in the

[2]T106A (Low $Re_{2c} = 160000$, High $Tu = 4\%$) described in section 6.2.7, T106D described in section 6.3.3, N3-60 (High $Re_{2c} = 600000$, High $Tu = 4\%$) described in section 6.4.4

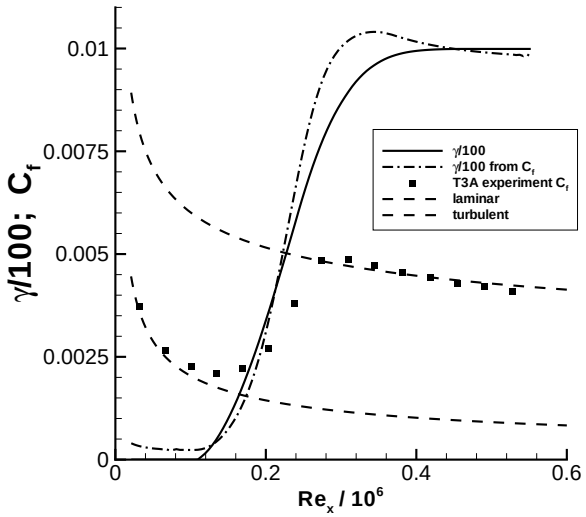

Figure 4.5: Evolution of 'intermittency' for the T3A test cases.

decelerated part. So possible errors are limited. In this viewpoint, the flat plate test cases have limited importance for wake-induced transition in LP turbines.

Although the test have limited relevance in an unsteady turbomachinery environment, the agreement with the experiments is judged sufficiently good. The model has to be able to reproduce steady test cases, since in wake induced transition also quasi steady bypass transition is observed. But, in an unsteady context, reproducing the correct response to the impacting wakes dominates the quality of the simulation. An improved agreement with the experiment is judged not necessary as this will require an ever increased accuracy of the operating conditions of the test case, which are often not well known in industrial cases. Perfect agreement will not be achieved since anisotropy is not taken into account. Further study would enlighten the sensitivity of the transition to operating conditions. The possible improvement can be labeled as rather aesthetic. In the unsteady cases with industrial relevance, capturing the correct unsteady behaviour becomes more important than fine-tuning the quasi steady behaviour.

Chapter 5

Steady cascade

5.1 Introduction

The model has been applied to steady cascade test cases. The comparison with the experiments is done using experimental skin friction measurements or heat transfer coefficient values. Due to the strong acceleration of the flow, levels of turbulence intensity vary substantially along the front part of the profile suction side. This is simply because the level of turbulence kinetic energy k remains almost constant, but the velocity increases heavily. In this way the use of the leading edge turbulence intensity in the Mayle criterion for transition onset is no longer physically reasonable. The criterion has to be used with the local level of free-stream turbulence intensity.

5.2 VKI Cascade Test case

5.2.1 Geometry

The test cases have a turbine profile of the Von Karman Institute (VKI) and were measured at the University of Genova [2]. Reynolds number based on the chord and exit velocity for VKI1 is $Re_{2c} = 1.6 \times 10^6$ and for VKI2 $Re_{2c} = 0.59 \times 10^6$. A sketch of the computational domain is given in Figure 5.1a. The relevant geometrical characteristics of the cascade are listed in Table 5.1. The

grid consists of 110000 cells, and the first grid point is located at $0.0023mm$ from the wall, which ensures $y^+ < 0.6$. The experimental decay of free-stream turbulence along the blade is available, it can be derived from a series of u' profiles along the suction side. For comparison, the assumption has been made that 50% of the turbulent kinetic energy consists of streamwise fluctuations. The free stream values for k and ω at the leading edge are listed in Table 5.2. Also tabulated are the oncoming velocity U_i and the turbulence intensity at the leading edge Tu_{le}. The low aspect ratio of the cascade results in an acceleration of the flow in the decelerating part of the suction side. This has some influence on the experimental data, but is not taken into account in the numerical calculation.

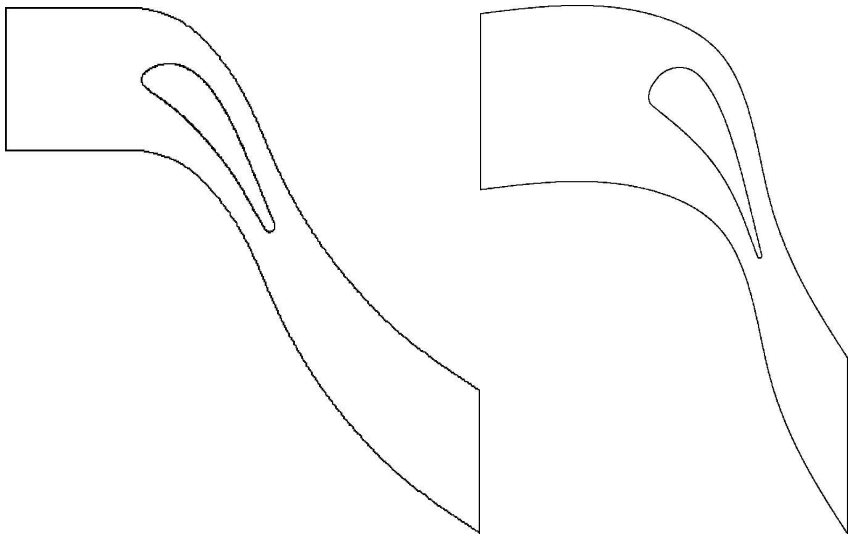

Figure 5.1: Computational domain of the VKI (left) and MUR (right) test cases. The MUR cascade is described in Section 5.3

blade chord	c	$300mm$
axial blade chord	c_{ax}	$197.5mm$
pitch to chord ratio	g/c	0.7
Reynolds number	Re_{2c}	1.6×10^6 and 0.59×10^6
inlet flow angle		0°
blade aspect ratio	h/c	1

Table 5.1: Geometrical characteristics of VKI test cases.

Case	$U_i(m/s)$	$Tu_{le}(\%)$	$k_{le}(m^2/s^2)$	$\omega_{le}(s^{-1})$
VKI1	28.1	1.35	0.45	1400
VKI2	10.5	1.8	0.09	475

Table 5.2: Description of $U_i(m/s)$ for VKI test cases. Further, numerical estimates are given for Tu_{le}, k_{le} and ω_{le}

5.2.2 Numerical results

Figure 5.2 shows the calculated skin friction profiles. The two cases have comparable free-stream turbulence intensity, but the Reynolds number differ. The start of transition is determined based on the local turbulence intensity. The results show that this results in good prediction of the start location on the suction side for VKI2, but slightly downstream of the experiment for the VKI1 case. In the VKI1 case, the overshoot in skin friction after transition is numerically not reproduced. This is not possible within the assumptions of the model. It is unclear what the reason for the high skin friction at completion of transition is. Upstream of transition, the levels of experimental laminar skin friction are somewhat higher than the calculated levels. Since pretransitional fluctuations do not cause substantial Reynolds stresses, the increased skin friction must be the result of an irregularity causing flow acceleration. In this location a decrease in momentum thickness was measured experimentally, as shown later.

On the pressure side, the flow undergoes acceleration from the leading edge stagnation point to the trailing edge. At the stagnation point, levels of turbulence intensity are very high ($Tu > 15\%$). However, the acceleration parameter is also very high, even above the relaminarisation limit of $K = 3 \times 10^{-6}$, presented by Mayle [46]. The lower Reynolds number leads to more extreme values of the local acceleration parameter, as explained in Eqn. (4.2). For the pressure side, the acceleration is increased with reduced Reynolds number. The high acceleration keeps the momentum thickness low, delays transition, and reduces the spot growth considerably after transition. Toward the trailing edge, the acceleration is less strong, so transition is able to complete for the high Reynolds case VKI1. This transition results in an increase in skin friction which is not observed in the experiment. In the experiment, however, the acceleration due to secondary effects may delay transition .

A more complete picture of the boundary layer state can be obtained by considering the boundary layer integral parameters. An important parameter

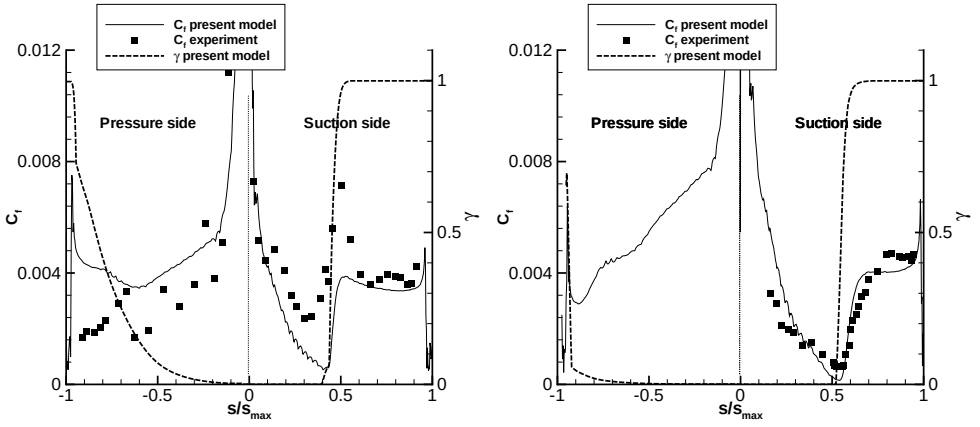

Figure 5.2: Skin friction evolution for cascades (left VKI1, right VKI2).

is the shape factor H_{12}, defined as the ratio of the displacement and momentum thickness.

$$H_{12} = \delta^*/\theta \tag{5.1}$$

with

$$\delta^* = \int_0^\infty \left(1 - \frac{U}{U_\infty}\right) dy = \text{displacement thickness} \tag{5.2}$$

$$\theta = \int_0^\infty \frac{U}{U_\infty}\left(1 - \frac{U}{U_\infty}\right) dy = \text{momentum thickness} \tag{5.3}$$

For a laminar boundary layer, the shape factor is about 2.2, and drops to about 1.5 for a turbulent boundary layer. Figure 5.3 shows the calculated shape factor profiles. On the suction side, again good agreement is obtained for VKI2. Both computational results have a similar shape. Shape factor values start at a laminar value of about 2.2. Due to the deceleration, values go up until the transition point, after which they decrease to the turbulent level of about 1.5. We can also observe that for the low Reynolds number case VKI2, the suction side prior to transition is close to separation as a result of the combination of low skin friction and high shape factor value (H_{12} about 3.5). For the low Reynolds case VKI2, the deceleration rate K is stronger. Nevertheless, no separation is observed, and transition is of attached bypass type. For the VKI1 case, transition is ended at $S = 0.5$, this is well captured by the model. Upstream of that location, the experimental values of shape factor are hard to interpret, since they seem to be much affected by the irregularity in the flow.

For the pressure side, the thin boundary layer makes it extremely difficult to obtain reliable results of shape factor value. The general observation is

that H_{12} levels remain high, so the boundary layer is laminar or only slightly transitional. Spectral analysis of the boundary layer velocity indicate that the boundary layer is transitional for the VKI1 case. Since in the computation, transition is completed near the trailing edge, shape factor values start to decrease toward the turbulent level in that region.

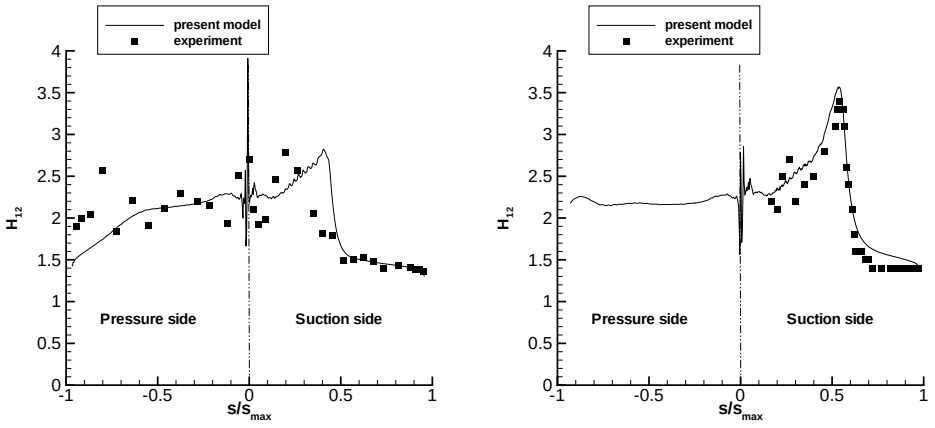

Figure 5.3: Shape factor evolution for cascades (left VKI1, right VKI2).

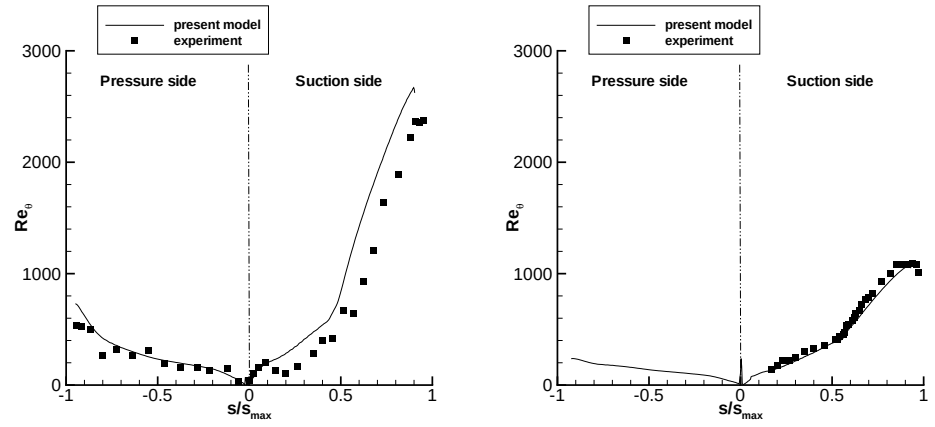

Figure 5.4: Re_θ evolution for cascades (left VKI1, right VKI2).

Figure 5.4 shows the calculated profiles of Re_θ. On the suction side, the general observation is that values of θ are higher for the high Reynolds case, and thus, so are the losses. The levels are well predicted by the computation. The transition is indicated by a change in slope by which θ increases, the location of this switch in slope is well predicted in both cases. In the VKI1 case, at $S = 0.1$, the value of Re_θ suddenly drops. This doesn't happen in the

simulation, and results in a constant offset with the experiment downstream of that location.

For the pressure side, the value of Re_θ remains low as a consequence of the acceleration. The losses resulting from the pressure side are consequently negligible compared to the suction side losses.

5.3 MUR cascade test case

5.3.1 Geometry

The model has also been tested at high Mach conditions on cascade test cases (MUR237, MUR235 and MUR232) with a turbine rotor profile of the Von Karman Institute [7]. A sketch of the computational domain is given in Figure 5.1b. The relevant geometrical characteristics of the cascade are listed in Table 5.3. The grid consists of 100000 cells, and the first grid point is located at $0.0005mm$ from the wall, which ensures $y^+ < 0.5$. The specifications of the calculations of the MUR test cases are given in Table 5.4. The incoming turbulence level Tu_i is measured $55mm$ upstream of the leading edge. Also the exit Mach number and the exit Reynolds number based on the chord are specified.

blade chord	c	$67.647mm$
axial blade chord	c_{ax}	$37mm$
pitch to chord ratio	g/c	0.85
Reynolds number	Re_{2c}	1×10^6
inlet flow angle		$0°$

Table 5.3: Geometrical characteristics of MUR test cases.

5.3.2 Heat transfer: modelling assumptions

For the MUR test cases, only heat transfer coefficent ($H = \frac{Q_w}{T_{01} - T_w}$) was measured. To calculate heat transfer coefficient, wall functions for fully turbulent flow were used. The first grid point is located well inside the viscous sublayer,

Case	$M_{2,is}$	$TU_i(\%)$	$Re_{c,2}$
MUR237	0.775	6	1.10^6
MUR132	0.68	0.8	1.10^6
MUR235	0.927	6	1.10^6
MUR129	0.84	0.8	1.10^6
MUR232	1.061	6	1.10^6
MUR210	1.076	1	1.10^6

Table 5.4: Description of MUR test cases.

so the linear law for a thermal conduction sublayer is applied.

$$T^* = Pr\ y^* + \frac{1}{2}\rho Pr \frac{C_\mu^{1/4} k^{1/2}}{Q_w} U^2 \tag{5.4}$$

$$T^* = \frac{(T_w - T)\rho c_p C_\mu^{1/4} k^{1/2}}{Q_w} \tag{5.5}$$

$$y^* = \rho c_p \frac{C_\mu^{1/4} k^{1/2}}{\mu} y \tag{5.6}$$

$$\tag{5.7}$$

So, the resulting wall heat flux

$$Q_w = \frac{|T_w - T|\ k_f}{y} - \frac{1}{2}\frac{\mu\ U^2}{y} \tag{5.8}$$

k_f is the thermal conductivity of the fluid. The second term in the right hand side of Eqn. 5.4 is activated for compressible flow calculations. The influence of Mach number is included in the velocity scale U. For increasing Mach number (increasing velocity U), the wall heat flux reduces.

The increase in turbulence kinetic energy has no direct modelled influence on the heat flux through the thermal sublayer. However, the turbulent kinetic energy k has an influence on the temperature diffusion in the energy equation. The coefficient in the temperature diffusion term is the effective conductivity k_{eff}, which is the sum of the molecular thermal conductivity k_f, and the turbulent thermal conductivity (here transitional because of the weighted turbulent viscosity):

$$k_{eff} = k_f + \frac{c_p\ (\tau \mu_t)}{Pr_t} \tag{5.9}$$

By default the turbulent Prandtl number Pr_t is 0.85 in the energy equation. So after transition, values of k and μ_t increase, which lead to an increase in

diffusion of temperature into the thermal sublayer. As a result the temperature difference at the wall $|T_w - T|$ increases, and consequently also the wall heat flux.

The effect of the free-stream turbulence level on the laminar boundary layer has been incorporated as proposed by Smith and Kuethe [72]:

$$\mu_{t,lam} = 0.164\rho\frac{Tu\%}{100}U_\infty y \tag{5.10}$$

The distance from the wall $'y'$ has been limited outside the boundary layer. This extra viscosity is added to the laminar viscosity in the laminar part of the Navier-Stokes calculation. The turbulent viscosity is left unaltered. The effective viscosity used in the Navier-Stokes part of the calculation is thus:

$$\mu_{eff} = [\mu + (1-\tau)\mu_{t,lam}] + \tau\,\mu_t \tag{5.11}$$

5.3.3 Numerical results

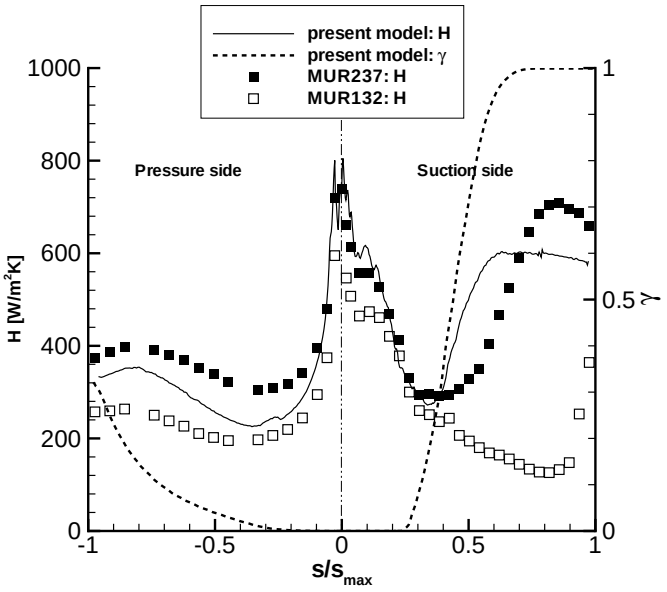

Figure 5.5: Heat transfer coefficient evolution for MUR237 cascade. (MUR132 is also shown as corresponding case for low turbulence level)

Figure 5.5 shows the calculated surface heat transfer coefficient ($H = \frac{Q_w}{T_{01}-T_w}$) and wall intermittency profile for the MUR237 ($Tu_i = 6\%$) test

case. The experimental heat transfer is given for MUR237 and MUR132 ($Tu_i = 0.8\%$). The local turbulence intensity is used in the Mayle correlation to determine start of transition. This means 1.5% for the suction side and 12% for the pressure side. The transition location is for all three calculated cases identical, since the inlet turbulence intensity is identical, and the transition location is independent of the Mach number. The Mach number affects the acceleration parameter K, and the spot growth rate β. It results in an slower growth of intermittency with increasing Mach number. In the transition region, the heat transfer coefficient goes up faster than in the experiment. Further, the fully turbulent ($\tau = 1$) heat transfer coefficient is lower than the experimental measured one. These two observations are general for all three test cases. This is a deficiency of the turbulence model. More specific, the assumption that turbulent diffusion of temperature can be modelled with a constant turbulent Prandtl number in the transitional and fresh turbulent region is too simplified. The MUR132 experiment result is added to the plot for ease of detecting the transition location. Due to the very low inlet turbulence intensity, transition location is shifted much downstream, so this curve represents mainly the laminar reference heat transfer. Simulated transition starts at $S = 0.25$, and is completed at about $S = 0.7$. Before the transition location, the two experimental curves differ only slightly, a result of the difference in free-stream turbulence intensity acting on the laminar boundary layer. In this region, the extra viscosity $\mu_{t,lam}$ is activated, according to Equation (5.10). After transition, the two experimental curves differ significantly. This indicates that the simulated transition location is in good agreement with the experiment. During transition the simulated H goes up, and remains almost constant afterwards.

Figure 5.6 shows the calculated surface heat transfer coefficient and intermittency profile for the MUR235 ($Tu_i = 6\%$) test case. The experimental heat transfer is given for MUR235 and MUR129 ($Tu_i = 0.8\%$). The exit Mach number of the MUR235 is somewhat higher than in the previous test case MUR237. Simulated transition starts again at the same $S = 0.25$, but is completed at about $S = 0.8$, indicating a slower growth of intermittency. Together with the longer transition region, also a longer region of increasing heat coefficient H is simulated. In the experiment, at about $S = 0.7$, the H goes up fast, as the result of a light shock. Due to the somewhat coarse streamwise resolution of the grid, this shock is not well captured in the simulation.

For the highest Mach number case MUR232, shown in Figure 5.7, the growth rate of the intermittency is significantly reduced. As a result, the difference between the transitional and the laminar heat transfer coefficient

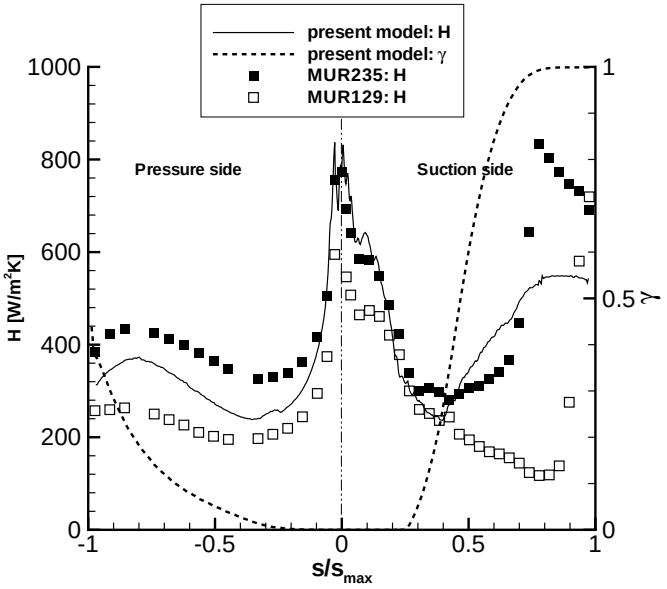

Figure 5.6: Heat transfer coefficient evolution for MUR235 cascade. (MUR129 is also shown as corresponding case for low turbulence level)

becomes small. A strong shock appears at $S = 0.85$. The shock is also seen in the simulation, but less sharp. Nevertheless, after this shock, heat transfer is much enhanced in experiment and simulation. The increase of heat transfer after the shock is not a result of the transition model, since transition is almost completed at that location. It is clear that the transition location is much upstream of the shock location. Turbulence production is very strong, both in experiment and simulation. After the shock, the temperature diffusion toward the wall is much enhanced.

At the pressure side, the results are similar for all cases because the acceleration is similar. Transition is detected very close to the leading edge, but the growth of intermittency is low due to the high acceleration. The calculated heat transfer coefficient is about halfway the laminar and the experimental value.

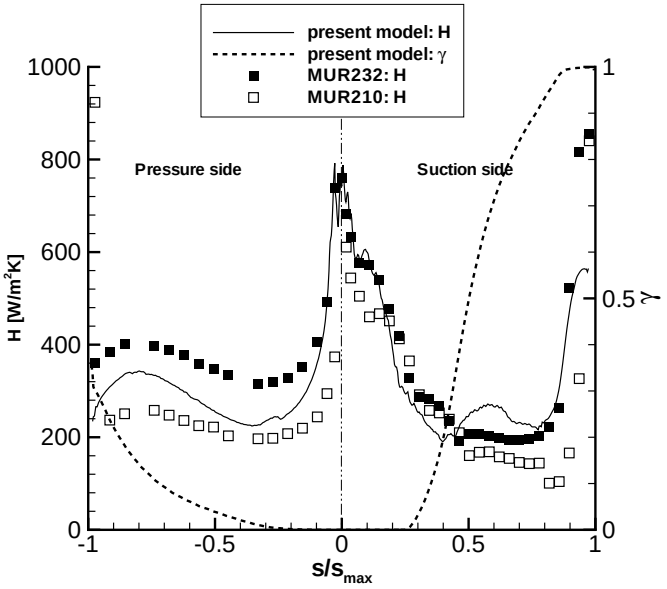

Figure 5.7: Heat transfer coefficient evolution for MUR232 cascade. (MUR210 is also shown as corresponding case for low turbulence level)

5.4 Conclusion

The high acceleration near the leading edge changes the turbulence intensity along the leading edge part of the blade substantially. The use of the Mayle criterion based on leading edge turbulence intensity is no longer valid. Instead, the local turbulence intensity at the boundary layer edge is used to evaluate the Mayle criterion for start of transition. The results show good accuracy for prediction of start of transition location.

Of the VKI1 and VKI2 cases, only the VKI2 measurement appears to be reliable. For this case, very good agreement is observed for skin friction, shape factor and momentum thickness. This illustrates that the good results on the steady flat plate cases can be reproduced on steady cascade cases.

Under high Mach number conditions, the prediction criterion for transition location remains valid and results in accurate predictions. In the transition region, the predicted values of heat transfer coefficient are somewhat higher than the experiment. The fully turbulent heat transfer coefficient is somewhat lower than the experimental one. Although the agreement is not perfect, the

model shows to be able to incorporate the quantitative influence of Mach number on transition. Modeling of *transitional heat transfer* is not an objective of this thesis, and appears to be an item of further research. Skin friction data are not often available in high Mach test cases. Wall functions for fully turbulent heat transfer were used in these transitional calculations.

Chapter 6

Unsteady cascade test cases

6.1 Introduction

In real gasturbine engines, the wakes from a bladerow impact on downstream bladerows. As any wake, they consist of a velocity deficit with an elevated level of turbulence intensity. Their effect on the downstream bladerow is thus twofold. First, the high turbulence intensity induces transition upstream of the steady case with only the background turbulence. Second, the velocity deficit alters locally the loading of the blade. This is the kinematic wake impact which has important consequences on a separation bubble.

The wakes are convected with the flow into the blade passage, where they are bent and stretched. Some production of turbulence is associated with this mechanism. In the model, the local leading edge turbulence intensity intensity is used to determine the transition location. The transition model is thus dependent on the inlet turbulence intensity level of the wakes, and on the production in the blade passage. A lot of effort has to be put into the implementation of the wakes into the calculation. But still, the production in the blade passage is a source of possible error. A rough way to cope with this is proposed by Lardeau et al. [36]. They use the Mayle transition criterion using the inlet background turbulence intensity irrespective of the wakes, so for a fixed level of $Re_{\theta t}$. We show here that good agreement can be obtained while using the local free stream turbulence intensity for onset of transition.

6.2 T106A

The T106A test cascade, for low Reynolds numbers and low free-stream turbulence intensity was experimentally measured by Stieger and Hodson [77, 78]. For these operating conditions, transition is mainly due to kinematic wake impact on a separation bubble. This is not very representative of the real engine turbine conditions. Older data from the EC-project TURMUNSFLAT are used to see the influence of an increased Reynolds number. Finally, the influence of a higher background turbulence intensity is simulated based on the very recent results from Opoka and Hodson [56]. The higher background turbulence intensity is more representative for the real engine turbine conditions. There is mixed importance of wake turbulence and wake kinematics on transition. Additional data were obtained by private communication on results obtained in the EC-project UTAT.

6.2.1 Geometry

The flow is unsteady due to incoming wakes from a moving bar system located $0.33c_{ax}$ upstream of the cascade leading edge. Figure 6.1 shows a sketch of the experimental setup. The basic parameters are listed in Table 6.1. The computational grid consists of a T106 profile with pitchwise periodic boundary conditions. The moving bar system is not included in the computation. Instead, a moving wake profile is used as inlet condition. The inlet of the computational domain is located between the bars and the leading edge at $0.175c_{ax}$ upstream in axial direction of the leading edge. In Figure 6.2, a zoom on the leading edge region of the blade shows the boundary layer refinement on the profile. The grid consists of 80600 cells from which 53600 are located in the boundary layer. The y^+ value in the first grid point in wall vicinity is below 0.5. A stretching factor of 1.03 has been applied perpendicular to the wall such that the viscous region of the boundary layer ($y^+ < 50$) contains more than 35 cells. Per pitchwise traverse, 800 time steps are used. This high accuracy is necessary to properly simulate the unsteady movement of the wake, as illustrated by Lardeau et al. [35].

blade chord	c	$198mm$
axial blade chord	c_{ax}	$170mm$
pitch to chord ratio	g/c	0.799
Reynolds number	Re_{2c}	1.6×10^5 and 2.6×10^5
undisturbed inlet flow angle	α_1	$-37.7°$
design exit angle		$63.2°$
bar diameter	d	$2.05mm$
bar pitch/ cascade pitch		1.00
axial distance bars to LE		$0.33c_{ax}$
flow coefficient	U_{1x}/U_b	0.83
free-stream turbulence intensity		$< 0.5\%$

Table 6.1: T106A cascade.

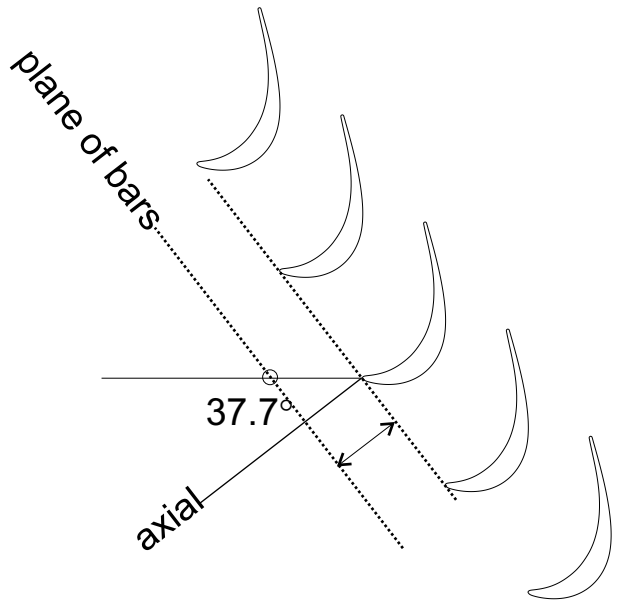

Figure 6.1: Experimental setup of T106A test case.

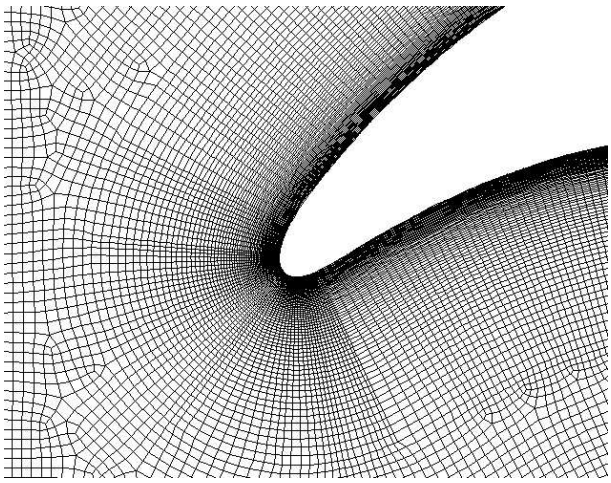

Figure 6.2: Grid at the leading edge region of the T106A profile.

6.2.2 Concept of a moving wake profile at the inlet

For the unsteady cascade test cases, the periodic impact of the wakes from upstream blade rows is replaced in the experiments by bars passing upstream of the instrumented blade. The diameter of the cylindrical bars has been chosen to produce a wake with a velocity deficit and a turbulent kinetic energy that is comparable to that of a blade wake. From a numerical point of view, there are two possibilities to include the wake into the computation. The first is to fully resolve the bars in a moving grid upstream of the blade. Besides being computationally expensive, it shows poor results, especially in a 2D calculation. The advantage however is that no experimental input is needed. In 3D flow, the unsteady vortex shedding behind a cylinder results in a highly unsteady wake. The vortices break up in the span-wise direction relatively quickly after the cylinder. When performing 2D unsteady calculations, it is possible to resolve the shedding by using a fine enough time step, but resolving the break-up of the shed vortices is not possible. As a consequence, the shed vortices extend much further downstream of the cylinder, compared to experiments. If a larger time step is used, the shedding is not resolved, and the wake has less resolved and more modeled turbulence. Hereby, the recirculation region behind the cylinder is too long, and results in a too strong velocity deficit behind the cylinder. This is a typical defect of RANS solutions for bluff-body flows. The Strouhal number of a bar is defined as $S = nd/U_\infty$ and is equal to 0.21. For the flow around a bar at $Re = 2600$, the shedding period is equal to $5.27 \times 10^{-4} s$. One wake passage is $0.0246s$, this means that by using 800 time steps per wake passage, about 17 time steps per shedding

period are used. So, the shedding is not well resolved.

A second option is to replace the bar by a sliding wake profile applied at the inlet of the calculation. This wake profile is a time averaged (over the wake shedding period) representation of the wake that can represent the downstream evolution of the wake profile if the inlet profile is chosen carefully. In this case, experimental results of the isolated bar wake have to be available. Also a steady RANS calculation has to be performed to asses the downstream evolution of the wake. For this option, the inlet can be located close to the blade leading edge, which reduces the grid size, and the stream-wise length of the wake prior to wake impact. In doing so, the effect of numerical diffusion on the wake will be limited.

6.2.3 Precursor calculation for the incoming wake

A sliding wake profile has been applied at the inlet. It is determined from a precursor calculation. A 2D RANS computation of the wake of a stationary cylinder at $Re = 2600$ is compared with experimental results of Stieger and Hodson. The Reynolds number is the same as for the moving bar wake in the $Re_{2c} = 2.6 \times 10^5$ case. The experimentally measured wake spreading is computed by steady RANS between $x/d = 5$ and $x/d = 62$ on a rectangular grid of $150mm \times 40mm$, see Figure 6.3. Only half of the wake is computed. In the wake center, a symmetry condition is applied. Wake characterizing parameters at $x/d = 5$, such as wake width and velocity deficit, are extracted from the experimental results. Since the turbulent velocity fluctuations at that location are highly anisotropic, the level of turbulent kinetic energy used in a steady isotropic RANS simulation cannot be that of the experiment. The turbulent kinetic energy in the wake and the background dissipation have been used as degrees of freedom to match the experimental results at $x/d = 62$. The wake behind a cylinder has a self-similar profile as described by Pope [60]. Therefore we impose self-similar profiles at the inlet of the 2D RANS calculation:

$$U = U_\infty - (U_\infty - U_{center}) \exp\left[-(\ln 2)\left(\frac{y}{y_{1/2}}\right)^2\right] \tag{6.1}$$

$$k = k_\infty + (k_{center} - k_\infty) \exp\left[-(\ln 2)\left(\frac{y}{y_{1/2}}\right)^2\right] \tag{6.2}$$

U_{center}/U_∞	0.7
$y_{1/2}$	$1.8mm$
k_{center}	$6.0m^2/s^2$
k_∞	$0.005m^2/s^2$
ω_∞	$80s^{-1}$

Table 6.2: T106A; inlet condition precursor RANS computation.

The inlet conditions for the specific dissipation are those described by Wilcox [90]:

$$\omega = \omega_\infty + C_\mu^{1/4} \frac{\sqrt{k}}{l_{mix}} \tag{6.3}$$

$$l_{mix} = 0.18 y_{1/2} \tag{6.4}$$

The inlet conditions ($x/d = 5$) are listed in Table 6.2. The correspondence with the experiments at $x/d = 62$ for velocity and turbulence intensity is shown in Figure 6.4. By this good correspondence, we are sure that the spreading of the wake behind the cylinder is well reproduced by the RANS-calculation. This allows us to determine the profiles for velocity and turbulent quantities at the inlet plane of the calculation. The profiles at plane $x/d = 42.7$ under the relative flow angle $\beta = 63.2°$ are used. For $Re_{2c} = 1.6 \times 10^5$, Stieger and Hodson do not provide experimental results of the cylinder wakes. For this case, wake profiles are rescaled for the lower inlet velocity. The ratios of U_{center}/U_∞ and k_{center}/U_∞^2 are left unaltered, while the values of U_∞ and k_∞ are adjusted.

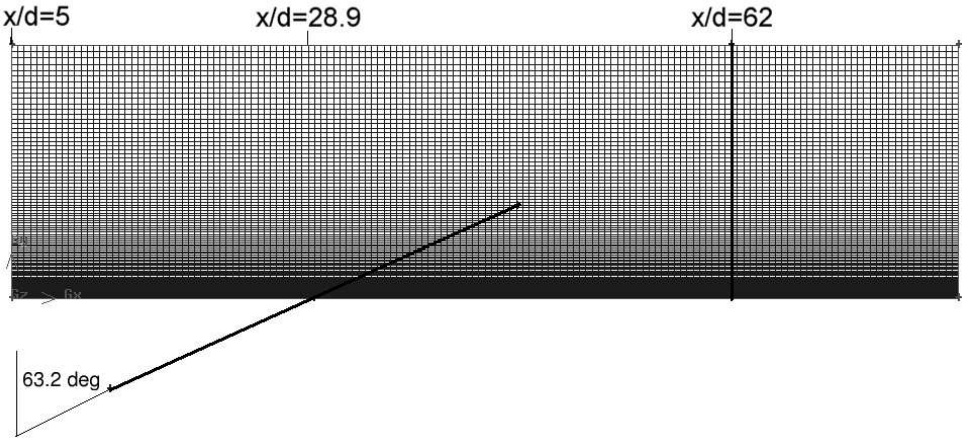

Figure 6.3: Grid used for steady RANS wake simulation.

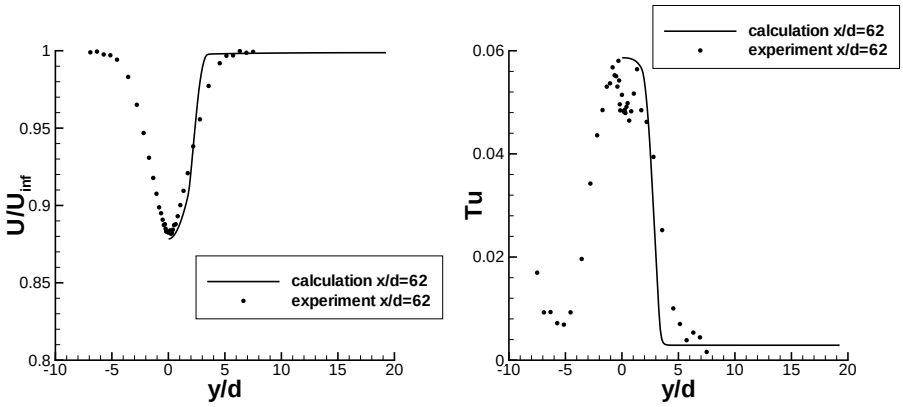

Figure 6.4: Matching the wake of a cylindrical rod with the experimental results at $x/d = 62$.

6.2.4 Inlet conditions

The inlet is very close to the leading edge of the profile. Thus, potential effects are important at that location. This means that the pressure drop near the suction side influences the surrounding region, i.e. the part of the inlet plane close to the suction side. The same accounts for the high pressure region near the pressure side. To obtain the time-averaged potential influence in the inlet plane, a steady viscous calculation has been performed with a constant total pressure inlet far upstream of the leading edge, see Figure 6.5. The velocity magnitude and angle at $0.15c$ upstream of the cascade inlet plane are extracted and used as inlet conditions in the unsteady calculation (close to the leading edge). The velocity deficit of the sliding wake profile is superimposed on these inlet conditions. The wake velocity deficit and wake turbulent kinetic energy are obtained from the RANS precursor wake calculation. The time averaged (average over the wake period) velocity contour shown in Figure 6.6 clearly shows that the velocity distribution at the inlet is in good agreement with Figure 6.5.

From the RANS wake calculation, the profiles at plane $x/d = 28.9$ under the relative flow angle $\beta = 63.2°$ are used as inlet conditions for the T106 cascade calculation. This wake profile is applied as a sliding wake profile at the inlet. Figure 6.7 shows the inlet velocity at a random time instant and the time averaged inlet velocity. The procedure ensures that the computation of the wake has good agreement with the experimentally measured behaviour. The time-averaged pressure distribution over the rear part of the profile is in good agreement with the experiment, as illustrated in Figure 6.8. The pressure coefficient is defined by (6.5), with p_{01} the total inlet pressure and p_{2is} the isentropic outlet pressure.

$$C_p = \frac{p_{01} - p}{p_{01} - p_{2is}} \tag{6.5}$$

In Table 6.1 the inlet angle of the steady experiment is given. In the unsteady experiment, the movement of the bars alters the time-averaged inlet angle substantially. A time averaged inlet angle of 39.7°, so 2° larger than the undisturbed value, is used in the calculation in order to get a good agreement with the experimental pressure distribution of the leading edge part of the profile. The agreement is perfect for $Re_{2c} = 160000$. For $Re_{2c} = 260000$, the numerical pressure distribution is identical to the $Re_{2c} = 160000$ case due to the same inlet angle. By slightly changing the inlet angle, the agreement with the experimental distribution could be improved for the leading edge region, but not for the maximal suction region. Therefore, we did not vary the inlet

angle and we accept the small discrepancy between numerical and experimental pressure distributions for $Re_{2c} = 260000$. We have no explanation why the experimental pressure distributions for the two cases are not exactly the same.

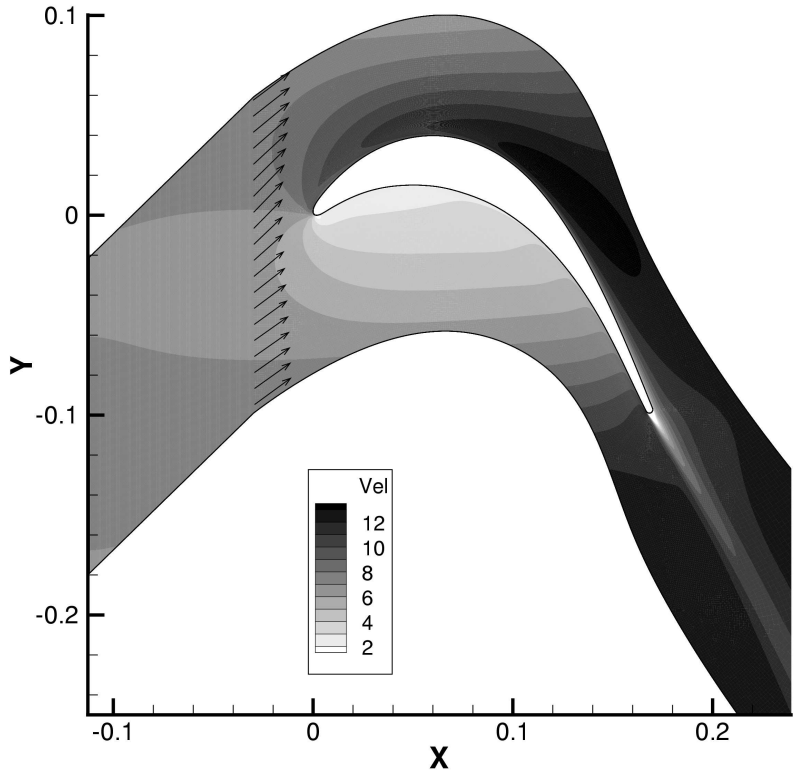

Figure 6.5: Velocity contours of the T106A profile ($Re_{2c} = 160000$) using the constant total pressure inlet.

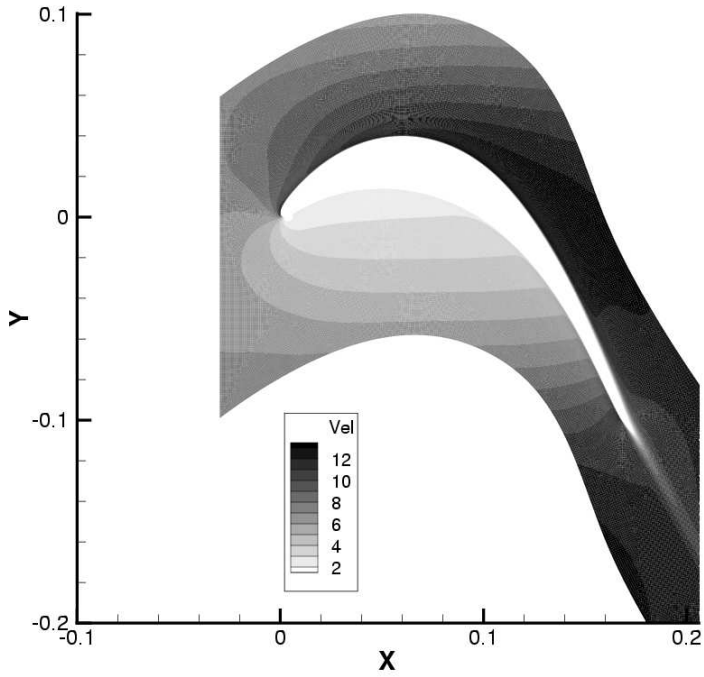

Figure 6.6: Wake period averaged velocity contours of the T106A profile ($Re_{2c} = 160000$) using the velocity vectors from the precursor calculation at the inlet.

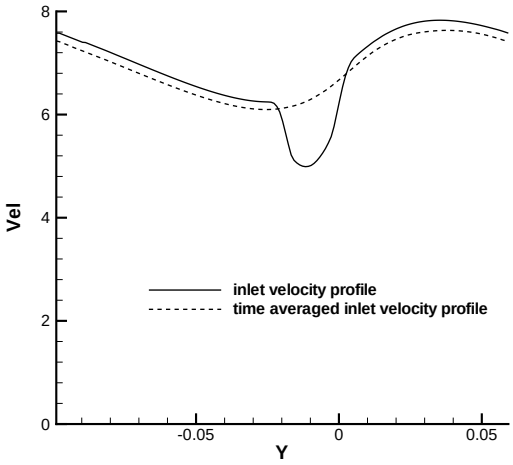

Figure 6.7: Velocity inlet profile in the unsteady calculation of the T106A $Re_{2c} = 160000$ cases.

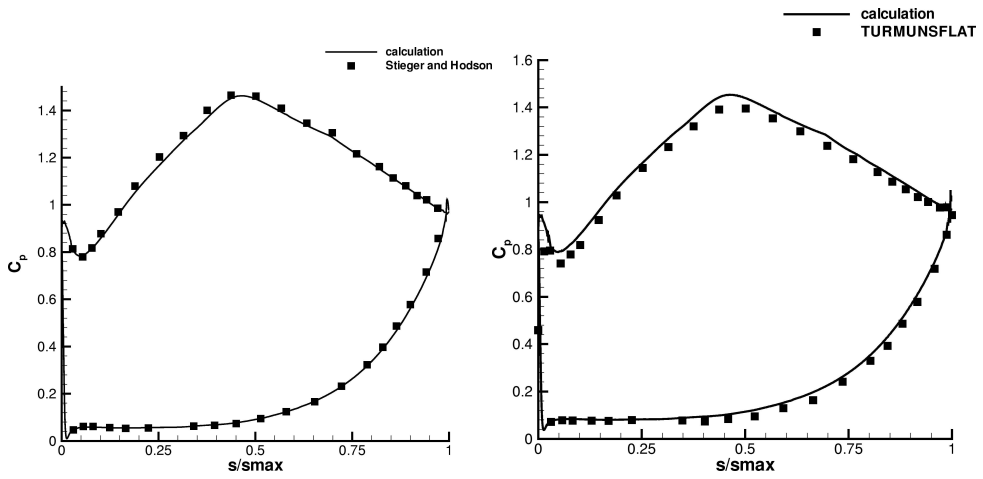

Figure 6.8: T106A; Time-averaged pressure distribution (left $Re_{2c} = 160000$; right $Re_{2c} = 260000$).

6.2.5 T106A (Low $Re_{2c} = 160000$, Low $Tu = 0.5\%$)

For a typical thin LP turbine blade, about 60 percent of the profile losses are created on the suction side. We therefore have particular interest in the unsteady transition on the suction side. On the suction side, the three transition criteria are used in competition with each other. For the pressure side, the bypass transition mechanism is applied. Figure 6.9 shows the turbulence kinetic energy contours (scaled with exit kinetic energy) at one instant during the wake period. For the suction side, calculated and experimental wakes are very similar. The maximum level of TKE is well reproduced, as well as the subtle decrease of TKE due to flow acceleration near the front part of the LE. Disabling the turbulence production upstream of the LE plays a crucial role in obtaining this result. The agreement proves the quality of the applied inlet conditions and the numerical algorithm, together with a careful use of the turbulence model. Perturbation velocity vectors with respect to steady flow, for the same time instant, are shown in Figure 6.10. The wake can be seen as a negative jet pointing toward the moving bar. The result inside the blade channel is a jet pointing toward the suction side. Due to the kinematic wake effect, the suction side boundary layer is accelerated (A) and decelerated (B).

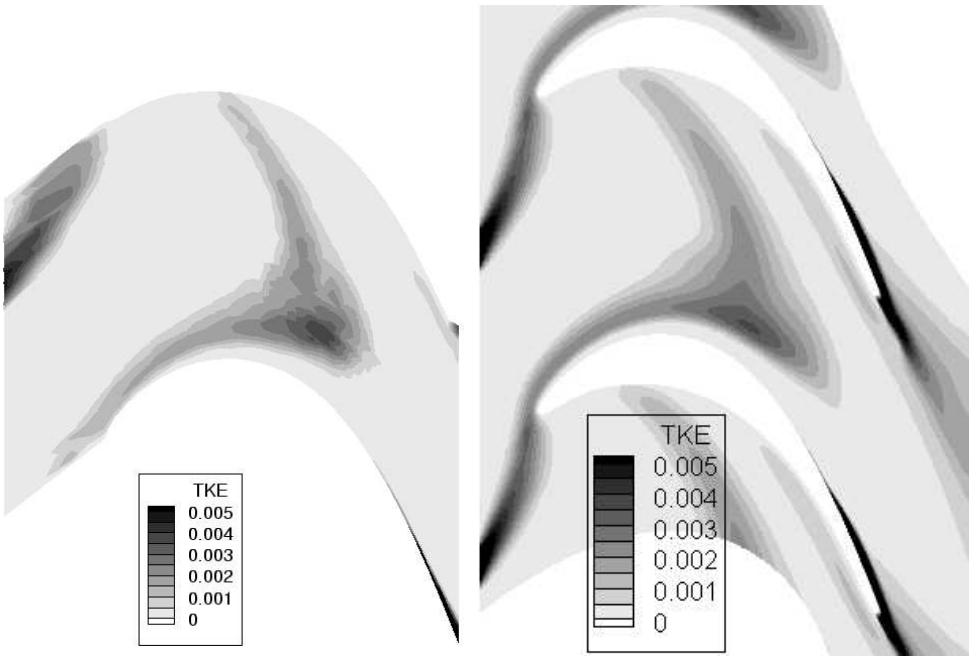

Figure 6.9: T106A (160000, 0.5%); Instantaneous turbulent kinetic energy k contours (left: experiment — right: computation).

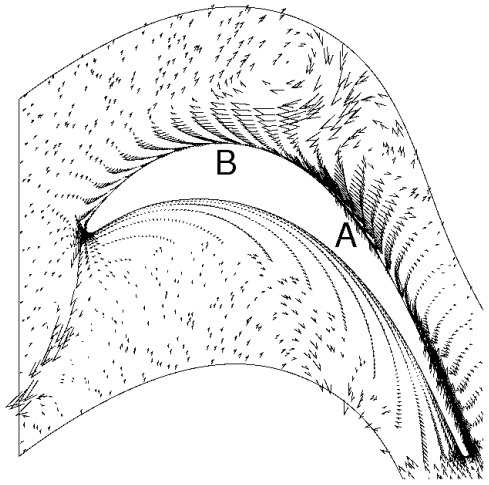

Figure 6.10: T106A (160000, 0.5%); Instantaneous perturbation velocity vectors.

In Figure 6.11a, the wall shear stress is plotted on an $S-T$ diagram over the entire suction surface. Zones with negative wall shear stress have been blanked. The space coordinate S is the relative suction surface length s/s_{max}. The time coordinate T is scaled with the wake period. The solid lines A and B on the $S-T$ diagram represent a particle path of maximal (A) and minimal velocity (B). The zone between the lines A and B indicates the extension of the *kinematic wake impact*. When looking at time evolution (horizontal lines from bottom to top) we see the periodic appearance of a separation bubble ($S = 0.75$, $T = 0.5$) followed by the kinematic wake impact between lines A and B. The boundary layer with the separation bubble undergoes a rapid succession of acceleration and deceleration, which leads to break-up of the separation bubble into three roll-up vortices and causes almost immediate transition. Finally, the roll-up regions are ended due to *wake turbulence induced transition*. The solid lines represent velocity paths of about the free-stream velocity. The path of the roll-up vortices corresponds to a much lower velocity. A zoom of the trailing edge in Figure 6.12 shows the perturbation vectors for a time instant when the trailing edge is decelerated by the kinematic wake effect (B). Three roll-ups are clearly visible.

The $S-T$ plot of turbulence intensity, shown in Figure 6.11b, indicates that the kinematic wake impact precedes the increased levels of Tu due to wake turbulence. All transition phenomena are visible in the $S-T$ plot of the starting function, shown in Figure 6.11c. First, before kinematic wake impact (so under line A), quasi-steady transition over a growing separation bubble is seen. Then, kinematic wake impact transition follows ($F_s = 2$) since the flow is separated and the free-stream turbulence intensity is higher than 2.12%. Finally, together with the boundary layer deceleration due the wake kinematic impact, the wake turbulence is convected and diffused into the boundary layer, and causes wake turbulence induced bypass transition ($F_s = 1$ location moves upstream). After the wake passage, the trigger to transition disappears. The intermittency near the wall is destroyed and the intermittency in the boundary layer is convected downstream. This phenomenon is visible by comparing the $S-T$ plot of wall intermittency and averaged turbulence weighting factor, as shown in Figure 6.13. The wake turbulence induced transition starts in the bulk of the boundary layer, and grows toward the wall. The non-zero values of averaged intermittency upstream of $S = 0.5$ indicate the wake path. Since at these locations $\gamma = 0$, essentially the free-stream intermittency ζ is contributing to the τ_{avg} integral. During the wake passage, turbulent fluctuations enter the outer part of the underlying boundary layer, here represented by free-stream intermittency penetrating deeper into the boundary layer.

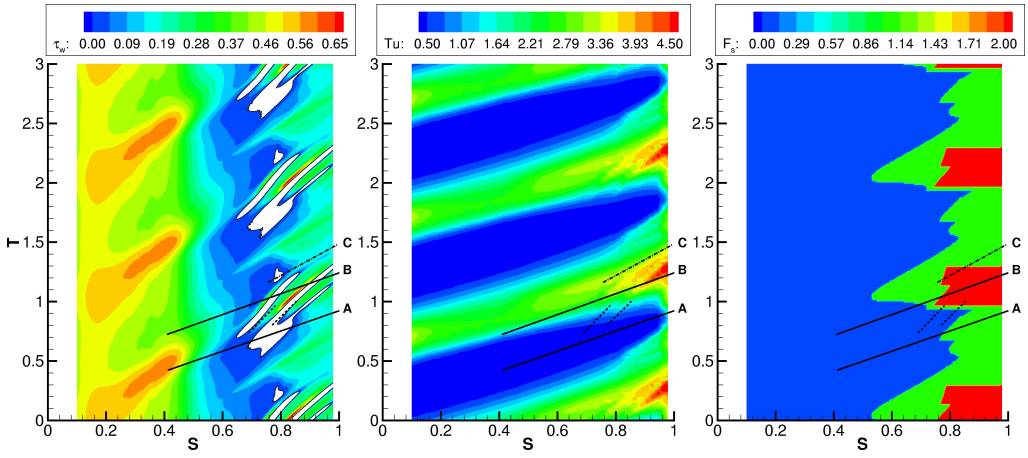

Figure 6.11: T106A (160000, 0.5%); $S-T$ diagram over the suction side of the wall shear stress, the free-stream turbulence intensity and the values of starting function.

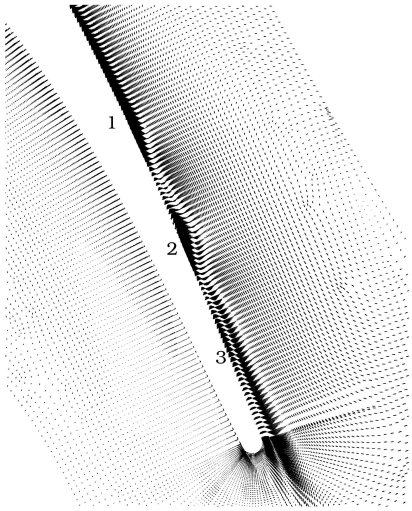

Figure 6.12: T106A (160000, 0.5%); Perturbation vectors near the trailing edge.

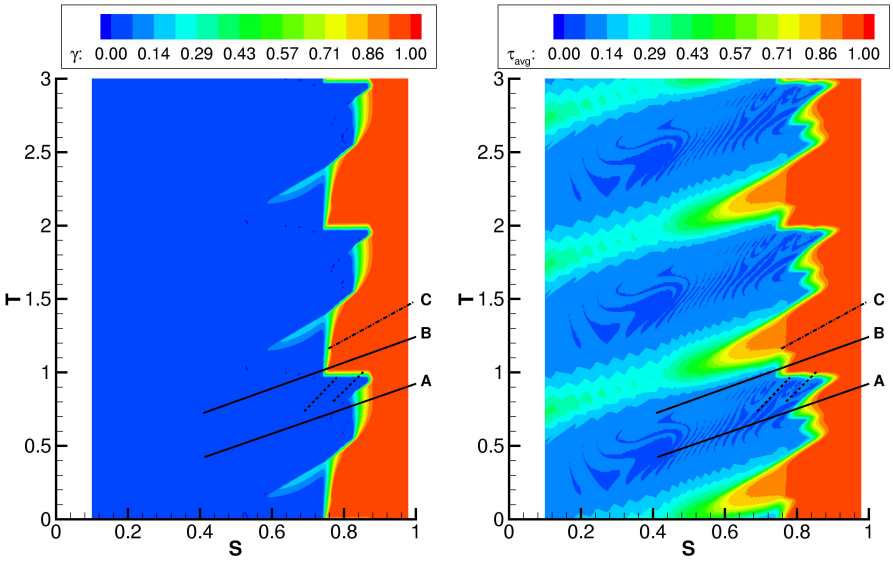

Figure 6.13: T106A (160000, 0.5%); $S-T$ diagram of the wall intermittency (left) and the boundary layer averaged intermittency (right).

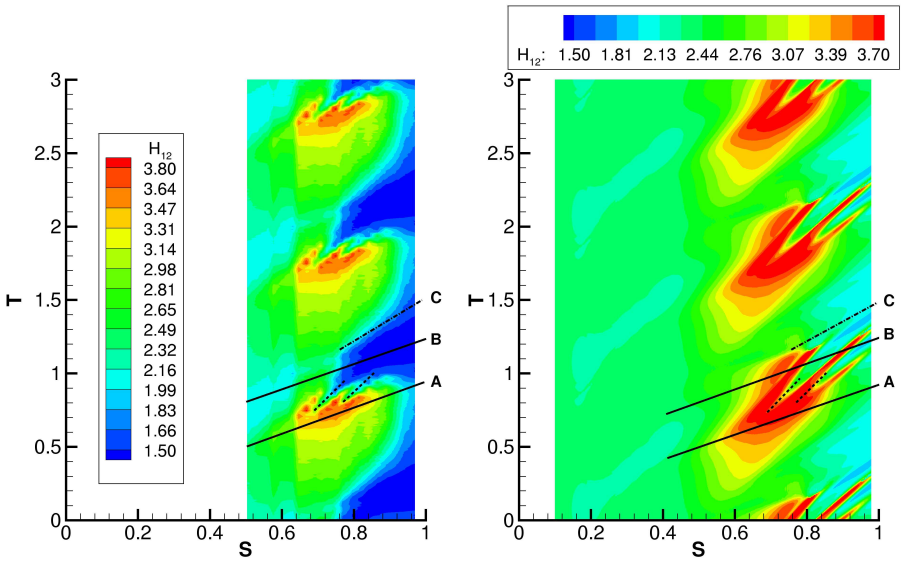

Figure 6.14: T106A (160000, 0.5%); $S-T$ diagram of the experimental (left) and computed (right) shape factor.

The unsteady nature of the transition starting in the bulk of the boundary layer and going toward the wall affects the interpretation of experimental intermittency measurements. The shape factor is mostly affected by the averaged intermittency in the boundary layer, whereas fluctuations in (quasi) wall shear stress are only affected by the wall intermittency. These are not necessarily identical.

Comparison with the experiments is done by an $S - T$ diagram of shape factor in Figure 6.14. High values of shape factor occur at S values of 0.6 to 0.8. These high values indicate velocity profiles that are separated, or have the tendency to separate. There is also agreement with the wall shear stress diagram in Figure 6.11. Attention has to be made that features in shape factor and wall shear stress are not identical. Due to the incoming wakes, the velocity profiles are distorted. This has a different result on shape factor and on wall shear stress. Nevertheless, the regions of low wall shear stress and high shape factor correspond. The appearance of the separation and the transition into roll-ups is well represented by the computation. However, in the calculation, the roll-up vortices extend too far in time. Our interpretation is that this is a consequence of the 2D representation of the flow. In the experiment, roll-up vortices break down in the span-wise direction. This transfers a high amount of energy to the boundary layer, explaining the lower levels of shape factor. This phenomenon is not well captured in the simulation, since shape factor values of 2 indicate a transition which is not completed. We are convinced that for flow with low Reynolds number, there is need for VLES or even LES models to resolve the breakdown of the roll-up vortices into turbulence. So, we consider the too low speed by which the roll-up vortices lead to turbulence as an inherent shortcoming of a RANS turbulence model. We remark that Lardeau and Leschziner [34] obtain the same phenomenon for transition simulation with a non-linear eddy viscosity model without intermittency modelling. For higher Reynolds number cases or cases with higher background turbulence intensity[1], the roll-up vortices are less strong and their transition to turbulence is captured better, as we will see further.

On the other hand, the computational wake turbulence induced transition region is larger than the experimental one. The dash-dot line C represents the experimental beginning of the calmed region. In the simulation, the region of experimental observed calming is covered by wake induced transition. So the calming is simulated later in time. Referring to Figure 6.11b and 6.11c, and Figure 6.13, one can see that this phenomenon is not due to a deficiency of

[1]T106A ($Re_{2c} = 260000$, $Tu = 0.5\%$) described in section 6.2.6 and T106A ($Re_{2c} = 160000$, $Tu = 4\%$) described in section 6.2.7

the intermittency model. The starting function is correctly activated under the high Tu-level zone of the wake. The intermittency both at the wall and in the bulk of the boundary layer is correctly brought to unity. The observation is that the production of turbulent kinetic energy by the turbulence model is somewhat too large in the rear zone of the incoming wake, leading to a turbulence tail which is unphysical. The reason for this TKE *tail* trailing behind the wake, is explained in the description of the high Tu case T106A ($Re_{2c} = 160000$, $Tu = 4\%$), described in section 6.2.7. A similar phenomenon was observed by Lardeau and Leschziner [34] with a non-linear eddy viscosity model without intermittency modelling. Further, they obtain too early a start of transition, which is a typical result for a transition simulation without intermittency modelling.

Based on the momentum thickness, shown in Figure 6.15, which is an indicator of the losses, it is even more clear that the wake turbulence induced region is too large. The peak value of momentum thickness above line C is too high compared to the experimental value. On the other hand, the increase of momentum thickness resulting from the breakdown of the roll-up vortices is computationally not captured.

The overall conclusion for the test case T106A ($Re_{2c} = 160000$) is that the physical transition phenomena are qualitatively correctly described but that quantitative differences occur. These are due to deficiencies in the turbulence model itself and to the impossibility to represent roll-up breakdown in a 2D RANS simulation.

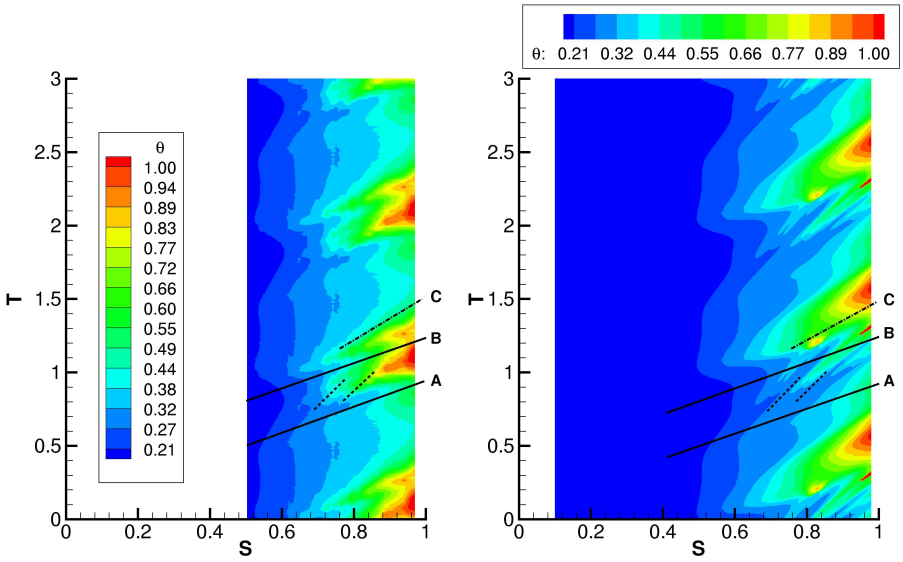

Figure 6.15: T106A (160000, 0.5%); $S-T$ diagram of the experimental (left) and computed (right) momentum thickness.

6.2.6 T106A (Medium $Re_{2c} = 260000$, Low $Tu = 0.5\%$)

The flow patterns for this test case and the previous one are similar, and thus, the intermittency equations react similarly. This is visible in the averaged intermittency and starting-function patterns shown in Figure 6.16. There are however, quantitative differences due to the higher Reynolds number. The break-up of the roll-up vortices is enhanced and the wake turbulence induced region is larger. This has as a consequence that the boundary layer does not separate before the next wake passage. It has high shape factor values indicating nearly separated profiles. Nevertheless, the wake impact causes the formation of roll-up vortices. These can be seen in the numerical result for shape factor shown in Figure 6.17b. In the experimental results, shown in Figure 6.17a, the roll-up vortices are not visible. The high shape factor zone preceding the roll-up vortices is experimentally detected. One has to take into account the much lower resolution of the experimental data for $Re_{2c} = 260000$ compared to these for $Re_{2c} = 160000$. From later experiments with much better resolution [97], it is known that kinematic wake impact on a laminar boundary layer near separation leads to roll-up vortices. So, we cbig in thean be confident that the numerically obtained roll-up vortices are real. They extend certainly too far due to the missing break-up mechanism in a 2D simulation. So, probably in reality they are therefore not detected in the experiments. The overall agreements for shape factor between experiment and simulation is, except for the too big roll-up vortices, very good and certainly much better than for the previous test case. This is due to the lower importance of the kinematical caused transition and the higher importance of the wake turbulence induced transition. The region of low shape factor values is in good agreement with the experiment. Values go down to about 1.8, which is somewhat higher than the level of 1.6 in the experiment . This is a general observation for the T106A simulations. There is also a good distinction between low shape factor values originating from the breakdown to turbulence of the roll-up vortices, and low values originating from wake turbulence induced transition.

Values of momentum thickness are shown in Figure 6.18. The overall level of losses is lower compared to the lower Reynolds case. In between two wakes, the transition appears further upstream due to the higher receptivity of the boundary layer. The agreement between computed and experimental momentum thickness is very good. Although we remark peak values above line B, originating from wake turbulence induced transition, of higher magnitude than in the experiment. This is observed in all T106A cases, and is a result of the TKE tail described in section 6.2.7.

The overall conclusion for the test case is that physical transition mechanisms are qualitatively correctly predicted and that quantitative agreement with the experiments is very good. The agreement is much better than for the lower Reynolds number.

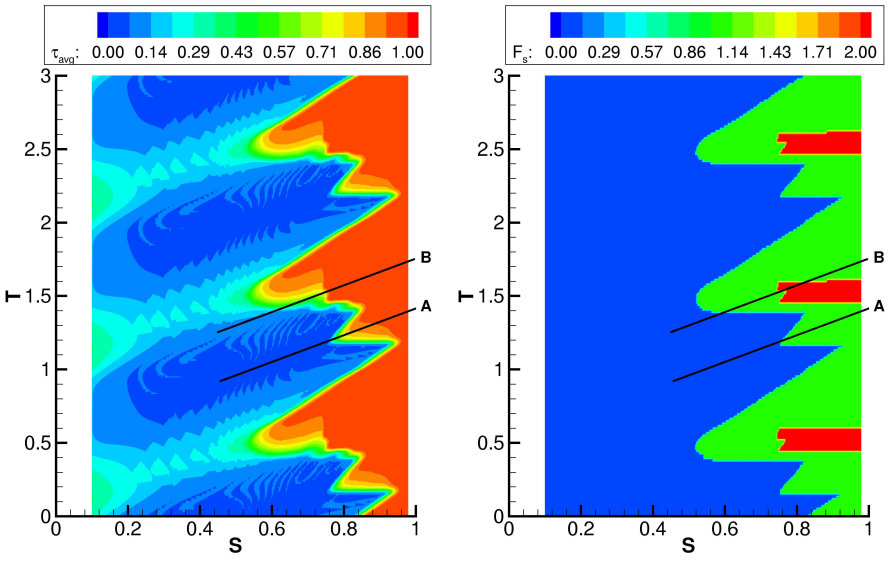

Figure 6.16: T106A (260000, 0.5%); $S - T$ diagram of the boundary layer averaged intermittency (left) and the values of starting function (right).

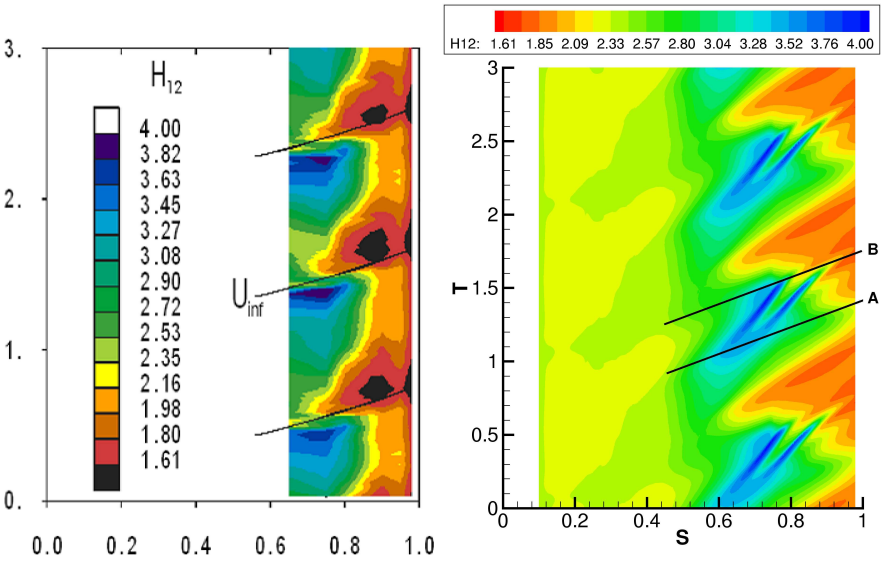

Figure 6.17: T106A (260000, 0.5%); $S-T$ diagram of the experimental (left) and computed (right) shape factor.

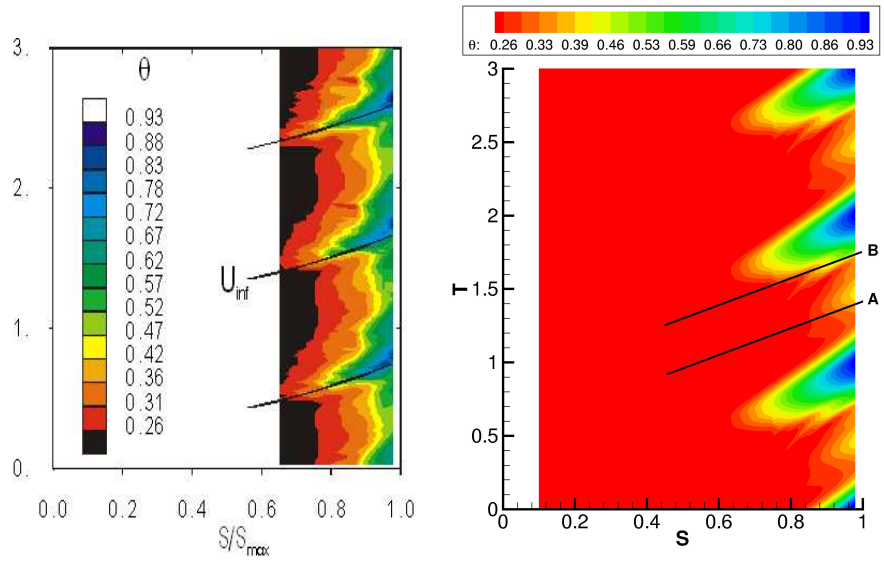

Figure 6.18: T106A (260000, 0.5%); $S-T$ diagram of the experimental (left) and computed (right) momentum thickness.

6.2.7 T106A (Low $Re_{2c} = 160000$, High $Tu = 4\%$)

Contours of turbulent kinetic energy are shown in Figure 6.19. The inlet specifications closely match the experiment, as is the deformation of the wake in the blade passage. In terms of the level of TKE, the overall observation is that production is overestimated in the simulation. In between the wakes (1), the low level of inlet TKE has increased due to diffusion from the wakes, and production. The peak level in the core of the wake (2) is slightly higher than in the experiment. Most important is the high TKE levels trailing behind the simulated wakes over the suction side (3) and (4). In this region, the experimental turbulence decreases rapidly, but in the simulation, the production remains much longer, resulting in somewhat high levels of Tu on the decelerating part of the suction side. This is a deficiency of any isotropic turbulence model, which maximizes turbulence production. The higher levels of Tu between the wakes result in a more upstream prediction of the transition location. It is also responsible for the bigger wake turbulence induced region, as already seen in the low Tu case T106A ($Re_{2c} = 160000$, $Tu = 0.5\%$).

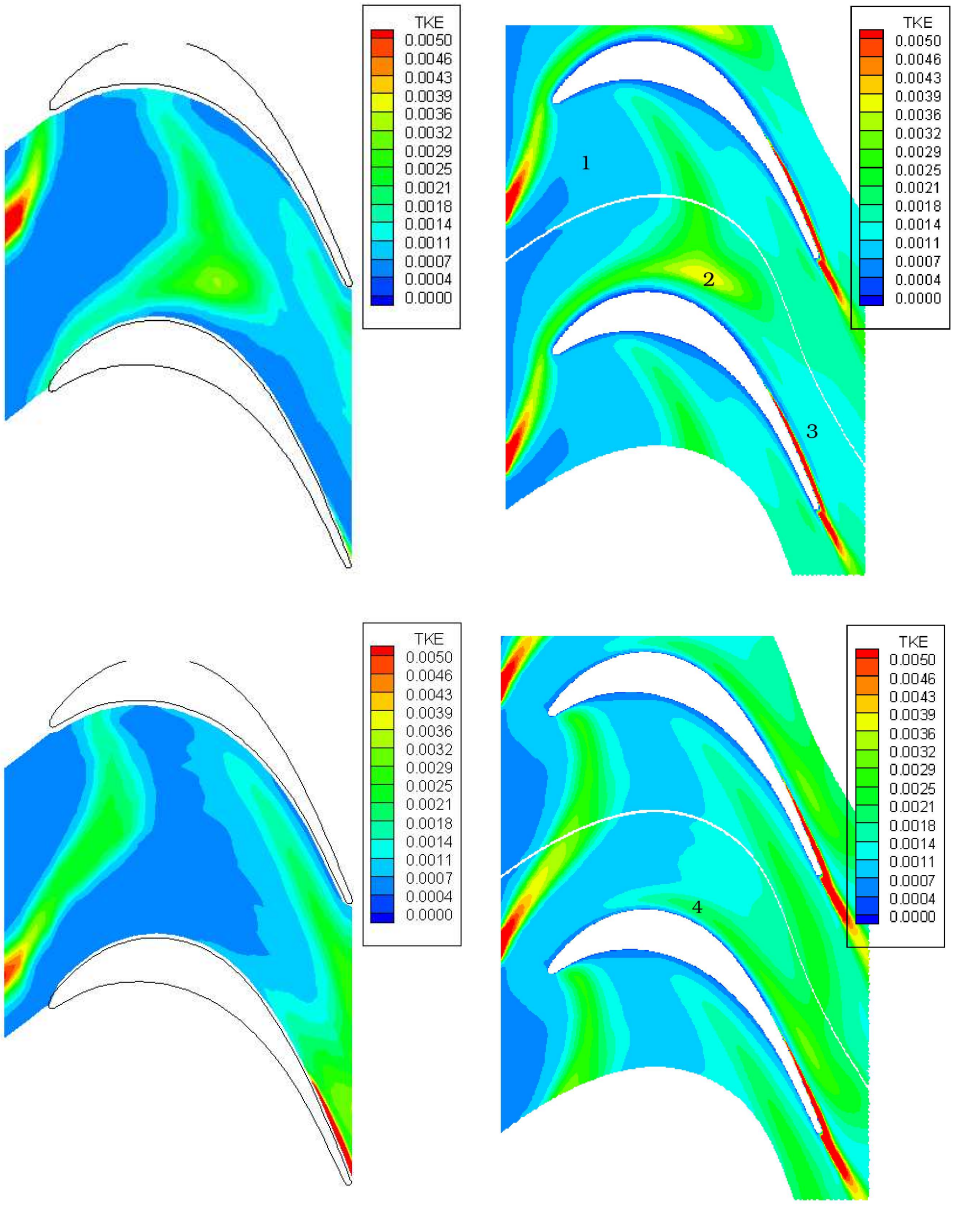

Figure 6.19: T106A (160000, 4%); Contours of turbulence kinetic energy in the blade passage (left: experiment, right: simulation).

Figure 6.20 shows a comparison between the experimental shape factor and the simulation. The overall higher free-stream turbulence intensity, compared to the Tu 0.5% case, moves the transition upstream, as can be seen in values of starting function on Figure 6.21. In between two wakes the transition location shifts to greater values of Re_θ. In Figure 6.22, we see zones of low wall shear stress appear in between the wakes, but there is no laminar boundary layer separation. In the low Tu case, a laminar separation appears before wake impact between $S = 0.68$ and $S = 0.84$. The high turbulence intensity between the wakes starts up transition at about $S = 0.65$ and separation is prevented. Although not separated, the flow is inflexional, and the kinematic wake impact on this profile leads to a small rollup vortex with some associated separation. In between solid lines (A) and (B) in the wall shear stress plot, negative values of wall shear stress are encountered. Only one rollup vortex is seen. The roll-up location at $S = 0.75$ between lines (A) and (B) comes out well in the simulation, and is followed by low values of shape factor. The small roll-up vortex is rapidly destroyed, and creates turbulence in the boundary layer. After line (B), the kinematic wake impact is closely followed by wake turbulence induced transition. Since the wake properties are similar, the extent of the wake turbulence induced transition location is equal to the low Tu case. So again this region is larger than the experimental one.

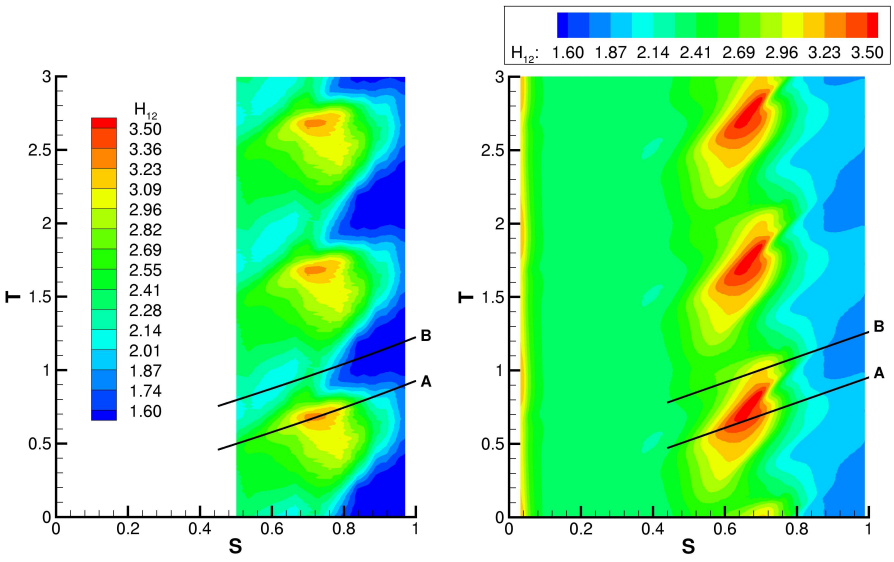

Figure 6.20: T106A (160000, 4%); $S - T$ diagram of the experimental (left) and computed (right) shape factor.

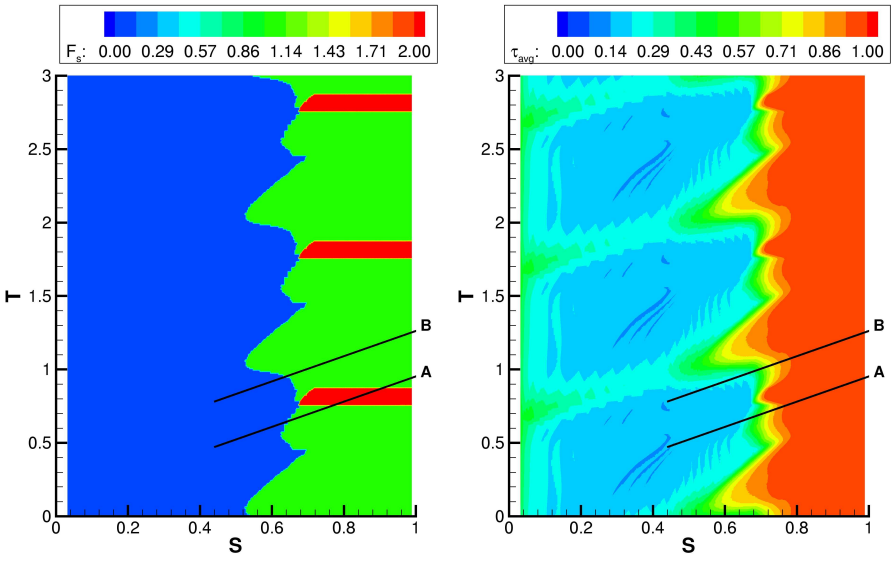

Figure 6.21: T106A (160000, 4%); $S-T$ diagram of the starting function (left) and boundary layer averaged intermittency.

The shear layer roll-up comes out more pronounced than in the experiment. But, it is confirmed by the experimentalists that roll-up occurs during some of the wake passages, but not always [56]. The experimental distribution is thus an average, and an instantaneous shape factor plot during roll-up would resemble more the simulation.

The comparison between the experimental momentum thickness and simulation, in Figure 6.23, again indicates that the turbulence induced transition region, above line B, is simulated too large. The experimental peak between lines A and B confirms the appearance of roll-up. Compared to the low Tu case, the momentum thickness in between the wakes has increased.

Overall, the predictions for the high Tu level are better than for the low Tu level. The differences remain qualitatively similar. The separation or near-separation zones are somewhat too large in the simulation. The turbulent zones come out somewhat too large, with a shape factor not as low as in the experiment.

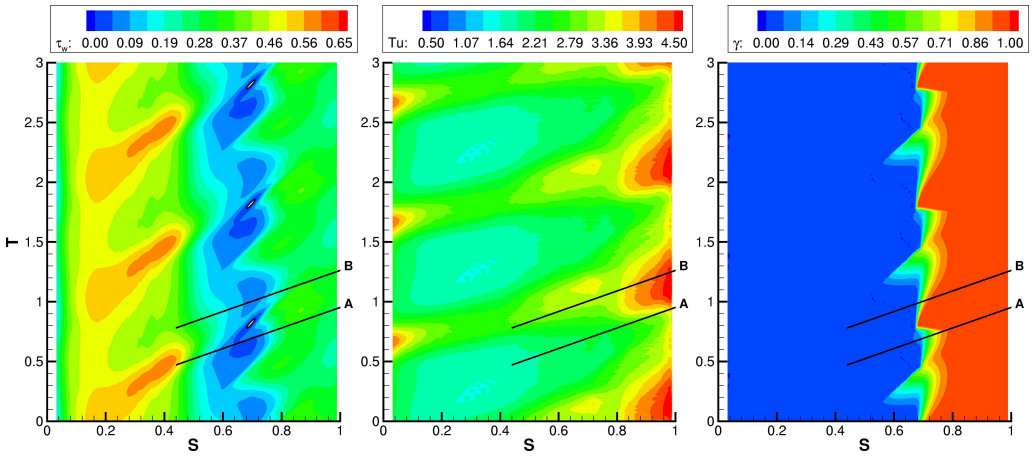

Figure 6.22: T106A (160000, 4%); $S-T$ diagram over the suction side of wall shear stress, free-stream turbulence intensity and wall intermittency factor.

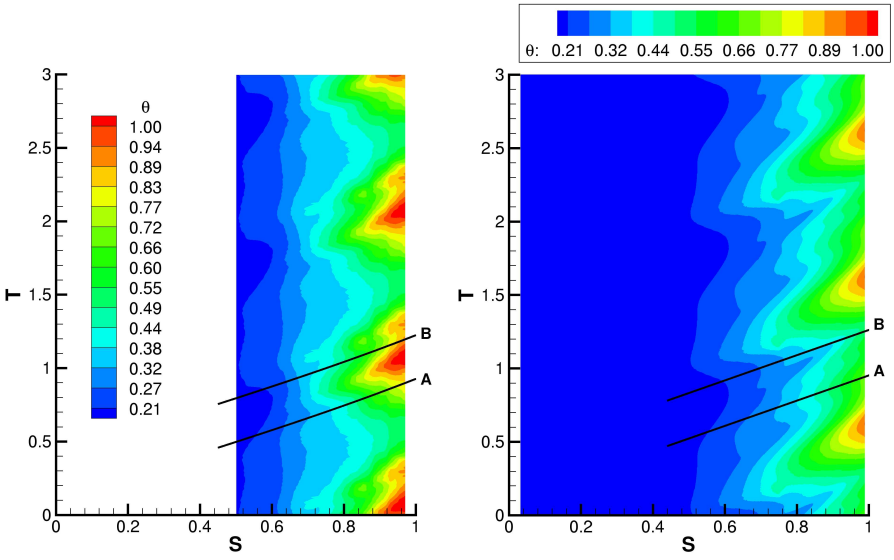

Figure 6.23: T106A (160000, 4%); $S-T$ diagram of the experimental (left) and computed (right) momentum thickness.

6.2.8 Conclusion

The test cases are representative for wake-induced transition with dominance of roll-up vortices (T106A, $Re_{2c} = 160000$, $Tu = 0.5\%$), mixed importance of roll-up breakdown and bypass transition (T106A, $Re_{2c} = 260000$, $Tu = 0.5\%$ and T106A, $Re_{2c} = 160000$, $Tu = 4\%$). The results show deficiencies for the first case, and improve for the second and third case.

The 0.5% Tu test cases used in this paper are not fully representative for real world turbomachinery applications. The background turbulence is too low. The model performs better for the 4% Tu case. As in the experiment, small roll-up activity is seen.

For applications to low-Reynolds number flows, which might become important for future developments in gas turbine engines, the current model cannot be successful. It becomes necessary to formulate the model in a hybrid RANS/LES form, in order to capture large scale vortex breakdown. The extension of the presented model to a hybrid formulation can basically be done without major difficulties and will be the object of further research.

6.3 T106D

This test case was experimentally investigated in the high speed cascade wind tunnel of the Universität der Bundeswehr München by Hilgenfeld, Stadtmüller and Fottner [25]. Additional data were obtained by private communication. The test case has an extreme loading which results in a separation bubble in the deceleration region. This is not desired in real engine conditions. Even if the case is not industrially applicable, the model must be able to reproduce this effect, and herewith warn a designer that a configuration is over-loaded.

6.3.1 Geometry

The cascade has the same LPT rotor blade as T106A, but with increased pitch-to-chord ratio. Bars are moving parallel to the inlet plane $70mm$ ($0.814c_{ax}$) upstream of the leading edge. The basic parameters are listed in Table 6.3. This is 'operating point 1' of the test case documentation. The computational grid consists of a T106 profile with pitchwise periodic boundary conditions. Again, the moving bar system is not included in the computation. Instead, a moving wake profile is used as inlet condition. The inlet of the computational domain is located between the bars and the leading edge at $60mm$ axially upstream of the leading edge. The inlet plane is sufficiently far from the cascade so that potential effects are small at this location. No precalculation of the potential effect is done here. The grid consists of 107000 cells. The y^+ value in the first grid point in wall vicinity is below 0.4. A stretching factor of 1.05 has been applied perpendicular to the wall such that the viscous region of the boundary layer ($y^+ < 50$) contains more than 30 cells. Per pitchwise traverse 3×800 time steps are used. This high accuracy is necessary to properly simulate the unsteady movement of the wake.

6.3.2 Inlet conditions

The bar pitch had to be reduced to $35mm$ to obtain a multiple of the blade pitch in the calculation. The deviation of the inlet flow due to the force by the bars is much higher than in the previous test case. The inlet angle had to be increased by 4.5° to 42.2° in order to get good comparison with the experimental pressure distribution, shown in Figure 6.24. The T106D test case, unlike the T106A test case, has a leading edge separation bubble due

blade chord	c	$100mm$
axial blade chord	c_{ax}	$85.967mm$
pitch to chord ratio	g/c	1.05
Reynolds number	Re_{2c}	2.0×10^5
exit Mach number	Ma_{2th}	0.401
undisturbed inlet flow angle	α_1	$-37.7°$
bar diameter	d	$2.05mm$
bar pitch/ cascade pitch		$40mm/105mm$
axial distance bars to LE		$70mm$
flow coefficient	U_{1x}/U_b	3.09
Strouhal number		0.84
free-stream turbulence intensity		$< 1\%$
turbulence level in the bar wake		7%

Table 6.3: T106D cascade.

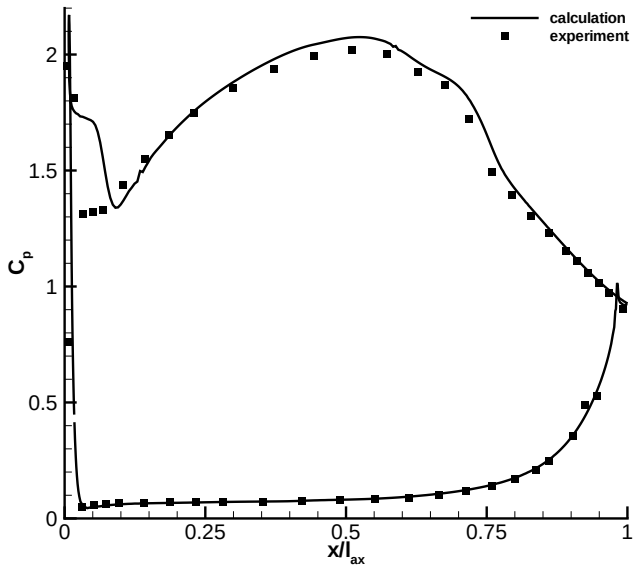

Figure 6.24: T106D; Time-averaged pressure distribution.

to the higher loading. This makes the case extremely sensitive to inlet angle effects. So, the inlet angle has to be set here so that the mean size of the separation bubble at the rear part of the suction side is correct. A slightly different inlet angle (41.7° or 42.7°) also gives good agreement for the pressure distribution, but has an important influence on the leading edge separation bubble. The change of the leading edge separation bubble alters the boundary layer integral parameters in the acceleration zone of the suction side, which influences significantly the Mayle transition criterion, resulting in significant changes in predicted separation bubble size in the deceleration zone of the suction side.

Due to the small height of the blade ($176mm$), the flow is three-dimensional. Corner vortices are present at the end walls in the decelerating part of the suction side. The pressure side remains relatively unaffected. This results in a measured value of the axial velocity density ratio AVDR of 0.8718 in the mid-plane of the cascade (from private communication). The effect of the global acceleration in the mid-plane due to flow obstruction by the corner vortices has been incorporated in the calculation by means of a source term in the x- and y- momentum equations. This source term is a constant multiplied by the velocity component, and is only active in the rear half part of the decelerating channel between two blades. Its value has been tuned such that the source term prevents the trailing edge from separating. Compared to experiments, the computed trailing edge shape factor is higher. This indicates that the applied acceleration force is less strong than the equivalent force of the experimental 3D effects. It was, however, a deliberate choice to keep the acceleration force as low as possible.

6.3.3 T106D (Low $Re_{2c} = 200000$)

The increased loading (about 30% higher than for T106A) causes a separation bubble at about $0.64\, x/l_{ax}$. In steady flow (free-stream $Tu = 2.5\%$), a large separation bubble appears. In unsteady flow, the separation bubble size is reduced due to the wakes. A leading edge separation bubble is also observed at the front part suction side. The flow reattaches there due to the strong acceleration. In the simulation, the transition mechanisms have been deactivated over this leading edge separation.

Figure 6.25 shows the numerically obtained wall shear stress, free-stream turbulence intensity and starting function. The transition is always of quasi-steady type. In the wake turbulence induced region (between lines B and

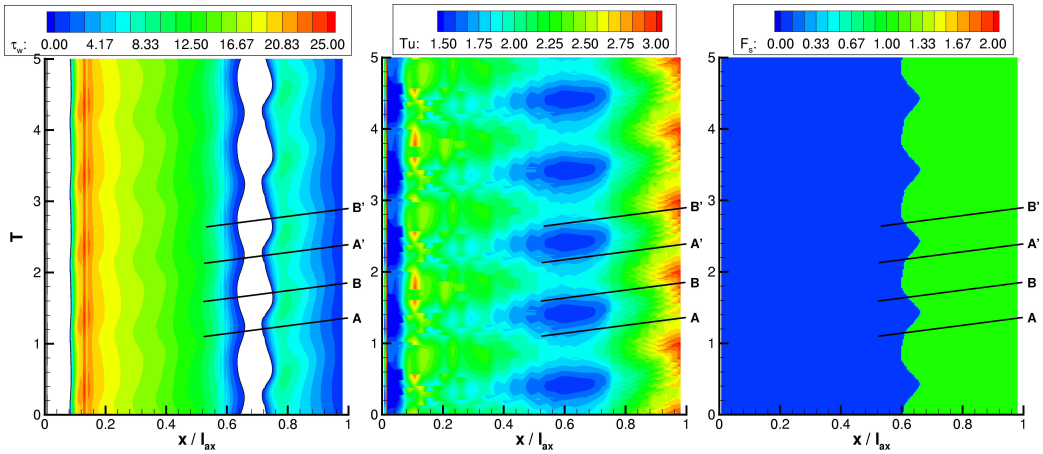

Figure 6.25: T106D; $S-T$ diagram over the suction side of the wall shear stress, the free-stream turbulence intensity and the values of starting function.

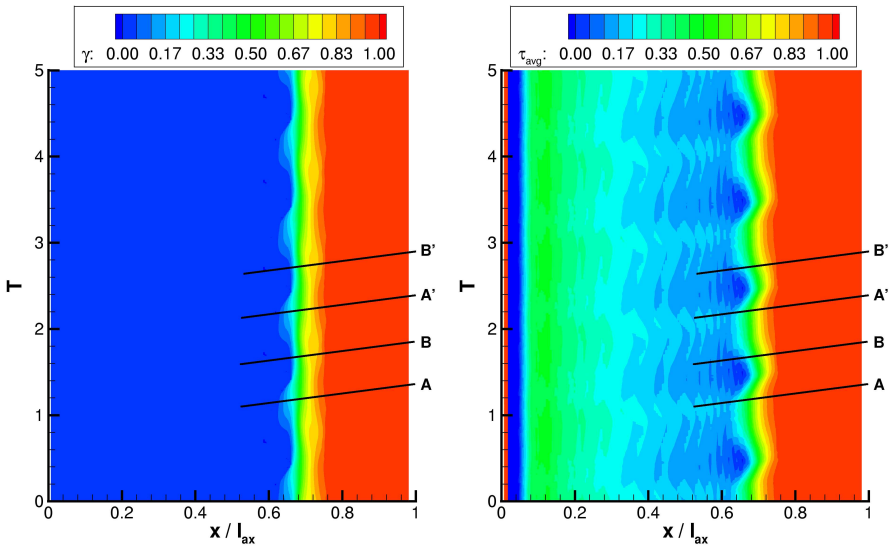

Figure 6.26: T106D; $S-T$ diagram of the wall intermittency factor (left) and the averaged intermittency factor (right).

A'), the start of transition is located before the separation point (at about $0.60\, x/l_{ax}$) in the deceleration zone. At start of the deceleration phase, there is a competition between transition due to spot growth, and flow separation. In between two wakes, the transition point moves somewhat downstream of the separation point, and transition over a separation bubble is detected. Due to wake turbulence, the transition location moves forward, but the growth rate of the spots is low in the weak adverse pressure part of the suction side. So, changes in intermittency are subtle, as shown in Figure 6.26, but the effect on the wall shear stress is stronger.

The high number of wakes per blade pitch has a clear influence on the $S-T$ plot of averaged intermittency. The suction side is almost constantly influenced by the wakes, so values of τ_{avg} remain high.

Since, compared to the T106A case, the distance between bars and profiles is large, the kinematic impact of the wake is weaker. Roll-up of the separation bubble is not observed. The wake periodically changes the deceleration rate of the rear part suction side. Under the acceleration (A), the deceleration is reduced, and so is the bubble size. The deceleration (B) due to the wake kinematics increases the deceleration, and this enhances the tendency to separate, resulting in a larger bubble size. This is captured very well in the simulation.

The overall extent of the separation matches well the experiment. This can be seen by the averaged pressure distribution and the $S-T$ plot of shape factor shown in Figure 6.27. It is repeated that the size of the separation bubble is very dependent on the inlet angle and its effect on the leading edge separation bubble. This is a consequence of the delicate physical phenomena acting in this test case. It highlights the care that has to be taken in reproducing the exact experimental setup. However, if these are reproduced well, the model is capable of reproducing the physics. The predicted losses are in good agreement with the experiment, as visible on the momentum thickness plot shown in Figure 6.28.

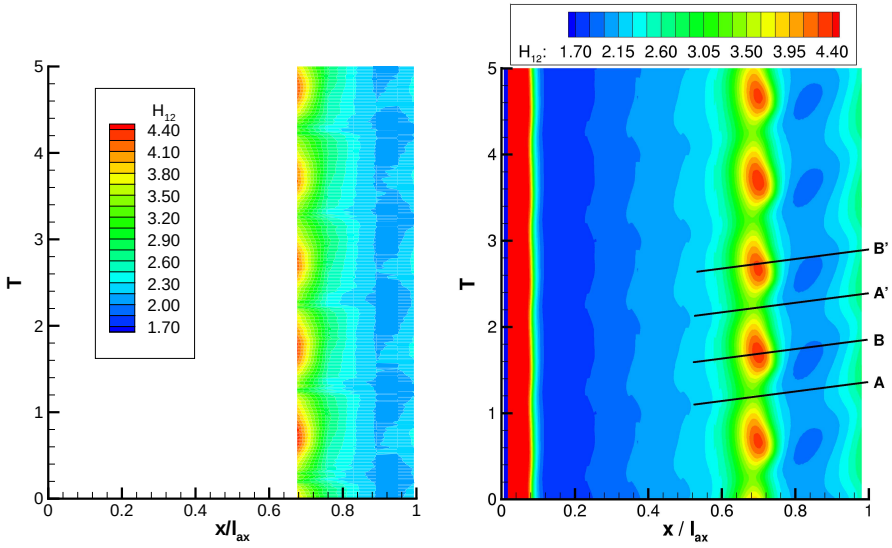

Figure 6.27: T106D; $S-T$ diagram of the experimental (left) and computed (right) shape factor.

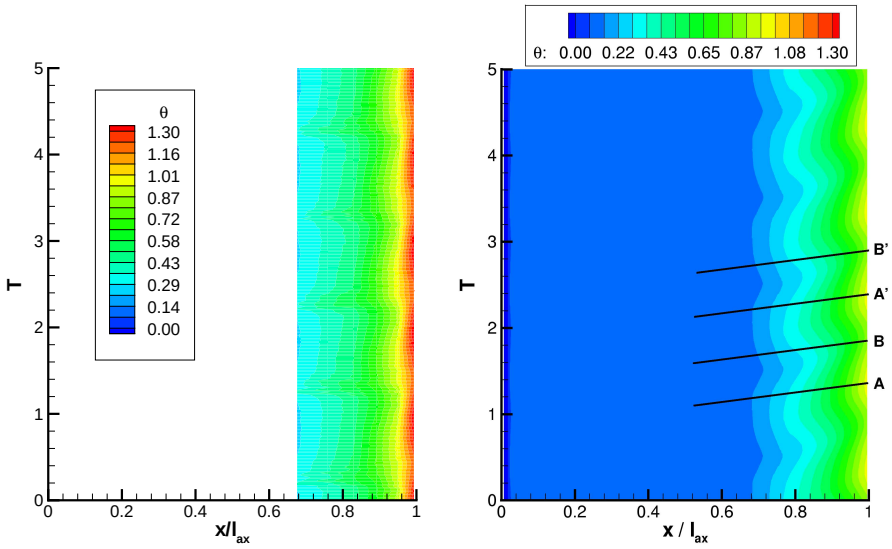

Figure 6.28: T106D; $S-T$ diagram of the experimental (left) and computed (right) momentum thickness.

6.3.4 Conclusion

The overall conclusion for the T106D test case is that predictions are very good. The basic reason is that due to the larger number of wakes per pitch and the larger distance between the bars and the profiles, compared to T106A test cases, the flow is almost steady with an almost constant and high turbulence level at the leading edge plane of the cascade ($Tu \sim 2.5\%$). The transition is of bypass type. Earlier studies, with a slightly different transition model, were done by the authors for steady *attached* bypass flows [41, 42]. The results for these steady flows were generally very good. We come here to the same conclusion for quasi-steady bypass transition in *separated* flow. For these steady and quasi-steady flows, the results are critically dependent on the quality of the empirical criteria for prediction of start and growth rate of transition. The remarkable observation is that these criteria which have been determined on rather simple flat plate flows remain valid for turbomachinery bladings, provided that they are used locally, i.e. made dependent on the local free-stream turbulence level, instead of the incoming turbulence level in the simple flat plate flows.

6.4 N3-60

The quality of the transition model is further illustrated on the N3-60 test profile using experimental results of Piotrowski, Zarzycki and Elsner [40, 96] for attached flow transition. Additional data were obtained by private communication on results obtained in the EC-project UTAT. This test case is used here because of the relatively high Reynolds number. Transition is of quasi bypass type.

6.4.1 Geometry

The N3-60 profile is experimentally measured in the open-circuit wind tunnel equipped with a disturbance generator at the Institute of Thermal Machinery TU of Czestochowa. The profile N3-60 is an industrial one and it was used as a stator vane of the high-pressure part of TK-200 turbine produced by a Polish manufacturer (formerly ZAMECH now ALSTOM). The main geometrical parameters of the cascade are listed in Table 6.4. Bars are moving parallel to the inlet plane $70mm$ ($0.3437c_{ax}$) upstream of the leading edge. Instead of including the moving bar system in the computation, a moving wake profile is used as inlet condition. The inlet of the computational domain is located between the bars and the leading edge at $0.21c_{ax}$ upstream of the leading edge. The grid consists of 150700 cells. The y^+ value in the first grid point in wall vicinity is below 0.35. Per pitch-wise traverse, 800 time steps are used. This high accuracy is necessary to properly simulate the unsteady movement of the wake.

blade chord	c	$300mm$
axial blade chord	c_{ax}	$203.65mm$
pitch to chord ratio	g/c	0.8
Reynolds number	Re_{2c}	0.6×10^6
inlet flow angle		0°
bar diameter	d	$4mm$
bar pitch	s_b	$204mm$
axial distance bars to LE		$0.35c_{ax}$
flow coefficient	U_{1x}/U_b	0.68
free-stream turbulence intensity		0.4% and 4%

Table 6.4: Geometrical characteristics of N3-60 test cases.

6.4.2 Inlet conditions

The bar pitch s_b had to be increased to $240mm$ to obtain a multiple of the blade pitch in the calculation. We have chosen to keep the flow coefficient constant. This means that the bar speed is left constant at $U_b = 12m/s$. The increase in bar pitch results thus in a decrease in bar frequency f_b, from $59Hz$ to $50Hz$. And consequently the reduced frequency F also drops, from 0.604 to 0.512. The **reduced frequency** sets the ratio of the convection time scale to the wake passing time scale. The higher the reduced frequency, the greater the number of wake segments in a blade passage at any one time. So the *unsteadiness* of the flow in the wake passage increases with increasing reduced frequency. The reduced frequency can be defined as

$$F = f_b \frac{C}{U_2} = \frac{U_b}{s_b} \frac{C}{U_2} \tag{6.6}$$

In the simulation, the time between two wake passages has somewhat increased compared to experiment. For the T106A case at $Re_{2c} = 160000$, the bar passing frequency is $40.28Hz$, which leads to a reduced frequency $F = 0.685$. Compared to the T106A case, the time between two wake impacts for N3-60 is longer.

The inlet angle had to be increased to 5° in order to get good comparison with the experimental pressure distribution. The difference in the inlet flow angle, is probably due to airflow leakage through the slots located upstream of the blade, where the moving bars pass. To incorporate the potential effect of the profile on the inlet plane velocity, a fully-turbulent steady calculation with inlet far upstream of the leading edge has been performed, as shown in Figure 6.29. The velocity distribution (magnitude and angle) on the inlet plane is used as inlet velocity for all calculations. For unsteady calculations, the wake velocity deficit is added to this velocity distribution profile.

Verification of the inlet conditions is achieved by means of the time averaged pressure distribution over the profile. The pressure coefficient distribution is shown in Figure 6.30. At $S = 0.55$, the deceleration is computed stronger than observed in the experiment. This may be the result of a sudden change in curvature of the profile. The tested profile is polished and probably smoother than the profile dataset. Downstream, the pressure distribution fits the experimental data properly. The wake profiles applied at the inlet were taken from experiments. Turbulent kinetic energy in the wake and the background dissipation has been used to adjust the wake evolution to the experimental one.

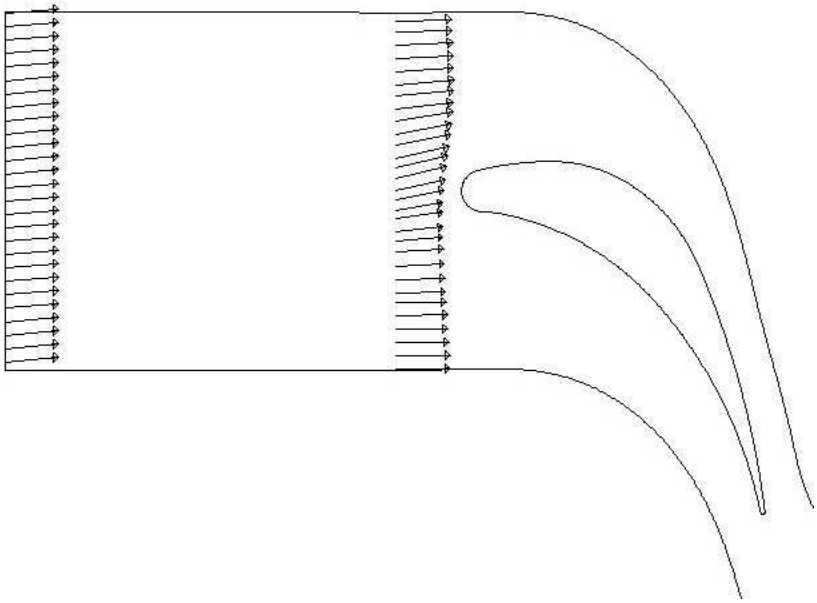

Figure 6.29: Potential influence on the inlet plane for N3-60.

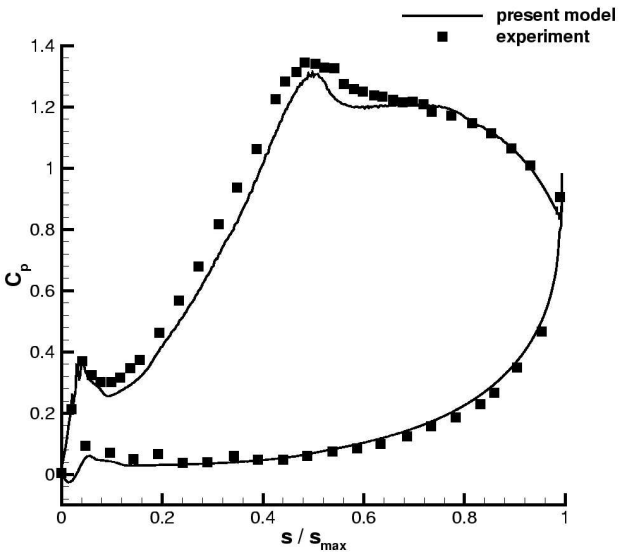

Figure 6.30: Pressure coefficient distribution for N3-60.

6.4.3 N3-60 (High $Re_{2c} = 600000$, Low $Tu = 0.4\%$)

Without the wakes, the overall turbulence intensity is much below 1%. Attached bypass transition is not observed, and the flow goes into laminar separation near the trailing edge of the suction side, as shown on Figure 6.31. Steady transition over a separation bubble is activated. The reattachment point of this separation bubble is close to the trailing edge. In the experiment, the separation is not observed, and may be prevented by natural transition taking place upstream of the separation. Figure 6.32 shows the shape factor evolution. After $S = 0.9$, the experimental shape factor values start to decrease again, so the separation level of $H = 3.5$ is not achieved. In the computation, separation is observed, and the shape factor goes up to 4.5.

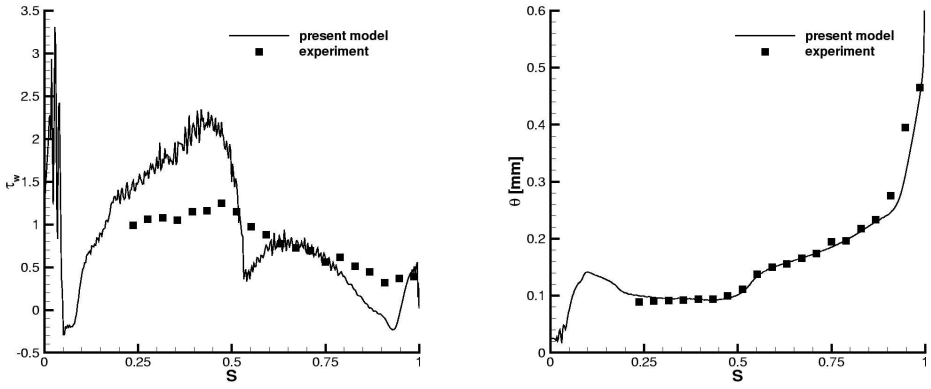

Figure 6.31: Wall shear stress and momentum thickness evolution for N3-60, $Tu = 0.4\%$, steady flow.

The sudden sharp deceleration at $S = 0.55$ observed in the pressure distribution is reflected in a low wall shear stress value at the same location. The strong deceleration and the resulting strong increase in momentum thickness Reynolds number is a key point in the suction side evolution. Under wake passage, the higher turbulence intensity starts transition at that location, more of less independent of the turbulence intensity level. In between two wakes, the boundary layer relaxes toward the steady result.

With unsteady wake passage, wake turbulence induced transition starts at about $S = 0.55$, and is completed at about $S = 0.75$. Figure 6.33 shows the experimental ($0.3mm$ from the wall) and simulated intermittency $S - T$ plots for the suction side. The simulated intermittency is shown as an

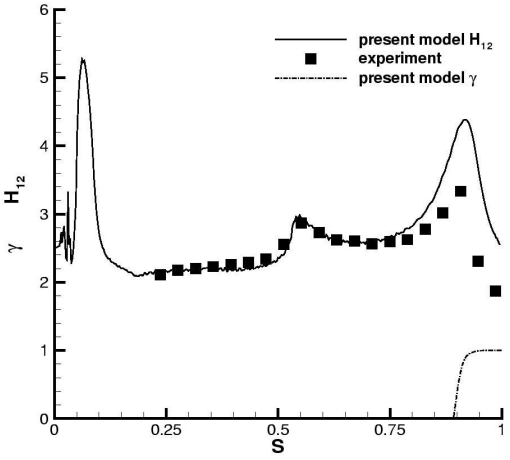

Figure 6.32: Shape factor and intermittency evolution for N3-60, $Tu = 0.4\%$, steady flow.

average over the boundary layer, and at the wall. The solid lines indicate the location of maximal acceleration (A) and deceleration (B) due to wake kinematic effect. Under the wake passage, the agreement with the experiment is good. After wake passage, the turbulence intensity level decreases, and the transition location moves downstream. Immediately after wake passage, for some time ($T = 1 \rightarrow 1.1$), transition is not detected, as seen in the plot of starting function F_s in Figure 6.34. This is due to the becalming effect. The velocity profile is still turbulent like, and can withstand the deceleration for some time. However, at $T = 1.1$, the boundary layer starts to separate near the trailing edge, this can be seen in the wall shear sress in Figure 6.34. The separation bubble grows with time. Quasi steady transition over a separation bubble is located some distance downstream of the separation point, as seen in the values of starting function in Figure 6.34.

The experiment shows natural transition starting at $S = 0.9$ in between the wakes. In the simulation, natural transition is not implemented. The simulation does not incorporate natural transition because this is not present in industrial applications. Also in the experiment, a small separation bubble appears. High levels of shape factor are observed just before wake impact, indicating separation. This can be seen in Figure 6.35 at $S = 0.85$ and $T = 1.3$, which shows the experimental and computed shape factor. Natural transition takes place after wake passage, and limits the growth of the separation bub-

ble. The trailing edge boundary layer is always attached and transitional in between the wakes. Further, in the simulation, the reduced frequency is lower than in the eperiment. So numerically, the separation bubble has more time to re-establish.

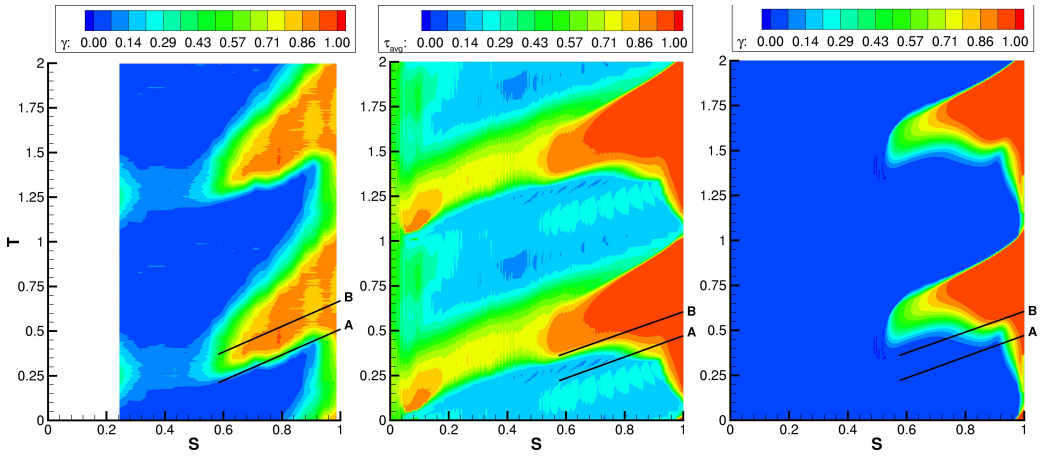

Figure 6.33: S-T plot of experimental intermittency (left) and calculated averaged- (middle) and wall- intermittency (right) for N3-60, $Tu = 0.4\%$.

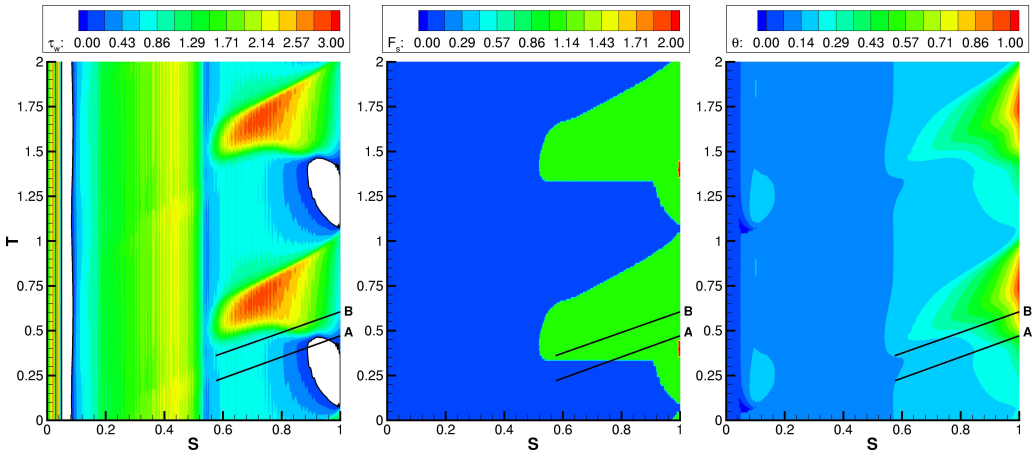

Figure 6.34: S-T plot of wall shear stress, values of starting function and momentum thickness for N3-60, $Tu = 0.4\%$.

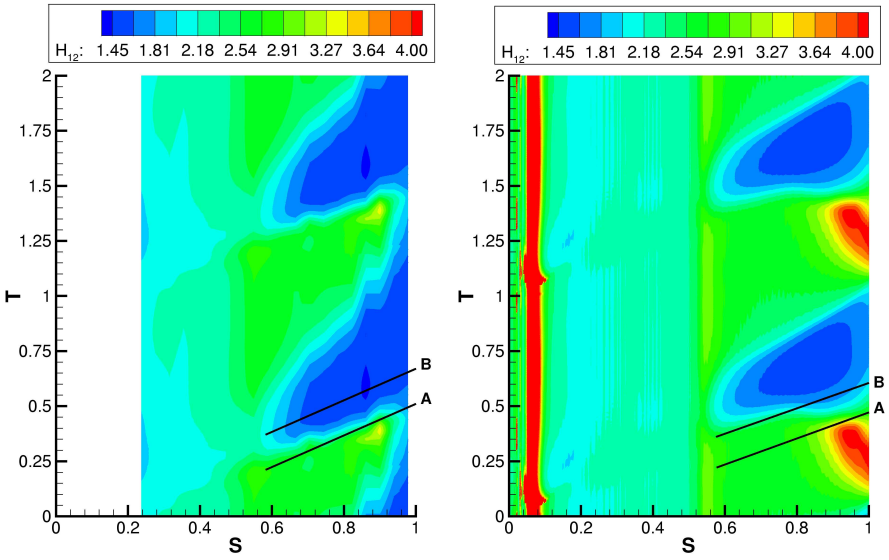

Figure 6.35: S-T plot of experimental (left) and calculated (right) shape factor for N3-60, $Tu = 0.4\%$.

6.4.4 N3-60 (High $Re_{2c} = 600000$, High $Tu = 4\%$)

In the steady case, the high inlet turbulence intensity decays to a level of 1.1% in the deceleration part of the suction side, see Figure 6.36. With this level, transition is activated halfway the deceleration part of the suction side. The shape factor distribution, given in Figure 6.37, indicates that transition is predicted somewhat too far in the simulation.

Levels of TKE in the blade passage are compared with experiments in Figure 6.38. Again the observation is that in the simulation, the tail of the wake (A) has elevated TKE. Also shown are perturbation vectors. Clearly visible are two counter rotating vortices, and the jet pointing toward the suction side surface.

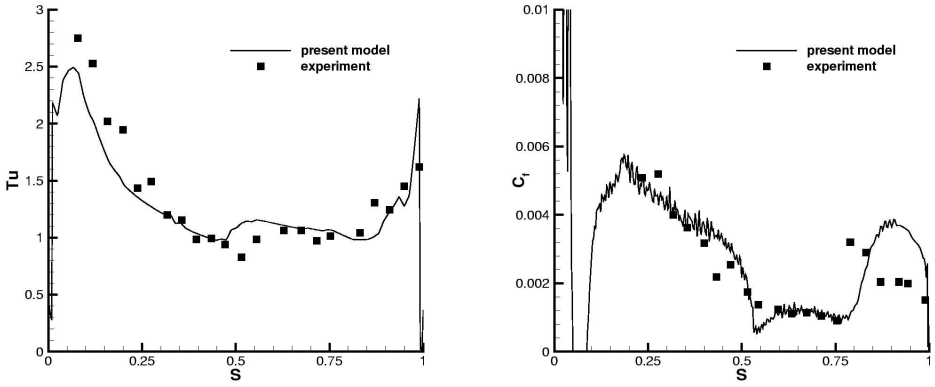

Figure 6.36: Turbulence intensity and skin friction evolution for N3-60, $Tu = 4\%$, steady flow.

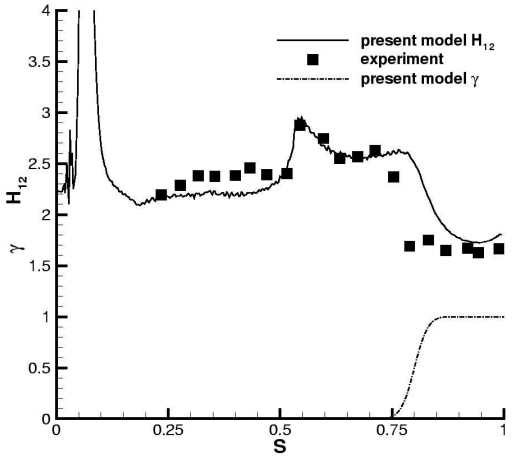

Figure 6.37: Shape factor and intermittency evolution for N3-60, $Tu = 4\%$, steady flow.

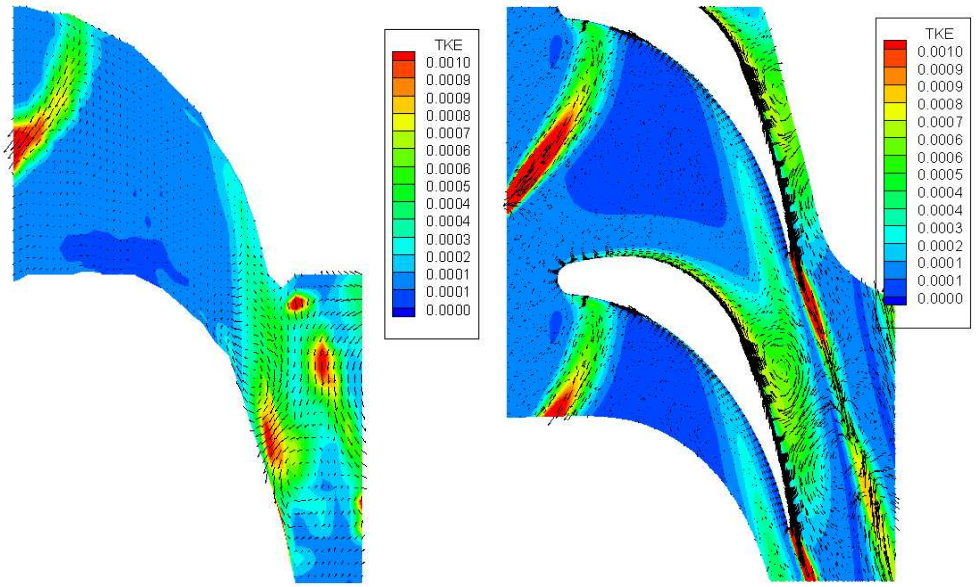

Figure 6.38: Contours of turbulent kinetic energy and perturbation vector in the blade passage for N3-60, $Tu = 4\%$ (left: experiment, right: simulation).

The wake properties of the low Tu case are similar to the high Tu case, but the background turbulence is different, as shown on the $S-T$ plot of Tu in Figure 6.39. So in the unsteady case, the major difference with the low Tu case is in the region between the wakes. The background Tu is higher, and activates transition at $S = 0.75$.

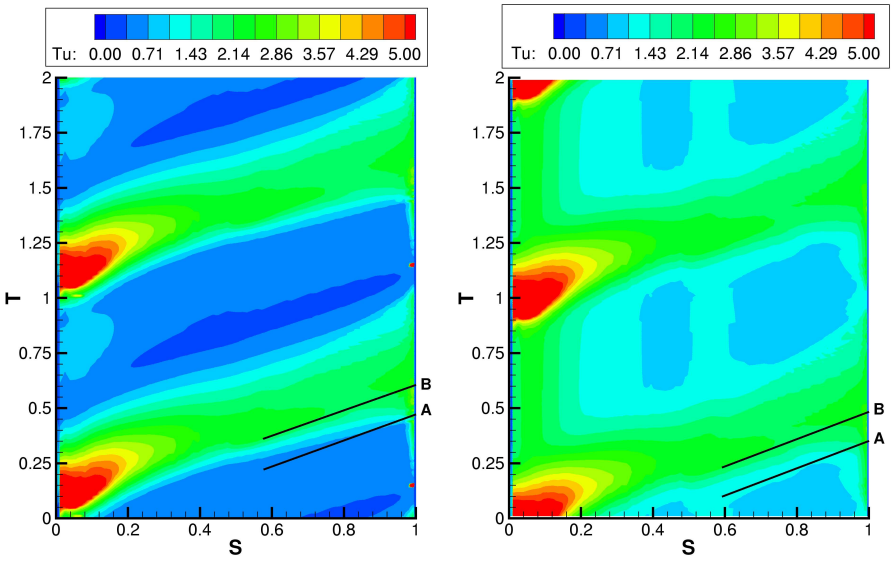

Figure 6.39: S-T plot of turbulence intensity for N3-60, $Tu = 0.4\%$ (left), and $Tu = 4\%$ (right).

With unsteady wake passage, the transition under the wake is qualitatively similar to the low Tu case. After wake passage, the calming effect shifts the transition location much downstream. The transition location is shown in the plot of starting function in Figure 6.40. The intermittency plot is given in Figure 6.41. The Tu decreases, but the boundary layer state remains turbulent like, so the Mayle criterion shifts the transition location downstream. The relaxation of the boundary layer under the adverse pressure gradient from $S = 0.55$ to $S = 1$ leads to increasing levels of momentum thickness (-Reynolds number) until at some point ($S = 0.9$, $T = 0.95$) the Mayle criterion is activated, and transition in between the wakes is started. The boundary layer upstream of that location ($S = 0.9$) is still laminar but becalmed, and subject to deceleration, which makes the momentum thickness increase and the transition location shift even further upstream ($S = 0.75$). So after the becalming effect, the boundary layer evolves in between the wakes toward the steady result. When comparing the contour plots of TKE for the cases N3-60 and T106A low Re, see Figures 6.38 and 6.19, already visually the

wakes appear to be further apart in the N3-60 case. The reduced frequency confirms this impression, and explains why the N3-60 evolves more toward a steady result in between the wakes. This is especially the case in the simulation where the reduced frequency is even lower than the experimental one. Another way to say this, is that the wakes pass quicker. Consequently, the erroneous tail with high levels of TKE marked with A in Figure 6.38 has a reduced importance in the overall prediction.

The becalming effect is also visible in the shape factor plot in Figure 6.42. The high shape factor values at $S = 0.55$ are a result of the sharp deceleration in that region. The experimental data plot is rather coarse, therefore this region is bigger. But the experimental profile is also smoother, and so is the deceleration. In the experiment, the becalming is visible up to the trailing edge. At $T = 1$, the lowest contour level of shape factor values disappears shortly. Somewhat later is reappears downstream of $S = 0.96$. Under wake passage, the location moves to $S = 0.82$. In the simulated shape factor values, the becalming effect is somewhat stronger.

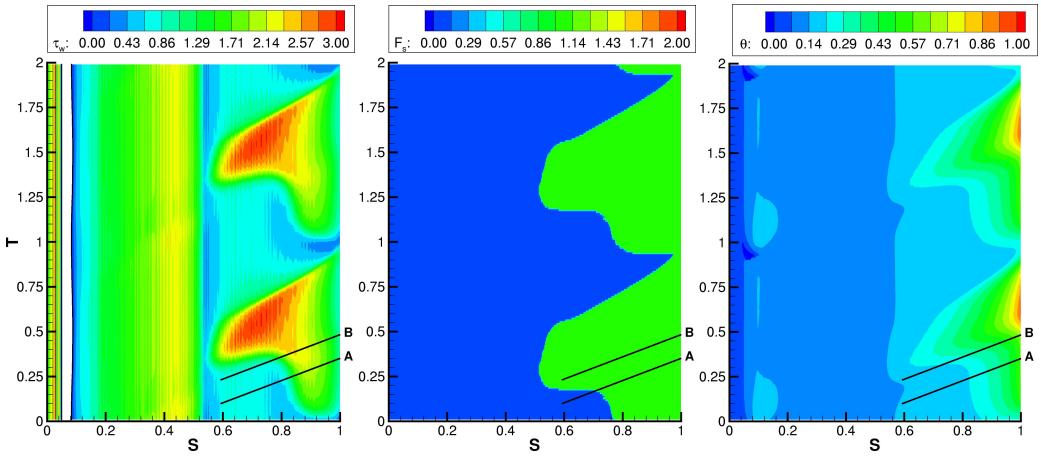

Figure 6.40: S-T plot of wall shear stress, values of starting function and momentum thickness for N3-60, $Tu = 4\%$.

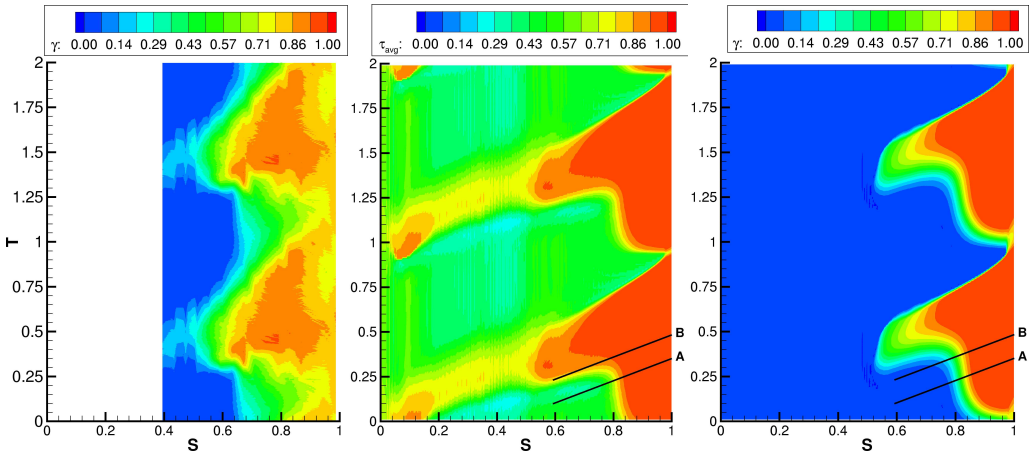

Figure 6.41: S-T plot of experimental- (left) and calculated averaged- (middle) wall- intermittency (right) for N3-60, $Tu = 4\%$.

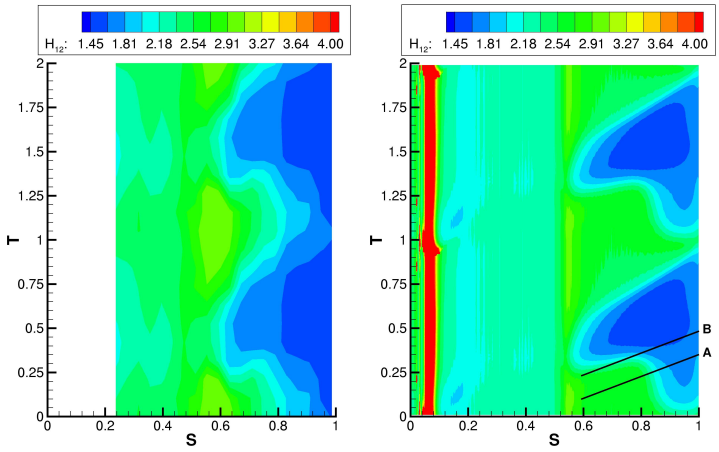

Figure 6.42: S-T plot of experimental (left) and calculated (right) shape factor for N3-60, $Tu = 4\%$.

6.4.5 Conclusion

The N3-60 test cases ($Re_{2c} = 600000$, $Tu = 0.4\%$ and $Tu = 4\%$) are representative for wake-induced transition of bypass type. The computational results for these cases are very good, except for the detection of the natural transition for the low background turbulence ($Tu = 0.4\%$). The natural transition is not seen in the simulation because no model for it is implemented.

Chapter 7

Conclusion and future work

A transition model for wake-induced transition based on dynamic description of intermittency was presented. The model was derived from the one equation model of Steelant and Dick [76], which acts as a basis for a conditional averaging between the laminar an the turbulent parts in the transitional region. Although being interesting from a physical viewpoint, the need to calculate both a laminar and a turbulent flow field hinders its applicability in industry. The conditional averaging was replaced here by Reynolds averaging. Furthermore, the intermittency equation was decomposed in two components to be able to account for the difference in time and length scale of the free stream compared to the boundary layer. The approach is proved to be successful. The model requires empirical input for detection of bypass transition in attached and separated state. For start and growth rate of bypass transition, the Mayle correlations have been used. The present study confirms the general applicability of these correlations. For start of transition due to breakdown of roll-up vortices caused by the kinematic action of the wake impact on a separation bubble, a rather heuristic criterion of simultaneous occurrence of separation and wake turbulence results in a realistic description of the intermittency.

The model presented in this thesis is the first model shown able to cover the broad range of physical transition mechanisms acting in LP turbines.

It is reported that turbulence build-up due to the breakdown of roll-up vortices cannot be described accurately with the present 2D RANS calculations. So, for flows where transition is dominated by breakdown of large scale vortices, one has to be careful with the present model. These are typically

flows with low Reynolds numbers and lower background turbulence level, and separated, or nearly separated, flows. Zhang et al. [97] experimentally observed that roll-up causes an inadmissible amount of loss. In their proposal for a new ultra-high-lift profile, they take particular care in avoiding roll-up of the separation bubble. The designer should be warned by an appearance of roll-up and must try to avoid it, even if the simulation doesn't reproduce the associated high loss.

The transition model works properly, but the production of turbulence in the wake passage by the turbulence model is too high. Including the effects of anisotropy in the turbulence model would improve the simulation results. This is resolved in a hybrid RANS/LES simulation.

The study further shows that the results of the simulations are very sensitive to inflow conditions and to the quality of the numerical method. For test cases with very high loading and low free-stream turbulence intensity, as used here, subtle changes in operating conditions can alter the transition type significantly. Further it is necessarily to have a very accurate representation of the passing wakes. This sensitivity has purely physical reasons. The consequence is that practical transition analysis is always very delicate.

We conclude that further improvement can be obtained by improving the turbulence model rather than the transition model. The deficiencies of the turbulence model observed in the considered cases can be solved by going toward a hybrid RANS/LES model. This is not necessary a big step since in this RANS method, the kinematic wake impact on a separation bubble is sufficiently resolved. A LES simulation by Magagnato [44] on a T106A test case without wakes shows that the small scale shear layer instability of a separation bubble can be seen. A LES simulation by Sarkar [63] on the same profile with incoming wakes shows that the transitional phenomena are well reproduced.

Since the RANS/LES model is able to capture separation related transition, only a model for detection of bypass transition should be added. The model should be local to allow parallel computation. The mechanism for detection of bypass transition can be based on the model of Walters and Leylek [88], where pre-transitional boundary layer turbulence is subdivided into a large scale part and a small scale part. The small scale part acts as normal turbulence. The large scale part is constantly stimulated by the free-stream fluctuations. We are confident that resolving the free-stream eddies can contribute to the accuracy of the representation of the low scale part of

the pre-transitional fluctuations. Some threshold value should then enable the breakdown of the large scale fluctuations. This procedure is local, so it doesn't object parallel computation.

Bibliography

[1] http://cfd.me.umist.ac.uk/ercoftac/.

[2] http://transition.imse.unige.it/cases/goa.

[3] B. Abu-Ghannam and R. Shaw. Natural transition of boundary layers-the effects of turbulence, pressure gradient and flow history. *J. Mech. Eng. Sci.*, 22(5):213–228, 1980.

[4] J. S. Addison and H. P. Hodson. Unsteady transition in an axial-flow turbine: Part 1-measurements on the turbine rotor. *J. of Turbomachinery*, 112:206–214, 1990.

[5] J. S. Addison and H. P. Hodson. Unsteady transition in an axial-flow turbine: Part 2-cascade measurements and modeling. *J. of Turbomachinery*, 112:215–221, 1990.

[6] J. S. Addison and H. P. Hodson. Modelling of unsteady transitional boundary layers. *J. of Turbomachinery*, 114(3):580–589, 1992.

[7] T. Arts and M. Lambert de Rouvroit. Aero-thermal investigation of a highly loaded transonic linear turbine guide vane cascade. technical note 174, von Karman Institute, Belgium, 1990.

[8] R. J. Boyle and F. F. Simon. Mach number effects on turbine blade transition length prediction. *J. of Turbomachinery*, 121(4):694–702, 1999.

[9] P. Bradshaw. Turbulence: The chief outstanding difficulty of our subject. *Exp. in Fluids*, 13:203–216, 1994.

[10] L. Brandt, P. Schlatter, and D. S. Henningson. Transition in boundary layers subjected to free-stream turbulence. *J. Fluid. Mech.*, 517:167–198, 2004.

[11] S. Byggstøyl and W. Kollmann. Closure model for intermittent turbulent flows. *Int. J. Heat Mass Transf.*, 24:1811–1822, 1981.

[12] W. L. Chen, F. S. Lien, and M. A. Leschziner. Non-linear eddy viscosity modelling of transitional boundary layer pertinent to turbomachinery aerodynamics. *Int. J. Heat Fluid Flow*, 19(4):297–306, 1998.

[13] N. H. Cho, X. Liu, W. Rodi, and B. Schönung. Calculation of wake-induced unsteady flow in a turbine cascade. *J. of Turbomachinery*, 115(4):675–686, 1993.

[14] R. Cho and M. K. Chung. A $k-\varepsilon-\gamma$ equation turbulence model. *J. Fluid. Mech.*, 237:301–322, 1992.

[15] G. Comte-Bellot and S. Corrsin. The use of a contraction to improve the isotropy of grid-generated turbulence. *J. Fluid. Mech.*, 25:657–682, 1966.

[16] T. Craft, B. E. Launder, and K. Suga. Development and application of a cubic eddy-viscosity model of turbulence. *Int. J. Num. Methods in Fluids*, 17:108–115, 1996.

[17] T. Craft, B. E. Launder, and K. Suga. Prediction of turbulent transition phenomena with a nonlinear eddy-viscosity model. *Int. J. Heat Fluid Flow*, 18(1):15–28, 1997.

[18] S. Dhawan and R. Narasimha. Some properties of boundary layer during the transition from laminar to turbulent flow motion. *J. Fluid. Mech.*, 3:418–436, 1958.

[19] C. Dopazo. On conditional averages for intermittent turbulent flows. *J. Fluid. Mech.*, 81:433–438, 1977.

[20] H. W. Emmons. The laminar-turbulent transitionin a boundary layer - part1. *Journal of Aerospace Science*, 18:490–498, 1951.

[21] M. E. Goldstein and D. W. Wundrow. On the environmental realizability of algebraically growing disturbances and their relation to Klebanoff modes. *Theoret. Comput. Fluid Dyn.*, 10:171–186, 1998.

[22] J. P. Gostelow, G. Hong, and M. A. Sheppeard. Investigation of a by-pass turbulent spot with reference to boundary layers on turbomachinery blading. Hawaii, April 1992. ISROMAC Conference.

[23] J. P. Gostelow, N. Melwani, and G. J. Walker. Effects of steamwise pressure gradient on turbulent spot development. *J. of Turbomachinery*, 118:737–743, 1996.

[24] I. Hadžić and K. Hanjalić. Separation-induced transition to turbulence: second-moment closure modelling. *Flow, Turbulence and Combustion*, 63(1):153–173, 2000.

[25] L. Hilgenfeld, P. Stadtmüller, and L. Fottner. Experimental investigation of turbulence influence of wake passing on the boundary layer development of highly loaded turbine cascade blades. *Flow, Turbulence and Combustion*, 69:229–247, 2002.

[26] J. Hourmouziadis. *Aerodynamic design of low pressure turbines*, volume 167. AGARD Lecture Series, 1989.

[27] J. Hu and T. H. Fransson. Numerical investigation of e^N method in Navier-Stokes turbomachinery flow computations. *ISROMAC10-2004-103*, Honolulu, Hawaii, 2004.

[28] R. G. Jacobs and P. A. Durbin. Simulation of bypass transition. *J. Fluid. Mech.*, 428:185–212, 2001.

[29] N. Jiang and T. W. Simon. Evaluation of algebraic transition models for application to unsteady flows in low-pressure turbines. *ASME GT2004-54223*, Vienna, Austria, 2004.

[30] M. W. Johnson. A bypass transition model for boundary layers. *J. of Turbomachinery*, 116:759–764, 1994.

[31] M. W. Johnson and A. Dris. The origin of turbulent spots. *J. of Turbomachinery*, 122:88–92, 2000.

[32] P. Jonáš, O. Mazur, and V. Uruba. On the receptivity of the by-pass transition to the length scale of the outer stream turbulence. *Eur. J. Mech. B/ Fluids*, 19:707–722, 2000.

[33] C. L. Kuan and T. Wang. Investigation of the intermittent behaviour of transitional boundary layer using a conditional averaging technique. *Int. J. Exp. Heat Transfer, Thermodynamics, and Fluid Mechanics*, 3(2):157–173, 1990.

[34] S. Lardeau and M. A. Leschziner. Unsteady Reynolds-averaged Navier-Stokes computations of transitional wake/blade interaction. *AIAA J.*, 24:1559–1571, 2004.

[35] S. Lardeau and M. A. Leschziner. Unsteady RANS modelling of wake-blade interaction: computational requirements and limitations. *Computers & Fluids*, 34:3–21, 2005.

[36] S. Lardeau and M. A. Leschziner. Unsteady RANS modelling of wake-induced transition in linear LP-turbine cascades. submitted 2005.

[37] S. Lardeau, M. A. Leschziner, and N. Li. Modelling bypass transition with low-Reynolds-number nonlinear Eddy-viscosity closure. *Flow, Turbulence and Combustion*, 73(1):49–76, 2004.

[38] S. Lardeau, N. Li, and M. A. Leschziner. LES of transitional boundary layer at high free-stream turbulence intensity, and implications for RANS modelling. Williamsburg, Virginia, 2005. TSFP-4.

[39] X. Liu and W. Rodi. Experiments on transitional boundary layers with wake-induced unsteadiness. *J. Fluid. Mech.*, 231:229–256, 1991.

[40] K. Lodefier, E. Dick, W. Piotrowski, and W. Elsner. Modelling of wake induced transition with a dynamic description of intermittency. G. Bois, C. Sieverding, M. Manna, and T. Arts, editors, 6^{th} *European conference on Turbomachinery, Fluid Dynamics and Thermodynamics*, 730–739, Lille, France, 2005.

[41] K. Lodefier, B. Merci, C. De Langhe, and E. Dick. Transition modelling with the SST turbulence model and an intermittency transport equation. *ASME GT-2003-38282*, Atlanta, USA, 2003.

[42] K. Lodefier, B. Merci, C. De Langhe, and E. Dick. Intermittency based RANS transition modelling. *Progress in Computational Fluid Dynamics*, To appear 2006.

[43] L. M. Mack. Transition and laminar instability. *ARGARD Conference proceedings on laminar-turbulent transition*, volume ARGARD-CP-224, 1977.

[44] F. Magagnato, J. Rachwalski, and M. Gabi. Numerical investigation of the VKI turbine blade by large eddy simulation. G. Bois, C. Sieverding, M. Manna, and T. Arts, editors, 6^{th} *European conference on Turbomachinery, Fluid Dynamics and Thermodynamics*, 321–330, Lille, France, 2005.

[45] R. E. Mayle, K. Dullenkopf, and A. Schultz. The turbulence that matters. *J. of Turbomachinery*, 120:402–409, 1998.

[46] R. E. Mayle and W. B. Roberts. The role of laminar-turbulent transition in gas turbine engines. *J. of Turbomachinery*, 113(4):509–537, 1991.

[47] R. E. Mayle and A. Schulz. The path to predicting bypass transition. *J. of Turbomachinery*, 119(3):405–411, 1997.

[48] G. Medic and P. A. Durbin. Toward improved prediction of heat transfer on turbine blades. *J. of Turbomachinery*, 124(2):187–192, 2002.

[49] F. R. Menter. Two-equations eddy-viscosity turbulence models for engineering applications. *AIAA J.*, 32(8):1598–1605, 1994.

[50] F. R. Menter, M. Kuntz, and R. B. Langtry. Ten years of industrial experience with the SST turbulence model. K. Hanjalić, Y. Nagano, and M. Tummers, editors, *Turbulence, heat and mass transfer 4*, 625–632, Antalya, Turkey, October 2003.

[51] F. R. Menter, R. B. Langtry, S. R. Likki, Y. B. Suzen, and P. G. Huang. A correlation-based transition model using local variables. *ASME-GT-2004-53452 and GT-2004-53454*, Vienna, Austria, 2004.

[52] F. R. Menter, R. B. Langtry, S. Völker, and P. G. Huang. Transition modelling for general purpose CFD codes. W. Rodi and M. mulas, editors, *Engineering turbulence modelling and experiments 6*, 31–48. Elsevier, 2005.

[53] V. Michelassi, F. Martelli, R. Dénos, T. Arts, and C. H. Sieverding. Unsteady heat transfer in stator - rotor interaction by two - equation turbulence model. *J. of Turbomachinery*, 121(3):436–447, 1999.

[54] V. Michelassi, J. Wissink, and W. Rodi. Analysis of DNS and LES of flow in a low pressure turbine cascade with incoming wakes and comparison with experiments. *Flow, Turbulence and Combustion*, 69:295–330, 2002.

[55] R. Narasimha. On the distribution of intermittency in the transition region of a boundary layer. *J. Aero. Sci.*, 24:711–712, 1957.

[56] M. Opoka and H. P. Hodson. An experimental investigation of the unsteady transition process on the high lift T106A turbine blade. *ISABE-2005-1277*, Munich, Germany, September.

[57] U. Orth. Unsteady boundary-layer transition in flow periodically disturbed by wakes. *J. of Turbomachinery*, 115:707–713, 1993.

[58] R. Pecnik, W. Sanz, A. Geher, and J. Woisetschläger. Transition modeling using two different intemittency transport equations. *Flow, Turbulence and Combustion*, 70(1):299–323, 2003.

[59] R. Pecnik, W. Sanz, and P. Pieringer. Numerical investigation of unsteady boundary layer transition induced by periodically passing wakes with an intermittency transport equation. *ASME GT-2004-53204*, Vienna, Austria, 2004.

[60] S. B. Pope. *Turbulent flows*, chapter 5.4.3. The plane wake. Cambridge University press, 2000.

[61] O. N. Ramesh and H. P. Hodson. A new intermittency model incorporating the calming effect. pages 243–258, London, 1999. 3^{rd} European Conference on Turbomachinery Fluid Dynamics and Thermodynamics IMechE, Cambridge University Press.

[62] B. Raverdy, I. Mary, P. Sagaut, and L. Liamis. High resolution large-eddy simulation of the flow around a low-pressure turbine blade. *AIAA J.*, 41(3):390–398, 2003.

[63] S. Sarkar. Wake-induced transitional flow over a highy-loaded LP turbine blade through large-eddy simulation. *ASME 2005-GT-68895*, Reno, USA.

[64] A. M. Savill. A synthesis of T3 test cases predictions. O. Pironneau, W. Rodi, I. L. Ryhming, A. M. Savill, and T. V. Truong, editors, *Numerical simulation of unsteady flows and transition to turbulence*, 404–442, Lausanne, Switzerland, 1992. Proceedings of the ERCOFTAC Workshop held at EPFL 1990, Cambridge University Press.

[65] A. M. Savill. The Savill-Launder-Younis (SLY) RST intermittency model for predicting transition. *ERCOFTAC Bulletin*, 24:37–41, 1995.

[66] A. M. Savill. Chapter 6: One-point closures applied to transition. M. Hallback, D.S. Henningson, A.V. Johansson, and P.H. Alfredsson, editors, *Turbulence and Transition*, 233–268. Lecture notes from the ERCOFTAC/IUTAM Summerschool, Stockholm at 1995, Kluwer Academic Publishers, 1996.

[67] M. T. Schobeiri and B. Öztürk. Experimental study of the effect of periodic unsteady wake flow on boundary layer development, separation, and reattachment along the surface of a low pressure turbine blade. *J. of Turbomachinery*, 126:663–676, 2004.

[68] M. T. Schobeiri, K. Read, and J. Lewalle. Effect of unsteady wake passing frequency on boundary layer transition, experimental investigation, and wavelet analysis. *J. of Fluids Engineering*, 125:251–266, 2003.

[69] G. B. Schubauer and P. S. Klebanoff. Contributions on the mechanics of boundary layer transition. Technical Report 1289, National Advisory Committee for Aeronautics, 1956.

[70] V. Schulte and H. P. Hodson. Prediction of the becalmed region for LP turbine profile design. *J. of Turbomachinery*, 120(4):839–845, 1998.

[71] A. M. O. Smith. Transition, pressure gradient and stability theory. Brussels, 1956. presented at the IIX Int. Congr. Appl. Mech.

[72] M. C. Smith and A. M. Kuethe. Effects of turbulence on laminar skin friction and heat transfer. *The Physics of Fluid A*, 9(12):2337–2344, 1966.

[73] W. J. Solomon, G. J. Walker, and J. P. Gostelow. Transition length prediction for flows with rapidly changing pressure gradients. *J. of Turbomachinery*, 118(4):744–751, 1996.

[74] W. J. Solomon, G. J. Walker, and J. D. Hughes. Periodic transition on an axial compressor stator: incidence and clocking effects: Part II, Transition onset predictions. *J. of Turbomachinery*, 121:408–415, 1999.

[75] J. Steelant and E. Dick. Modelling of bypass transition with conditioned Navier-Stokes equations coupled to an intermittency transport equation. *Int. J. Num. Methods in Fluids*, 23(3):193–220, 1996.

[76] J. Steelant and E. Dick. Modeling of laminar-turbulent transition for high freestream turbulence. *J. of Fluids Engineering*, 123(1):22–30, 2001.

[77] R. D. Stieger and H. P. Hodson. The transition mechanism of highly loaded low-pressure turbine blades. *J. of Turbomachinery*, 126:536–543, 2004.

[78] R. D. Stieger and H. P. Hodson. The unsteady development of a turbulent wake through a downstream low-pressure turbine blade passage. *J. of Turbomachinery*, 127:388–394, 2005.

[79] R. D. Stieger, D. Hollis, and H. P. Hodson. Unsteady surface pressures due to wake-induced transition in a laminar separation bubble on a low-pressure cascade. *J. of Turbomachinery*, 126:544–550, 2004.

[80] Y. B. Suzen and P. G. Huang. Modelling of flow transition using an intermittency transport equation. *J. of Fluids Engineering*, 122(2):273–284, 2000.

[81] Y. B. Suzen and P. G. Huang. Numerical simulation of unsteady wake/blade interactions in low-pressure turbine flows using an intermittency transport eqation. *J. of Turbomachinery*, 127:431–444, 2005.

[82] Y. B. Suzen, P. G. Huang, L. S. Hultgren, and D. E. Ashpis. Predicitions of separated and transitional boundary layers under low - pressure turbine airfoil conditions using an intermittency transport eqation. *J. of Turbomachinery*, 125(3):455–464, 2003.

[83] Y. B. Suzen, G. Xiong, and P. G. Huang. Predictions of transitional flows in low-pressure turbines using intermittency transport eqation. *AIAA J.*, 40(2):254–266, 2002.

[84] R. L. Thomas and J. P. Gostelow. The prevasive effect of the calmed region. *ASME GT2005-69125*, Reno, USA, 2005.

[85] M. Vera, X. F. Zhang, H. P. Hodson, and N. W. Harvey. Separation and transition control on an aft-loaded ultra-high-lift LP tubine blade at low Reynolds numbers: high-speed validation. *ASME 2005-GT-68893*, Reno, USA.

[86] J. Vicedo, S. Vilmin, W. N. Dawes, and A. M. Savill. Intermittency transport modeling of separated flow transition. *J. of Turbomachinery*, 126:424–431, 2004.

[87] R. J. Volino. A new model for free-stream turbulence effects on boundary layers. *J. of Turbomachinery*, 120:613–620, 1998.

[88] D. K. Walters and J. H. Leylek. A new model for boundary layer transition using a single-point RANS approach. *J. of Turbomachinery*, 126(1):193–202, 2004.

[89] J. Westin and R. A. W. M. Henkes. Application of bypass transition with differential Reynolds stress models. *J. of Fluids Engineering*, 119(4):859–866, 1997.

[90] D. C. Wilcox. *Turbulence modelling for CFD*, volume paragraph 9.4.2. DCW Industries, Inc., 1993.

[91] D. C. Wilcox. Simulation of transition with a two equation turbulence model. *AIAA J.*, 32:247–255, 1994.

[92] X. Wu and P. A. Durbin. Evidence of longitudinal vortices evolved flom distorted wakes in a turbine passage. *J. Fluid. Mech.*, 446:199–228, 2001.

[93] X. Wu, R. G. Jacobs, J. C. R. Hunt, and P. A. Durbin. Simulation of boundary layer transition induced by periodically passing wakes. *J. Fluid. Mech.*, 398:109–153, 1999.

[94] Z. Yang and T. H. Shih. New time scale based $k - \varepsilon$ model for near-wall turbulence. *AIAA J.*, 31(3):1191–1198, 1993.

[95] T. A. Zaki and P. A. Durbin. Mode interaction and the bypass route to transition. *J. Fluid. Mech.*, 531:85–111, 2005.

[96] R. Zarzycki and W. Elsner. The effect of wake parameters on the transitional boundary layer on turbine blade. G. Bois, C. Sieverding, M. Manna, and T. Arts, editors, 6^{th} *European conference on Turbomachinery, Fluid Dynamics and Thermodynamics*, 750–759, Lille, France, 2005.

[97] X. F. Zhang, H. P. Hodson, and N. W. Harvey. Unsteady boundary layer studies on ultra-high lift low-pressure turbine blades. G. Bois, C. Sieverding, M. Manna, and T. Arts, editors, 6^{th} *European conference on Turbomachinery, Fluid Dynamics and Thermodynamics*, 363–375, Lille, France, 2005.

[98] X. F. Zhang, M. Vera, H. P. Hodson, and N. W. Harvey. Separation and transition control on an aft-loaded ultra-high-lift LP tubine blade at low Reynolds numbers: low-speed investigation. *ASME 2005-GT-68892*, Reno, USA.